

https://dspace.org/

Numerical simulations of isothermal collapse and the relation to steady-state accretion

Herbst, Rhameez Sheldon

2015-05
http://hdl.handle.net/10539/18563

Downloaded from a DSpace repository. https://dspace.org/

University of the Witwatersrand

Doctoral Thesis

Numerical Simulations of Isothermal Collapse and the Relation to Steady-State Accretion

Author:
Rhameez Sheldon Herbst

Supervisors:
Prof. Charis Harley
Prof. Ebrahim Momoniat

A thesis submitted in fulfilment of the requirements for the degree of Doctor of Philosophy

in the

Faculty of Science
School of Computational and Applied Mathematics

May 2015

Declaration of Authorship

I, Rhameez Sheldon Herbst, declare that this thesis titled, 'Numerical Simulations of Isothermal Collapse and the Relation to Steady-State Accretion' and the work presented in it are my own. I confirm that:

- This work was done wholly or mainly while in candidature for a research degree at this University.
- Where any part of this thesis has previously been submitted for a degree or any other qualification at this University or any other institution, this has been clearly stated.
- Where I have consulted the published work of others, this is always clearly attributed.
- Where I have quoted from the work of others, the source is always given. With the exception of such quotations, this thesis is entirely my own work.
- I have acknowledged all main sources of help.
- Where the thesis is based on work done by myself jointly with others, I have made clear exactly what was done by others and what I have contributed myself.

Signed: 

Date: 27/05/2015

"I want to know God's thoughts, the rest are details."

Albert Einstein

UNIVERSITY OF THE WITWATERSRAND

Abstract

Faculty of Science
School of Computational and Applied Mathematics

Doctor of Philosophy

Numerical Simulations of Isothermal Collapse and the Relation to Steady-State Accretion

by Rhameez Sheldon Herbst

In this thesis we present numerical simulations of the gravitational collapse of isothermal clouds of one solar mass at a temperature of $10K$. We will consider two types of initial conditions – initially uniform spheres and perturbed Bonnor-Ebert spheres. The aim of the performed numerical simulations is to investigate the core bounce described by Hayashi and Nakano [1]. They reported that if strong enough, the shock wave would be capable of ionizing the gas in the collapsing cloud.

The simulations are performed using two numerical methods: the TVD MUSCL scheme of van Leer using a Roe flux on a uniform grid and the TVD Runge-Kutta time-stepping using a Marquina flux on a non-uniform grid. These two particular methods are used because of their differences in numerical structure. Which allows us to confidently make statements about the nature of the collapse, particularly with regards to the core bounce. The convergence properties of the two methods are investigated to validate the solutions obtained from the simulations. The numerical simulations have been performed only in the isothermal regime by using the Truelove criterion [2] to terminate the simulation before central densities become large enough to cause artificial fragmentation.

In addition to the numerical simulations presented in this thesis, we also introduce new, analytical solutions for the steady-state accretion of an isothermal gas onto a spherical core as well as infinite cylinders and sheets. We present the solutions and their properties in terms of the Lambert function with two parameters, γ and m. In the case of spherical accretion we show that the solution for the velocity perfectly matched the solutions of Bondi [3]. We also show that the analytical solutions for the density – in the spherical case – match the numerical solutions obtained from the simulations. From the agreement of these solutions we propose that the analytical solution can provide information about the protostellar core (in the early stages of its formation) such as the mass.

Acknowledgements

My deepest gratitude goes to both of my supervisors. To Charis I say thank you for working tirelessly with me. For your patience, guidance and belief in me throughout the completion of this thesis. To Prof. Momoniat, thank you for your extremely insightful suggestions which often come across as vague, initially, but always lead to profound realisations. You have both done more than supervise, you have shown me what it means to pursue understanding. To my colleagues and dear friends, Byron and Mitch, thank you for the continuous encouragement and extremely helpful discussions. You have supplied endless entertainment (and perhaps a new found addiction for high quality caffeine) and given me room to reflect on my own work by allowing me a glimpse of yours. To Katlego, my brother, this is the realisation of a thirteen year old dream. Thank you for being a pillar and a compass and for keeping in my mind the importance of "**?**". Finally, I say thank you to my family for inspiring me to go further.

Contents

Declaration of Authorship i

Abstract iii

Acknowledgements iv

Contents v

List of Figures viii

List of Tables xi

Glossary xii

Symbols xiii

1 Introduction 1
- 1.1 Astrophysical Properties of Star Formation . . . 1
- 1.2 Numerical Simulation of Observed Phenomena . . . 3
  - 1.2.1 One-dimensional Collapse . . . 3
  - 1.2.2 Two-Dimensional Collapse: Spherical and Cylindrical Simulations 7
- 1.3 Steady-State Accretion . . . 8
- 1.4 Concluding Remarks . . . 8

2 Hyperbolic Conservations Laws and Numerical Methods 10
- 2.1 Introduction . . . 10
- 2.2 Derivation of Conservation Laws . . . 11
- 2.3 Hyperbolic Conservation Laws . . . 13
  - 2.3.1 Domain of Dependence and Range of Influence . . . 16
- 2.4 Finite Volume Methods for Hyperbolic Conservation Laws . . . 16
  - 2.4.1 Elements of Stability . . . 19
    - 2.4.1.1 The CFL Condition . . . 20
    - 2.4.1.2 Consistency . . . 20
    - 2.4.1.3 One-Norm Stability . . . 21
    - 2.4.1.4 TVD Stability . . . 22

2.4.2 Artificial Fragmentation . . . 22
2.5 Source Terms . . . 23
2.5.1 Geometric Source Terms . . . 24
2.5.2 Gravitational Potential . . . 24
2.5.2.1 Direct Method . . . 26
2.5.2.2 Multipole Expansion . . . 26
2.5.2.3 Diffusion Equation Approach . . . 27
2.5.2.4 Conservative Approach . . . 27
2.6 Hydrodynamic Equations Governing Spherically Symmetric, Isothermal Collapse . . . 28
2.7 Concluding Remarks . . . 29

3 Isothermal Clouds: Stability and Steady-States 30
3.1 Introduction . . . 31
3.2 Jeans Instability . . . 32
3.3 Equilibrium Configurations . . . 35
3.3.1 Gravitational Stability . . . 37
3.4 Steady-State Accretion . . . 39
3.4.1 Lambert's W-function . . . 39
3.4.2 Analytical Solutions of Steady-State Accretion . . . 40
3.4.2.1 Calculation of Gravitational Potentials . . . 41
3.4.3 Spherical Bondi Accretion . . . 43
3.4.4 Cylindrical Accretion . . . 45
3.4.5 Planar Accretion . . . 47
3.5 Concluding Remarks . . . 48

4 Numerical Simulations of Isothermal Collapse: TVD-MUSCL Scheme 50
4.1 Introduction . . . 51
4.2 Numerical Simulation . . . 54
4.2.1 The Model . . . 54
4.2.2 Derivation of Numerical Scheme . . . 56
4.2.3 Initializing Parameters for Numerical Simulation . . . 58
4.3 Results and Discussion . . . 58
4.4 Concluding Remarks . . . 62

5 Numerical Simulations of Isothermal Collapse: TVD Runge-Kutta Scheme 65
5.1 Introduction . . . 66
5.2 Numerical Simulation . . . 66
5.2.1 The Marqnuina Flux . . . 66
5.2.2 Runge-Kutta Time-Stepping . . . 67
5.2.3 Non-uniform Grid Construction . . . 68
5.2.4 Initializing Parameters for Numerical Simulations . . . 69
5.3 Results and Discussion . . . 69
5.4 Concluding Remarks . . . 73

6 Comparison of Numerical Schemes 76
6.1 Introduction . . . 77

6.2 Analysis of the TVD-MUSCL Scheme 77
6.2.1 Consistency 77
6.2.2 Stability 78
6.2.3 Convergence 78
6.3 Analysis of TVD Runge-Kutta Scheme 79
6.3.1 Consistency 79
6.3.2 Stability 80
6.3.3 Convergence 80
6.4 The Rankine-Hugoniot Conditions for Steady-State Accretion 81
6.4.1 Stationary Shocks 82
6.5 Discussion and Concluding Remarks 83

7 Conclusion and Closing Statements **88**

Bibliography **90**

List of Figures

1.1 *The Orion Molecular Cloud Complex: The most notable features are Barnard's Loop (the cresent shaped cloud) and the Great Orion Nebula. Also present in this complex are cold, dark nebulae known as Bok globules [4].* 2

1.2 *Bok globules: one of the coolest, densest protostellar objects in which individual stars are expected to form.* [5] 2

1.3 *The Figure shows the density profiles at different times found by the numerical simulations of Larson [6].* 6

3.1 *The Figure shows plots of the solutions to the isothermal Lane-Emden equation. On the abscissa is the dimensionless length and the dimensionless potential in on the ordinate.* 36

3.2 *The Figure shows plots of the dimensionless length against the dimensionless density for each case considered.* 37

3.3 *In the above Figure the log of the central concentration (ratio of central to outer density) as been plot against the dimensionless mass. The fist maximum is associated with the maximum radius possible for a gravitationally stable Bonnor-Ebert sphere.* 38

3.4 *The Figure shows plots of the two branches of the Lambert function together with their inverse. While the primary branch cut (dashed) is defined for all positive real numbers, the secondary branch cut is only defined on a small domain of negative real numbers.* 40

3.5 *The above Figure shows the two functions W_0 (red) and W_{-1} (green) for parameter values $\gamma = 0.9, 1.0, 1.1$ (corresponding to solid, dashed and dotdashed lines) and $m = 2$. The solutions are exactly those of classical Bondi accretion. For the case of $\gamma = 1$ the solutions intersect $x = m/2$. The solid line in blue represents the free-fall velocity profile.* 44

3.6 *The Figure shows a log scaled plot of the dimensionless length versus the dimensionless density. The density corresponding to subsonic flow is in red while the supersonic density profiles appear in green. Again, this has been done for parameter values of $\gamma = 0.9, 1.0, 1.1$ (solid, dashed, dotdashed) and $m = 2$. The solid blue line represents the density profile associated with free-fall.* 45

3.7 *The Figure shows the plot of the velocity profiles for cylindrical accretion in the case where $\bar{\lambda}_{cyl} < 1$. The red curves represent subsonic flow while curves in green represent supersonic flow. The single blue line represents the free-fall line. In these plots $\bar{\lambda}_{cyl} = 0.9, x_m = 5$.* 47

3.8 *The Figure shows the plot of the velocity profiles for cylindrical accretion in the case where* $\bar{\lambda}_{cyl} > 1$. *Again the red curves represent subsonic flow while curves in green represent supersonic flow. The single blue line represents the free-fall line. In these plots* $\bar{\lambda}_{cyl} = 2, x_m = 5$. 47

3.9 *The Figure shows the plot of the velocity profiles for steady planar accretion. The red curves represent subsonic flow while curves in green represent supersonic flow. The single blue line represents the free-fall line. In these plots* $\bar{\sigma} = 1, x_m = 5$. *and the solid, dashed and dot-dashed, red and green curves represent* $\gamma = 0.25, 1, 4$ *respectively.* 48

4.1 *A log-log plot of the density for a spherically symmetric cloud at different times during the collapse performed by Larson [6]. On the horizontal axis is the log of the dimensional radius and the vertical axis shows the log of the dimensional density. Simulations performed here were for an initial uniform cloud with a mass of* $1M_{\odot}$ [6]. 52

4.2 *A log-log plot of the density for Bonnor-Ebert spheres with increasing central densities but the same dimensional radius . On the horizontal axis is the log of the dimensional radius and the vertical axis shows the log of the dimensional density. The density profiles are very similar to those found by Larson, shown in Figure 4.1* 53

4.3 *The Figure shows log-log plots of the density profile for initially uniform spheres at various times (in units of* t_{ff}*), shown in the legend.* 59

4.4 *The Figure shows plots of the density profile for perturbed Bonnor-Ebert sphere at various times (in units of* t_{ff}*), shown in the legend.* 60

4.5 *The Figure illustrates the increase in central density for models* Uni 1 *(red),* Uni 2 *(blue) and* Uni 3 *(green). Core rebound is clearly seen in models one and two.* 61

4.6 *The Figure illustrates the increase in central density for models* BE 1 *(red),* BE 2 *(blue) and* BE 3 *(green). No rebound is seen however the central accretion is temporarily decreased.* 61

4.7 *The Figure illustrates the accretion rate at the centre for model* BE 1. *It is clear that the accretion rate is slowed down momentarily however gas continues to flow toward the centre.* 62

4.8 *The plots illustrate the density profiles of the initially uniform spheres for the last iteration together with the solution for steady-state accretion as well as the free-fall profile. The analytical solutions for steady-state accretion match closely with the numerical solution.* 63

4.9 *The plots illustrate the density profiles of the perturbed Bonnor-Ebert spheres for the last iteration together with the solution for steady-state accretion as well as the free-fall profile. The analytical solutions for steady-state accretion match closely with the numerical solution.* 64

5.1 *The Figure shows plots of the density profile at various times (in units of* t_{ff}*), shown in the legend.* 70

5.2 *The density profiles at various times for the three models with initially uniform density. All three clouds collapse in a similar fashion with subtle differences in the most dense cloud: collapse occurs in the central region slightly quicker while the rest of the cloud collapses and hence no core rebound is observed.* 71

5.3 *The plots illustrate the density profiles for the last iteration together with the solution for steady-state accretion for the initially uniform clouds. The analytical solutions for steady-state accretion match closely with the numerical solution.* 72
5.4 *The plots illustrate the density profiles for the last iteration together with the solution for steady-state accretion for the perturbed Bonnor-Ebert spheres. The analytical solutions for steady-state accretion match closely with the numerical solution.* 73
5.5 *The Figure illustrates the increase in central density for Bonnor-Ebert spheres with red, green, blue representing the order of increasing density. The core bounce is much less pronounced in the case of the Bonnor-Ebert spheres.* 74
5.6 *The Figure illustrates the accretion rate at the centre for model* BE 1. *It is clear that the accretion rate is slowed down momentarily however gas continues to flow toward the centre.* 74

6.1 *The Figure illustrates the increase in central density for models one (red), two (blue) and three (green). Core rebound is clearly seen in models one and two.* 79
6.2 *The Figure illustrates the increase in central density for models one (red), two (blue) and three (green). Core rebound is clearly seen in models one and two.* 80
6.3 *The Figure illustrates the density profile at the last iteration for each numerical scheme presented in this thesis. The two methods are shown to be in very good agreement with each other despite the difference in their numerical structure. The TVD-MUSCL scheme appears in blue while the red plot corresponds to the TVD Runge-Kutta scheme.* 81
6.4 *The plots show the Rankine-Hugoniot conditions for transonic, subsonic and supersonic jumps for a spherical fragment.* 84
6.5 *The plots show the Rankine-Hugoniot conditions for transonic, subsonic and supersonic jumps for an infinite cylinder when* $\lambda < 1$.*Note that supersonic jumps are not possible as the two plots do not intersect meaning that the Rankine-Hugoniot conditions are not satisfied.* 85
6.6 *The plots show the Rankine-Hugoniot conditions for transonic, subsonic and supersonic jumps for an infinite cylinder when* $\lambda > 1$. 86
6.7 *The plots show the Rankine-Hugoniot conditions for transonic, subsonic and supersonic jumps from the top down. The condition for a transonic jump is not satisfied in the case of the infinite sheet as the two graphs intersect only at the maximum length* x_m *and both solutions are complex beyond that point.* 87

List of Tables

4.1 *In the above Table we provide initial data for the collapse of each presented model. The dimensional parameters are the clouds radius, the central density, and the mean density. The dimensionless quantities are the ratio of free-fall to sound travel time.* 58
4.2 *The Table shows the parameters that match the Bondi accretion solution to the numerical simulations performed using the TVD Runge-Kutta scheme.* 61

5.1 *In the above Table we provide initial data for the collapse of each presented model. The dimensional parameters are the clouds radius, the central density, and the mean density. The dimensionless quantities are the ratio of free-fall to sound travel time.* 69
5.2 *The Table shows the parameters that match the Bondi accretion solution to the numerical simulations performed using the TVD Runge-Kutta scheme.* 75

Glossary

Interstellar Medium (ISM): Gas which permeates galaxies, generally at extremely low densities and vast temperature ranges, mainly hydrogen gas.

Giant Molecular Cloud (GMC): Cold, dense parts of the interstellar medium consisting mostly of molecular hydrogen.

Bok globules: Cold, dark molecular clouds from which individual stars are expected to form.

Isothermal gas: A gas whose temperature remains constant under changes of pressure and volume.

Jean's Radius: The critical radius which marks the turning point in the stability of a spherical, uniformly dense cloud against gravitational collapse.

Bonnor-Ebert sphere: A spherical, isothermal gas cloud in hydrostatic equilibrium. The Bonnor-Ebert sphere must be bounded by a surrounding medium.

Free-fall time (t_{ff}): The time take for a spherical cloud to collapse down to a single point in the absence of pressure.

Sound travel time (t_s): The radius of a spherical cloud divided by the sound speed in the cloud.

Bondi accretion: The flow of gas, due to gravitational attraction, on to a compact object. In Bondi accretion self-gravitation is ignored.

Hyperbolic conservation laws: A system of coupled partial differential equations that describe the conservation of quantities such as mass, momentum and energy.

Numerical flux: A numerical approximation of the flux term in the hyperbolic conservation laws. The Roe flux and the Marquina flux are both examples of numerical flux formulae.

TVD schemes: Any numerical scheme that is total variation diminishing.

Symbols

t	time	s
t_{ff}	free-fall time	s
t_s	sound travel time	s
r	radial distance	cm
R_c	cloud radius	cm
R_J	Jeans radius	cm
ρ	density	gcm^{-3}
ρ_c	central density	gcm^{-3}
$\bar{\rho}$	mean density	gcm^{-3}
u, v, w	velocity components	cms^{-1}
$\mathbf{u}$	velocity vector	cms^{-1}
E	specific total energy	$ergg^{-1}$
P	pressure	$gcm^{-1}s^{-2}$
c	sound speed	cms^{-1}
T	temperature	K
Φ	gravitational potential	erg
ω	angular frequency	rads^{-1}
ϕ	dimensionless gravitational potential	1
α	ratio of thermal to gravitational energy	1
β	ratio of rotational to gravitational energy	1
ξ	dimensionless radius	1
μ	mean molecular weight	1
σ	surface density	gcm^{-2}

Dedicated to my Wife

Chapter 1

Introduction

1.1 Astrophysical Properties of Star Formation

The theory of star formation is one of the corner stones of astrophysics. It forms the basis of stellar evolution which is fundamental to our understanding of galaxy evolution on a large scale and planetary formation on a small scale. Currently theory, observation and computation suggest planets form from the gas remaining after star formation has occured. While the assumption that the molecular clouds in which stars form are isothermal is a great idealization it is highly applicable to the early stages of star formation when the density of the cloud is so low ($\sim 10^{-19} gcm^{-3}$) that any heat generated during the collapse is efficiently radiated away before the cloud can increase in temperature. This can occur over several orders of magnitude – the isothermal approximation ceases to be realistic for densities greater than ($\sim 10^{-13} gcm^{-3}$) [7].

Star formation occurs in the densest and coldest parts of giant molecular clouds (GMC's) in the interstellar medium (ISM hereafter) where gravitational energy is dominant over all other forms of energy: thermal, magnetic, turbulent etc. The ISM can be divided into regions of various sizes – two stand out as particularly important: large low density CO regions with masses in the ranges of $10^3 - 10^4 M_\odot$ that are dominated by turbulence and magnetism, see Figure 1.1. More important (in the context of this thesis) are the higher density and much smaller regions in which gas motions are mainly due to thermal effects and the presence of turbulence and magnetism may be ignored. It is in these regions that star formation is thought to occur. In addition to these cold dense regions, there are also dark nebula, known as *Bok globules* which occur in isolation (see Figure 1.2). These globules have properties very similar to the dense molecular clumps described above. It has, until recently, been assumed that most regions of star formation would exist in spherical or at least close to spherical structures, but



FIGURE 1.1: *The Orion Molecular Cloud Complex: The most notable features are Barnard's Loop (the cresent shaped cloud) and the Great Orion Nebula. Also present in this complex are cold, dark nebulae known as Bok globules [4].*

observation has uncovered that non-spherical regions are in fact more common with the cylindrical filaments being the most frequent of them. Star formation occurs in large



FIGURE 1.2: *Bok globules: one of the coolest, densest protostellar objects in which individual stars are expected to form.* [5]

HII regions which are dense, cool and unstable against gravitational collapse [8]. As the gas clouds collapse their central temperatures increase but in the early stages the increase in central temperature is quickly radiated away due to the low density. This roughly maintains the low temperature. Above densities of $\sim 10^{-13} g\, cm^{-3}$ the heat can no longer be radiated away quickly enough and the central region of the cloud ceases to be isothermal. At this stage the core building occurs in a more or less free-fall fashion leading to an increase in the core size. As a result the outer region of the cloud then falls toward the central mass. It is expected that supersonic flow will ensue at this point. While this free-fall nature is a subtle point it does raise the importance of the steady

flow that occurs in the region surrounding the core. Also, since the gas outside of the nascent core still exists at isothermal densities, any heat radiated by the core will still be efficiently radiated away outside of the region where core formation occurs. Thus a complex core-envelope system is formed which requires an understanding of both the isothermal flow of the infalling gas as well as adiabatic flow governing the evolution of the core.

Once the density of the cloud exceeds the isothermal limit additional physical phenomena need to be introduced into the model for numerical simulations to remain relevant. These physical phenomena include magnetism and turbulence mainly. Another relevant physical phenomenon, which can be included in the isothermal phase, is rotation, see [9] as an example of numerical simulations with rotation. Angular momentum density is particularly important with regards to how it changes the shape of the collapsing cloud. Momentum not only flattens the cloud but can also introduce ring and disc structures [10–12].

1.2 Numerical Simulation of Observed Phenomena

Complimentary to the progress made through observation of star forming regions in several wavelengths is the numerical simulation of the theoretical models for star formation. Even in the simplest models, the numerical methods employed need to be robust due to the nonlinear nature of the governing equations – the presence of gravity also introduces the need for high resolution grids to track core formation. The development of the supercomputer has given rise to the development of numerical codes such as the Zeus and Athena (to name just two) hydro-codes which are capable of running simulations with a very large number of grid point and a variety of numerical methods [13, 14]. The approach taken in this thesis has been to construct numerical code from the ground up. This allows for a greater degree of freedom in terms of engaging with the various aspects of the numerical methods used. As such we are able to engage with the efficiency and accuracy of methods of this type within the context presented. Furthermore, the two codes hydro-codes mentioned contain a lot more physics than necessary (such as magnetism and radiation) for the problem considered in this thesis.

1.2.1 One-dimensional Collapse

The mathematical modelling of star formation goes back to the work of Sir James Jeans [15] in which he considered linear perturbations of the Euler equations for an infinite, isothermal cloud. This gave rise to the Jeans instability criterion which states that a

cloud must be below a particular radius (the Jeans radius, R_J) in order to be unstable to gravitational collapse. While the assumption of an infinitely large gas cloud was obviously an unreasonable one, the work of Bonnor [16] and Ebert [17] (independently) on the gravitational stability of finite isothermal clouds in hydrostatic equilibrium rendered a strikingly similar criterion:

$$R_{cloud} < R_J = \frac{0.41GM\mu}{R_g T},$$

G, M and μ are the gravitational constant, cloud mass and the mean molecular mass while R_g and T are the gas constant and the temperature. The simplest numerical simulation comes from the assumption of a pressureless collapse. It gives rise to the free-fall time which has proven useful in that it has served as a reference upon which collapse time is measured and it has been demonstrated that the inclusion of pressure does not significantly increase the collapse time. The exception to this is the case where the cloud is close to the Jeans radius. This results in a core rebound which consequently delays the collapse. The free-fall time can be shown [7] to be given by

$$t_{ff} = \sqrt{\frac{3\pi}{32G\rho}}. \tag{1.1}$$

One dimensional collapse has laid the ground for our understanding of isothermal clouds in the context of star formation. The assumption of spherical symmetry had played a fundamental role in explaining both qualitative behaviour (like the stability analysis by Jeans, Bonnor and others [6, 16]) as well as quantitative behaviour through the numerical (see [6, 18–20]) and analytical (see [21, 22]) solving of the hydrodynamic equations. While the work of Jeans and Bonnor provided the qualitative behaviour it also provided the initial conditions for numerical simulation.

Bodenheimer and Sweigert [23], demonstrated the dependence of the collapse on the ratio of free-fall time to sound travel time by solving the hydrodynamic equation in the Lagrangian formulation using Henyey's implicit method. It is important to note that the importance of this ratio is not surprising as it may just be reinterpreted as the Jeans stability criterion. Larson [6] modelled a more complex problem by introducing the radiation equations. His numerical simulations illustrated the self-similar nature of isothermal collapse which later gave rise to the development of self-similar solutions. While Larson [6] noted that a core rebound is experienced close to the Jeans radius it was Hayashi [24] who described the bounce as resulting from the large pressure gradients toward the center as collapse proceeds. Hayashi further concluded that this bounce resulted in a shock wave "strong enough to ionize" the hydrogen gas, making this a fairly important feature to note and investigate. An interesting point to raise here is that Larson attributed the core bounce (referred to as "rebound" in his paper [6])

to numerical inaccuracy. The idea proposed here is that the bounce is in fact not a numerical artifact but rather the result of the formation of a high pressure gradient close to the free-fall time whenever the cloud radius is initially close to the Jeans radius. It will be shown later that the bounce propagates outward creating a short-lived outflow and a shock in the density further down stream. The shape of this shock is changed when rotation is included in the model. Indeed the exact nature of the collapse of clouds close to R_J will depend on the grid resolution and this will be investigated in Chapters 4 and 5.

At the time of Larson's work the Henyey method – an implicit solver for the stellar structure equations – was the most appropriate method available to simulate star formation. The scheme is computationally expensive (and therefore Larson's grid was relatively coarse) due to its implicit nature, but the results of the collapse remain a benchmark for numerical simulations of spherically symmetric, isothermal collapse. Foster et al. [19] performed numerical simulations of isothermal collapse of clouds initially near hydrostatic equilibrium, i.e. perturbed Bonnor-Ebert spheres, using the piecewise parabolic method of Collela and Woodward as well as the sink cell method proposed by Boss and Black [25]. They found that differently perturbed clouds all had similar evolutions, particularly toward late times in the collapse. An important result found by Foster et al. [19] was that for initially non-singular finite core sizes supersonic velocities developed during the collapse, tending to $3.3c$ toward the centre of the cloud. They also found that the density had a r^{-2} profile near the center and that the accretion rate was strongly dependant on the ratio of initial cloud radius to core radius. While Larson developed the benchmark solution of numerical, isothermal collapse, Shu [21] derived the self-similar solutions for the collapse of a singular isothermal cloud. Shu considered the following equations

$$\frac{\partial M}{\partial t} + u\frac{\partial M}{\partial r} = 0, \quad \frac{\partial M}{\partial r} = 4\pi r^2 \rho \tag{1.2}$$

$$\frac{\partial \rho}{\partial t} + \frac{1}{r^2}\left(r^2 \rho u\right) = 0 \tag{1.3}$$

$$\frac{\partial u}{\partial t} + u\frac{\partial u}{\partial r} = -\frac{c^2}{\rho}\frac{\partial \rho}{\partial r} - \frac{GM_r}{r^2}, \tag{1.4}$$

and via the following change of variables

$$\begin{aligned} x &= \tfrac{r}{ct} & \rho &= \tfrac{\alpha(x)}{4\pi G t^2} \\ M &= \tfrac{c^3 t}{G} m(x) & u &= cv(x), \end{aligned}$$

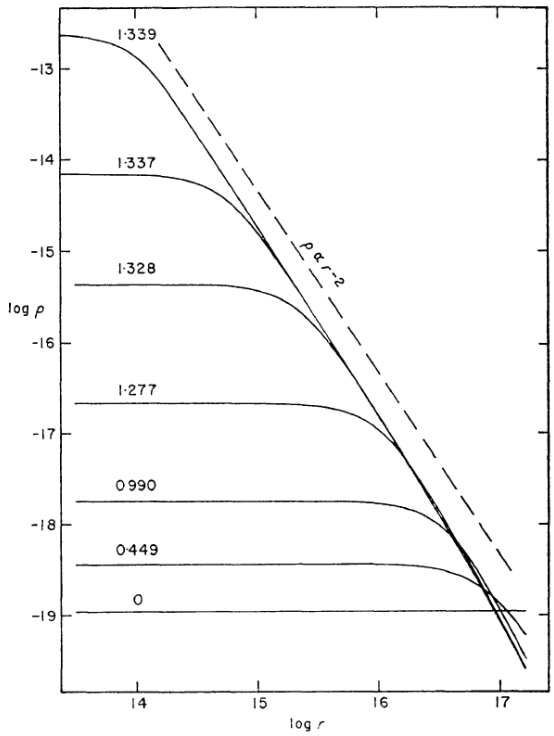


FIGURE 1.3: *The Figure shows the density profiles at different times found by the numerical simulations of Larson [6].*

showed that the equations reduce to the system

$$\begin{aligned}\left[(x-v)^2-1\right]\frac{dv}{dx} &= \left[\alpha(x-v)-\frac{2}{x}\right](x-v)\\ \left[(x-v)^2-1\right]\frac{1}{\alpha}\frac{d\alpha}{dx} &= \left[\alpha-\frac{2}{x}(x-v)\right](x-v),\end{aligned} \tag{1.5}$$

with the mass equation given by

$$m = \alpha x^2(x-v). \tag{1.6}$$

From this system of equations a number of solutions may be generated. The hydrostatic solution is given by

$$v = 0,\ \alpha = 2/x^2,\ m = 2x$$

whereas the dynamic solution is given by

$$x - v = 1,\ \alpha = 2/x.$$

Shu [21] argued from this dynamical solution that the initial dimensional density for self-similar collapse should be of the form

$$\rho = \frac{c^2 A}{4\pi G r^2}.$$

Whitworth and Summers [26] extended the similarity solutions of isothermal collapse stating the solutions of Larson [6] and Penston [18] (the so-called LP solution) and Shu [21] as special cases in a continuum of solutions described by two parameters related to the core size and density. Although the self-similar approach has been extensively developed by various authors, see [22, 27–30], Whitworth et al. [31] have warned against the use of the singular isothermal sphere as an initial condition, arguing that such an initial condition would be biased against the formation of binary stars. The singular sphere is also not favourable for numerical simulation, however it is noted that it may be applicable to the late stages of star formation when the central density is many orders of magnitude larger than the rest of the collapsing cloud and the core region is much smaller than the rest of cloud. This idea of using a solution for an infinitely large cloud to approximate the density profile of a finite cloud will be used later in Chapter 4 and 5 with analytical solutions for spherically symmetric Bondi accretion to be derived in the next Chapter.

Despite the focus of numerical simulation being on multiple star formation, spherically symmetric collapse remains relevant in modern investigation. Ogino revisited the problem of spherically symmetric collapse of unstable Bonnor-Ebert spheres [20] and found that the evolution of the collapse could be separated into two stages; the core building stage in which the central density is increased, and the later stage of accreting flow in which the nascent stellar core undergoes contraction. Later, Aikawa et al. [32] also used the TVD-MUSCL scheme to simulate the collapse of unstable Bonnor-Ebert spheres with closer attention paid to the comparison with observation.

1.2.2 Two-Dimensional Collapse: Spherical and Cylindrical Simulations

Historically, numerical simulations of isothermal collapse have followed two tracks. On the one track simulations have been performed in spherical coordinates. The numerical simulations of Boss is one such example, see [11, 33]. Along a different path cylindrical coordinates have been employed, see [10, 12, 25]. The extension to three-dimensional simulations have allowed for multiple star formation to also be investigated [34, 35].

Larson [9] extended his one-dimensional work to simulate an axisymmetric cloud with and without rotation using the same scheme implemented in his previous work [6]. In the absence of rotation Larson [9] found that the clouds with perturbations of concentric cylinders about the pole and horizontal perturbations about the equator evolved back to their spherical distributions during the collapse. This strengthened the idea that slight alterations in the initial data did not change the structure of the collapse significantly.

While Larson's [9] simulations were done on a very coarse grid, static grid (only 12×6), the formation of a ring was confirmed by Boss [11] who used a more complex method that included a moving mesh [33]. Black and Bodenheimer [10] had developed a similar code earlier but employed a cylindrical coordinate system.

While the formation of the ring remains allusive, Boss [11] used analytical solutions to demonstrate the presence of a ring in pressureless collapse. Fundamentally, the formation of both ring and disc fragments is likely due to rotation. Norman [12] pointed out that numerical schemes in which the numerical diffusion caused small amounts of angular momentum density to be diffused outward are prone to form rings while discs form out of simulations in which the angular momentum density is diffused inward due to numerical diffusion of the particular numerical method. Another point to note is that it is common practice to replace the equation for $\phi-$momentum density ρw (momentum density about the axis of rotation) with an equation for the angular momentum density $\rho w r \sin\theta$. With this replacement global momentum can be maintained and local angular momentum density may be directly controlled in the numerical scheme.

1.3 Steady-State Accretion

Steady-state accretion plays a fundamental role in the process of star formation – after core formation the inflowing gas is expected to reach the free-fall speed toward the centre. However, the effects of pressure should still remain important throughout the collapsing cloud making Bondi accretion applicable to the gas dynamics in the early stages of core formation. Bondi found implicit solutions for steady-state accretion [3]. In Chapter 3 of this work we will introduce analytical, closed form solutions for Bondi accretion. The importance of such a solution is that core masses and radii could be calculated directly from the collapse as opposed to assuming a particular number or grids constitute a core. The extension of the Bondi solution to two dimensional flow has been investigated by Cassen and Pettibone [36] and the analytical solutions for one-dimensional flow could be extended in a similar way for the same purpose.

1.4 Concluding Remarks

In this Chapter we have discussed the physical aspects of star formation together with the numerical approaches that have been considered by several authors. In addition to this we have also briefly summarized the concept of steady-state accretion, highlighting the relevance of Bondi accretion in the context of star formation. In the Chapter to

follow we will discuss the mathematical and numerical aspects involved in solving the hydrodynamic equations that model the gravitational collapse of isothermal clouds.

Chapter 2

Hyperbolic Conservations Laws and Numerical Methods

2.1 Introduction

In this Chapter we review the theory of hyperbolic conservation laws and briefly discuss finite volume methods in the context of spherical and axisymmetric isothermal collapse.

In addition to the equations for isothermal collapse being hyperbolic, they also contain a source term in the form of self-gravitation. The inclusion of source terms requires special treatment that is automatically arrived at in the theory of numerical methods for hyperbolic equations. In the context of star formation it is particularly important to allow for the steady-states – such as the slowing down of the collapse of the core when it becomes opaque to radiation – to be arrived at numerically although this will be dependent strongly on the physics included in the model. In essence, one ideally wants to be able to evolve the fluid equations to the point where the star is in hydrostatic equilibrium with all the relevant physics (radiation, turbulent convection etc). This is however not practical and as such star formation is generally modelled in stages.

Historically, star formation has been investigated with a diverse range of numerical techniques: Larson employed a "simplified" Henyey method [6, 9] which is an implicit Lagrangian formulated method used to solve the stellar structure equations [37]. Gentry et al. [38] introduced the donor cell or fluid in cell (FLIC) method which was used throughout the series by Boss [11, 33, 34] in his investigation of two and three dimensional collapse of axisymmetric isothermal clouds as well as non-axisymmetric perturbations of collapsing isothermal clouds. Boss highlighted in [33] a major advantage of the FLIC method – negative density is automatically avoided in the scheme. Higher order schemes

like the piecewise parabolic method of Colella and Woodward [39] have been used in a Lagrangian remapping fashion by Foster and Chavalier [19]. Moving grids have also been used in many star formation simulations [10] to improve the local and global conservation of angular momentum – an extremely important quantity in the simulation of rotating collapse. The quantity is pivotal to our understanding of the nature of rotating collapse particularly because the direction of the numerical diffusion of angular momentum may determine the shape of the fragment resulting from the collapse. Norman [12] found that the donor cell scheme due to Black and Bodenheimer [10] directed the numerical diffusion of the angular momentum inward while another scheme developed by Tscharnuter and Winkler [40] diffused angular momentum outward. As a result these two schemes produced results which were not completely in strong agreement: the former favoured the formation of rings while the latter did not.

2.2 Derivation of Conservation Laws

Before discussing the theory of hyperbolic conservation laws and deriving the approach for the numerical solutions of the equations considered here, it is useful to derive the Euler equations. This derivation is important as it will provide the two forms of the conservation laws required for the formulation of the numerical solution: the integral form which holds even in the presence of a discontinuity in the conserved quantity and the differential form which is the form in which the equations generally appear.

Consider a fluid with a velocity field $\mathbf{u}(\mathbf{x}, t)$ (we will write $\mathbf{u}$ in shorthand) and a volume of fixed size V held at a fixed position in the fluid. Consider also some intensive quantity of the fluid and label this quantity $q(\mathbf{x}, t)$ (q in shorthand). The total amount of this quantity contained within the fixed volume is provided by

$$Q = \int_V q dV.$$

The change in Q after some time Δt must be equal to the amount of that intensive quantity fluxing through the boundary of the volume, ∂V, in the same time. This may be expressed as

$$\int_{\partial V} q\, \mathbf{u}.\mathbf{n}\, \partial V \Delta t,$$

where $\mathbf{u}.\mathbf{n}$ is the scalar product of the velocity vector and the unit normal to the surface. Combining these terms provides

$$Q|_{t+\Delta t} - Q|_t = -\int_{\partial V} q\, \mathbf{u}.\mathbf{n}\, \partial V \Delta t. \tag{2.1}$$

Writing Q in its integral form and using the divergence theorem we find

$$\int_V q(\boldsymbol{x}, t+\Delta t)dV - \int_V q(\boldsymbol{x}, t)dV = -\Delta t \int_V \nabla.(q\boldsymbol{u})dV.$$

This may be rearranged to provide us with

$$\int_V \left(\frac{q(\boldsymbol{x}, t+\Delta t) - q(\boldsymbol{x}, t)}{\Delta t} + \nabla.(q\boldsymbol{x}) \right) dV = 0. \tag{2.2}$$

Given that the volume can be chosen arbitrarily and taking the limit as $\Delta t \to 0$, the integrand must necessarily be zero and thus the conservation law for q is provided by

$$\frac{\partial q}{\partial t} + \nabla.(q\boldsymbol{u}) = 0. \tag{2.3}$$

For conserved quantities in general the complexity of the model determines the inclusion of additional terms for example pressure, self-gravity and radiative transfer. Under such circumstances the conservation law has the form

$$\frac{\partial q}{\partial t} + \nabla.(q\boldsymbol{u}) = s(\boldsymbol{x}, t, q, \boldsymbol{u}), \tag{2.4}$$

where the function s may be dependent not only on space and time but also on the conserved quantity and the velocity field. In the case of isothermal, gravitational collapse the fluid equations are provided by

$$\frac{\partial \rho}{\partial t} + \nabla.(\rho\mathbf{u}) = 0, \tag{2.5}$$

$$\frac{\partial \rho\mathbf{u}}{\partial t} + \nabla.(\rho\mathbf{u} \otimes \mathbf{u}) = -\nabla P - \rho\nabla\Phi. \tag{2.6}$$

The above system of equations is closed by the isothermal equation of state provided by $P = c^2\rho$ and the Poisson equation for the gravitational potential provided by $\nabla^2\Phi = 4\pi G\rho$. In the hydrodynamic equations ρ and $\rho\mathbf{u}$ are the mass density and the momentum density respectively – the conserved quantities of the system. P is the pressure and $-\nabla P$ represents the force (due to the pressure of the surrounding fluid) per unit volume acting on the fluid. Φ is the gravitational potential and the term $-\rho\nabla\Phi$ represent the force per unit volume due to self-gravitation.

It is important to note that while conservation laws in the form of equation (2.4) are convenient in terms of deriving numerical methods it is important to note that in the presence of discontinuities (i.e. shocks) only the form in equation (2.1) remains. As an example this may by written in one-dimensional, Cartesian geometry as

$$\int_{x_1}^{x_2} q(x, t_2)dx - \int_{x_1}^{x_2} q(x, t_1)dx = \int_{t_1}^{t_2} q(x_1, t)u(x_1, t)dt - \int_{t_1}^{t_2} q(x_2, t)u(x_1, t)dt. \tag{2.7}$$

2.3 Hyperbolic Conservation Laws

To derive the numerical structure which will be employed in this thesis a linear system in Cartesian coordinates is considered first. Let $\mathbf{Q}(x,t)$ be a vector of conserved quantities be governed by the system of hyperbolic conservation laws

$$\frac{\partial \mathbf{Q}}{\partial t} + A\frac{\partial \mathbf{Q}}{\partial x} = \mathbf{0}, \tag{2.8}$$

together with the initial state

$$\mathbf{Q}(x,0) = \mathbf{Q}_0,$$

where A is a constant matrix. The system of equations may be decoupled if the matrix A can be diagonalized. This is possible provided that we can write

$$\Lambda = R^{-1}AR,$$

where R and Λ are the right eigenvector matrix (whose columns are eigenvectors) and a diagonal matrix containing the eigenvalues respectively. In this case a new variable $\mathbf{W} = R^{-1}\mathbf{Q}$, called the characteristic vector, may be introduced and the above system of equations may be written as

$$\frac{\partial \mathbf{W}}{\partial t} + \Lambda\frac{\partial \mathbf{W}}{\partial x} = \mathbf{0}. \tag{2.9}$$

This system is now decoupled and may be written as a set of linear advection equations provided by

$$\frac{\partial w_i}{\partial t} + \lambda^i\frac{\partial w_i}{\partial x} = 0, \;\; i = 1, 2, \ldots, m, \tag{2.10}$$

where λ^i is the i^{th} eigenvalue and m is the number of conservation laws. To find the solution for w^i consider the rate of change of w^i along some characteristic curve $x(t)$:

$$\frac{d}{dt}w^i(x(t),t) = \frac{\partial w^i}{\partial t} + x'(t)\frac{\partial w^i}{\partial x}.$$

If $x'(t) = \lambda^i$ then $w^i(x(t),t)$ is constant, that is to say that w^i is constant on the characteristic curve $x = x_0 + \lambda^i t$. This allows us to solve for w^i from its initial conditions. Recall that $\mathbf{Q}(x,0) = \mathbf{Q}_0(x)$ so the initial condition for the characteristic variables $\mathbf{W}$ is just

$$\mathbf{W}(x,0) = R^{-1}\mathbf{Q}_0(x), \;\; w^i(x,0) = \boldsymbol{l}^i.\mathbf{Q}_0(x), \tag{2.11}$$

where $\boldsymbol{l}^i$ is the i^{th} left eigenvector of the matrix A (the i^{th} row of R^{-1}) and . represents the scalar product. In the case of isothermal gas dynamics the eigenvalue and eigenvector

matrices are given by

$$\Lambda = \begin{pmatrix} u-c & 0 \\ 0 & u+c \end{pmatrix},$$

$$R = \begin{pmatrix} -u-c & 1 \\ u-c & 1 \end{pmatrix},$$

$$R^{-1} = \frac{1}{2c}\begin{pmatrix} -1 & 1 \\ -u+c & u+c \end{pmatrix}.$$

Since $w^i(x_0, 0)$ can be found from equation (2.11) the solution for $w^i(x,t)$ can be provided as

$$w^i(x_0, 0) = w^i(x - \lambda^i t, 0) = w^i(x,t). \tag{2.12}$$

The solution $w^i(x,t)$ is just the initial condition $w^i(x,0)$ propagated at a speed $\left|\lambda^i\right|$, the direction of propagation is determined by the sign of λ^i. So the solution to the linear system given in equation (2.8) is provided by

$$\mathbf{Q}(x,t) = \sum_{i=1}^{m} w^i(x - \lambda^i t, 0)\boldsymbol{r}^i, \tag{2.13}$$

where $\boldsymbol{r}^i$ is the i^{th} right eigenvector of the matrix A (the i^{th} column of R). The state vector $\mathbf{Q}$ may therefore be seen as the linear superposition of the right eigenvectors of the coefficient matrix A with w^i as the weights.

Now consider the system of conservation laws (2.8) in the instance where the initial data of $\mathbf{Q}$ is discontinuous (a Riemann problem), say

$$\mathbf{Q}(x,0) = \begin{cases} \mathbf{Q}_l \text{ if } x < 0, \\ \mathbf{Q}_r \text{ if } x > 0. \end{cases} \tag{2.14}$$

This will correspond to the discontinuous characteristic provided by

$$\mathbf{W}(x,0) = \begin{cases} \mathbf{W}_l \text{ if } x < 0, \\ \mathbf{W}_r \text{ if } x > 0. \end{cases} \tag{2.15}$$

In this case the solution of the i^{th} characteristic equation is simply provided by

$$w^i(x,t) = \begin{cases} w_l^i \text{ if } x - \lambda^i t < 0, \\ w_r^i \text{ if } x - \lambda^i t > 0. \end{cases} \tag{2.16}$$

Again we have that $w^i(x,t)$ is constant on the characteristic curves $x = x_0 + \lambda^i t$ and the solution to the system of equations (2.8) is again provided by equation (2.13) with the

difference being that w^i jumps from one state to the next across the i^{th} characteristic curve.

From the solution we see that across each characteristic the solution jumps from the left state to the right whenever $x - \lambda^i t$ switches signs; in the case of the i^{th} characteristic the jump in $\mathbf{Q}$ is provided by

$$\left(w_r^i - w_l^i\right) \mathbf{r}^i = \alpha^i \mathbf{r}^i. \tag{2.17}$$

An extremely important result here is that the jumps in $\mathbf{Q}$ must be eigenvectors of A since they are just scalar multiples of $\mathbf{r}^i$.

If the jumps in $\mathbf{Q}$ are denoted as $\boldsymbol{\mathcal{W}}^i = \alpha^i \mathbf{r}^i$ then the solution $\mathbf{Q}(x,t)$ may be expressed in terms of jumps as

$$\begin{aligned} \mathbf{Q}(x,t) &= \mathbf{Q}_l + \sum_{i:x<\lambda^i t} \boldsymbol{\mathcal{W}}^i \\ &= \mathbf{Q}_r - \sum_{i:x>\lambda^i t} \boldsymbol{\mathcal{W}}^i. \end{aligned}$$

This form of the solution is important in the derivation of the numerical schemes considered here.

Now, if we were to consider equation (2.8) in conserved form,

$$\frac{\partial \mathbf{Q}}{\partial t} + \frac{\partial \mathbf{F}(\mathbf{Q})}{\partial x} = 0, \tag{2.18}$$

where $\mathbf{F} = A\mathbf{Q}$. A jump in $\mathbf{F}$ is just defined as

$$\begin{aligned} \mathbf{F}_r - \mathbf{F}_l &= A\left(\mathbf{Q}_r - \mathbf{Q}_l\right) = \sum_i \left(w_r^i - w_l^i\right) A\mathbf{r}^i \\ &= \sum_i \left(q_r^i - q_l^i\right) \mathbf{l}^i A \mathbf{r}^i = \Lambda\left(\mathbf{Q}_r - \mathbf{Q}_l\right), \end{aligned} \tag{2.19}$$

where $\mathbf{l}^i$ is the i^{th} left eigenvector of the matrix A. For a general system of hyperbolic conservation laws equation (2.19) would read

$$\mathbf{F}_r - \mathbf{F}_l = \Lambda\left(\mathbf{Q}_r - \mathbf{Q}_l\right). \tag{2.20}$$

Equation (2.20) represents the Rankine-Hugoniot condition. The conditions are necessary to connect the two sides of a discontinuity in a manner that is consistent with the strong form of the hyperbolic conservation laws. The Rankine-Hugoniot condition also describes the speed at which discontinuities propagate; they are a vital feature required in numerical methods so that shock speeds are properly computed in a simulation. It

should be noted that if we know the left and right states of the vector $\mathbf{Q}$ then we may find the speed of the shock by solving the system (2.20) to obtain a single shock speed λ.

2.3.1 Domain of Dependence and Range of Influence

Consider the value of $\mathbf{Q}$ at some point in space and time (X, T), the solution at that point is determined purely by the initial data $\mathbf{Q}_0$ as shown in the solution (2.13). This is obtained (through the initial characteristic data) by the points $X - \lambda^i T$ and the set of all the points $X - \lambda^i T$ for $i = 1, 2, \ldots, m$ is called the domain of dependence – this plays a vital role in the CFL condition which is a necessary condition for a solution to be convergent. Outside of this domain the value of the initial data has no effect on the value of $\mathbf{Q}$ at the point (X, T).

2.4 Finite Volume Methods for Hyperbolic Conservation Laws

The focus of this Section is the derivation of the discrete equations to be solved using the finite volume method. In general hyperbolic conservation laws with a source term may be written as

$$\frac{\partial \mathbf{Q(r,t)}}{\partial t} + \nabla . F(\mathbf{Q(r,t)}) = \mathbf{S}(\mathbf{r}, t, \mathbf{Q(r,t)}). \tag{2.21}$$

In the multidimensional case F is the stress-energy tensor which reduces to a vector in the case of one-dimensional flow. As mentioned above, the integral form of the conservation laws are particularly useful because they are valid in the presence of discontinuities. In particular, the structure of the spatial integration suggests the most feasible numerical structure to be used; this will be shown for the spherically symmetric and the axisymmetric cases.

The manner in which the hydrodynamic equations evolve in time is determined by the type of numerical method use to update the time – backward Euler and Runge-Kutta time stepping will be discussed. Recall that the integral form of the general equations (2.21) can be written as

$$\int_{\Delta V} \mathbf{Q}(\mathbf{r}, t^{n+1}) dV - \int_{\Delta V} \mathbf{Q}(\mathbf{r}, t^n) dV + \int_{t^n}^{t^{n+1}} \int_{\Delta V} \mathbf{F}(\mathbf{Q}) dV dt = \int_{t^n}^{t^{n+1}} \int_{\Delta V} \mathbf{S} dV dt. \tag{2.22}$$

In this form the equations are valid in some volume element ΔV across the two times t^n and t^{n+1}. Using the divergence theorem it is possible to avoid having to calculate (particularly approximate) the divergence of the flux. In this way the form of equation (2.22) may be slightly simplified to

$$\int_{\Delta V} \mathbf{Q}(\mathbf{r}, t^{n+1}) dV - \int_{\Delta V} \mathbf{Q}(\mathbf{r}, t^n) dV + \int_{t^n}^{t^{n+1}} \int_{\partial \Delta V} \mathbf{F}(\mathbf{Q}).\mathbf{dS} dt = \int_{t^n}^{t^{n+1}} \int_{\Delta V} \mathbf{S} dV dt,$$

where $\mathbf{F}.\mathbf{dS}$ has its usual meaning and $\partial \Delta V$ is the boundary of the volume element. The main difficulty in solving equations in hydrodynamics involves the calculation of the time integrals of the flux and source terms. Performing this integration may be avoided entirely by considering a slightly weaker form of the conservation law provided by

$$\int_{\Delta V} \frac{d\mathbf{Q}}{dt} dV + \int_{\partial \Delta V} \mathbf{F}(\mathbf{Q}).\mathbf{dS} = \int_{\Delta V} \mathbf{S} dV. \tag{2.23}$$

This form of the conservation laws has an attractive flux and source terms need not be approximated across a time step and as such numerical methods for nonlinear coupled ordinary differential equations may be used to solve the equations with higher order temporal accuracy. An example of such an instance is the Runge-Kutta time-stepping employed by Shu and Osher in their development of the essentially non-oscillatory schemes [41]. The caveat to this is that the flux and source terms must be approximated in a manner consistent with the theory discussed in the previous Section in order for the time-stepping technique to evolve the conservation laws correctly.

Since the equations are to be approximated on some computational grid, only some approximate value of $\mathbf{Q}$ will be known in a particular volume element (i.e. grid cell). In Godunov type methods this is assumed to be constant in each cell [42]. There are higher order schemes in which $\mathbf{Q}$ is approximated by continuous functions: the MUSCL scheme of van Leer [43] regards $\mathbf{Q}$ as a linear function in each cell while the PPM scheme of Colella and Woodward [39] approximates $\mathbf{Q}$ as a parabola in each cell. Other approaches include the piecewise hyperbolic method of Marquina [44]. In Chapter 4 we will discuss the MUSCL scheme in deeper detail as it will be used to perform the simulations in that chapter.

Inside a particular grid cell the conservation laws for the average of $\mathbf{Q}$ is provided by

$$\frac{1}{\Delta V} \frac{\partial}{\partial t} \int_{\Delta V} \mathbf{Q} dV + \frac{1}{\Delta V} \int_{\Delta V} \nabla . F(\mathbf{Q}) dV = \frac{1}{\Delta V} \int_{\Delta V} \mathbf{S} dV.$$

If we define the cell average in the grid cell as

$$\tilde{\mathbf{Q}} = \frac{1}{\Delta V} \int_{\Delta V} \mathbf{Q} dV, \tag{2.24}$$

the conservation law for the $\tilde{\mathbf{Q}}$ is then provided by

$$\frac{\partial \tilde{\mathbf{Q}}}{\partial t} + \frac{1}{\Delta V}\int_{\partial \Delta V} F(\mathbf{Q}).\mathbf{dS} = \frac{1}{\Delta V}\int_{\Delta V} \mathbf{S} dV, \tag{2.25}$$

where $\partial \Delta V$ is the boundary of the volume element. So, in a three-dimensional grid we would consider the indices, $\{i, j, k\}$ which specify a volume element ΔV_{ijk} – this is bounded by the surfaces $S_{i\pm 1/2jk}, S_{ij\pm 1/2k}$ and $S_{ijk\pm 1/2}$. Indices with half integers represent a position on an interface of a cell. As an example consider the numerical simulation of the hydrodynamic equations in spherical coordinates: the computational grid consists of a spherical cell whose radius is determined by the spatial step Δr the cells which follow are spherical shells of thickness Δr (in the case of a uniform grid).

For one-dimensional flow the general system of conservation laws for the averages in the i^{th} cell is provided by

$$\frac{d\tilde{\mathbf{Q}}_i}{dt} + \frac{\mathbf{F}_{i+1/2}S_{i+1/2} - \mathbf{F}_{i-1/2}S_{i-1/2}}{\Delta V_i} = \frac{1}{\Delta V_i}\int_{\Delta V_i} \mathbf{S} dV, \tag{2.26}$$

or equivalently, by integrating with respect to time from t^n to t^{n+1}:

$$\tilde{\mathbf{Q}}_i^{n+1} = \tilde{\mathbf{Q}}_i^{n} - \int_{t^n}^{t^{n+1}} \frac{\mathbf{F}_{i+1/2}S_{i+1/2} - \mathbf{F}_{i-1/2}S_{i-1/2}}{\Delta V_i} dt = \int_{t^n}^{t^{n+1}} \frac{1}{\Delta V_i}\int_{\Delta V_i} \mathbf{S} dV dt. \tag{2.27}$$

Notice in equation (2.22) that we have recovered the strong integral form of the conservation laws. In this instance though, it refers to the conservation of the quantities $\mathbf{Q}$ in the volume element ΔV_i.

In the case of spherical coordinates the volume and surface elements around the i^{th} cell are provided by

$$\Delta V_i = \int_{r_{i-1/2}}^{r_{i+1/2}} 4\pi r^2 dr = \frac{4\pi}{3}\left(r_{i+1/2}^3 - r_{i-1/2}^3\right),$$

and

$$S_{i\pm 1/2} = 4\pi r_{1\pm 1/2}^2.$$

The resulting discrete system my be written as

$$\frac{d\tilde{\mathbf{Q}}_i}{dt} = -\frac{3\left(r_{i+1/2}^2\tilde{\mathbf{F}}_{i+1/2} - r_{i-1/2}^2\tilde{\mathbf{F}}_{i-1/2}\right)}{r_{i+1/2}^3 - r_{i-1/2}^3} + \frac{3\int_{r_{i-1/2}}^{r_{i+1/2}} \mathbf{S} r^2 dr}{r_{i+1/2}^3 - r_{i-1/2}^3} \tag{2.28}$$

for equation (2.26) and

$$\tilde{\mathbf{Q}}_i^{n+1} = \tilde{\mathbf{Q}}_i^{n} - \Delta t\frac{3\left(r_{i+1/2}^2\tilde{\mathbf{F}}_{i+1/2} - r_{i-1/2}^2\tilde{\mathbf{F}}_{i-1/2}\right)}{r_{i+1/2}^3 - r_{i-1/2}^3} + \Delta t\tilde{\mathbf{S}}_i \tag{2.29}$$

for equation (2.29). It is important to note that while the numerical flux $\tilde{\mathbf{F}}$, in both these equations are numerical approximations of the flux, in equation (2.28) the approximation does not involve time integration but in equation (2.29) it does.

The updating formulas (2.28) and (2.29) implicitly state that an increase in the cell averages is dependent on the difference of the net flux passing through the interfaces. Recalling that the flux differences can be related to the jumps $\boldsymbol{\mathcal{W}}^i$ and the speeds at which they propagate λ^i through equation (2.19), equation (2.29) can be written as

$$\tilde{\mathbf{Q}}_i^{n+1} = \tilde{\mathbf{Q}}_i^n - \Delta t \sum_{p=1}^{N} \frac{3\left(r_{i+1/2}^2 (\lambda^p)^+ \boldsymbol{\mathcal{W}}_{i+1/2}^p - r_{i-1/2}^2 (\lambda^p)^- \boldsymbol{\mathcal{W}}_{i-1/2}^p\right)}{r_{i+1/2}^3 - r_{i-1/2}^3} + \Delta t \tilde{\mathbf{S}}_i. \tag{2.30}$$

In the above equation the following should be noted:

$$\lambda^+ = \max(\lambda, 0), \quad \lambda^- = \min(\lambda, 0).$$

If we define the total effect (at the $(i-1/2)^{th}$ interface) of all the right and left-going waves as $\mathcal{A}^+\Delta\mathbf{Q}_{i-1/2}$ and $\mathcal{A}^-\Delta\mathbf{Q}_{i-1/2}$ respectively then the flux at time t^n may be

$$\tilde{\mathbf{F}}_{i-1/2} = \mathbf{F}(\mathbf{Q}_{i-1}^n) + \mathcal{A}^-\Delta\mathbf{Q}_{i-1/2}^n, \tag{2.31}$$

where $\mathcal{A}^-\Delta\mathbf{Q}_{i-1/2}^n = \sum_p^N (\lambda^p)^- \boldsymbol{\mathcal{W}}_{i-1/2}^p$. It may also be written as

$$\tilde{\mathbf{F}}_{i-1/2} = \mathbf{F}(\mathbf{Q}_i^n) - \mathcal{A}^+\Delta\mathbf{Q}_{i-1/2}^n, \tag{2.32}$$

where $\mathcal{A}^-\Delta\mathbf{Q}_{i-1/2}^n = \sum_p^N (\lambda^p)^+ \boldsymbol{\mathcal{W}}_{i-1/2}^p$. The form of these fluxes allows for more robust numerical methods to be derived and this approach forms the very basis of the development of higher order methods [45].

2.4.1 Elements of Stability

The notions of consistency, stability and convergence are important in numerical methods; this is no different for the numerical methods for hyperbolic conservation laws. While a von Neumann stability analysis is an extremely useful tool for investigating numerical methods for linear problems it tends to be of little value in the analysis of numerical methods for hyperbolic problems. This is due to the fact that the numerical flux – in general – depends on the solution in a nonlinear way. As such alternative methods are required. Fortunately, due to the Lax-Wendroff theorem if we can show consistency of the numerical method (that is that the numerical method reduces to the original differential equation being solved when the time step Δt and the space step

Δx tend to zero) and stability – by some measure – then we are guaranteed that the numerical solution will converge to a weak solution [45]. For the sake of illustration we will use the upwind scheme to describe the discussed stability properties. The use of this scheme in our illustrations is valid due to the fact that both the Roe and Marquina flux formulae are based on the upwind scheme.

2.4.1.1 The CFL Condition

A condition that can easily be imposed on a numerical method is the CFL condition [46]. It states that a necessary (but not sufficient) condition for a numerical method to be convergent is that the numerical domain of dependence of a partial differential equation must contain the true domain of dependence in the limit as the temporal and spatial steps tend to zero.

In the case of a system of conservation laws (in spherical coordinates) the domain of dependence for a point (R, T) is given as defined before by the set

$$\mathcal{D}(R,T) = \{R - \lambda^1 T, R - \lambda^2 T, ..., R - \lambda^N T\}, \tag{2.33}$$

where λ^i is the i^{th} eigenvalues of the Jacobian of the flux. By the CFL condition if we let $\sigma = \frac{\Delta t}{\Delta r}$ and we have the numerical domain of dependence provided by

$$\mathcal{D}_N(R,T) = [R - T/\sigma; R + T/\sigma], \tag{2.34}$$

then $\mathcal{D}$ must be contained in $\mathcal{D}_N$. This is only possible if

$$\nu = \left| \frac{\max(\lambda^i)\Delta t}{\Delta r} \right|. \tag{2.35}$$

Thus we arrive at the CFL condition for a system of hyperbolic conservation laws.

2.4.1.2 Consistency

Another important aspect to guide us in the analysis of numerical methods of a hyperbolic conservation law is the consistency of the numerical method. This is related to the equivalent equation of the scheme in that it represents the partial differential equation that a numerical method in question would solve exactly. As an example we consider the equivalent equation of the upwind scheme on the linear equation

$$u_t + a u_x = 0.$$

The upwind scheme for this problem may be written as

$$\frac{U_i^{n+1} - U_i^n}{\Delta t} + a\frac{U_i^n - U_{i-1}^n}{\Delta x} = 0.$$

Then the equivalent equation is found by first expressing the approximate solution U_i^n in terms of the exact solution $u(x,t)$

$$\frac{u(x,t+\Delta t) - u(x,t)}{\Delta t} + a\frac{u(x,t) - u(x-dx,t)}{\Delta x} = 0$$

and then take a Taylor expansion about the independent variables. This results in the following equation

$$u_t + au_x = \frac{1}{2}a(dx - adt)u_{xx}, \tag{2.36}$$

after replacing $u_{tt} = a^2 u_{xx}$ which was found by differentiating the original linear advection equation with respect to time. Equation (2.36) contains very useful information: we note, firstly that the upwind scheme is diffusive. Secondly, the coefficient of u_{xx}, $\frac{1}{2}a(dx - adt)$ confirms the CFL condition – if $dx - adt < 0$ that is if $\frac{adt}{dx} > 1$ the equivalent equation would be a negative diffusion equation which is known to break down.

2.4.1.3 One-Norm Stability

While finding the equivalent equations offers insight into the consistency of a particular scheme it does not offer insight into the stability properties of the scheme. The one-norm is often used as a measure of the stability of a scheme (particularly in the case of nonlinear equations [45]) in the following way: A scheme is said to be stable in the one-norm if

$$\|U^{n+1}\|_1 \leq \|U^n\|_1, \tag{2.37}$$

with $\|U\| = \Delta x \sum_i |U_i|$. In the case of the upwind scheme we have

$$\begin{aligned}
\|U^{n+1}\| &= \Delta x \sum |U_i^{n+1}| \\
&= \Delta x \sum |U_i^n - a\frac{\Delta t}{\Delta x}\left(U_i^n - U_{i-1}^n\right)| \\
&\leq \Delta x \sum_i \left(1 - a\frac{\Delta t}{\Delta x}\right)|U_i^n| + \Delta x \sum_i a\frac{\Delta t}{\Delta x}|U_{i-1}^n| \\
&\leq \left(1 - a\frac{\Delta t}{\Delta x}\right)\|U^n\|_1 + a\frac{\Delta t}{\Delta x}\|U^n\|_1 \\
&\leq \|U^n\|_1.
\end{aligned}$$

Thus we have shown that the upwind scheme is stable in the 1-norm.

2.4.1.4 TVD Stability

Another property of a scheme that is a measure of stability is its total variation; the total variation of a continuous and differentiable function q is provided by

$$TV(q) = \int_{-\infty}^{\infty} |q'(x)|dx.$$

The discretized version of the total variation is stated as

$$TV(Q) = \sum_{i} |Q_i - Q_{i-1}|. \tag{2.38}$$

A numerical scheme is said to be "total variation bound" if for some initial date Q^0 with $TV(Q^0) < \infty$ and a time T, there is a constant $\mathcal{R}$ and a value $\Delta t_0 > 0$ such that

$$TV(Q^n) \leq \mathcal{R}$$

for all $n\Delta t \leq T$ whenever $\Delta t < \Delta t_0$. The scheme is said to be "total variation diminishing" if $TV(Q^{n+1}) \leq TV(Q^n)$.

2.4.2 Artificial Fragmentation

Next, we discuss a more subtle form of stability in terms of the numerical simulation of star formation. Due to the nature of the collapse the density in a grid cell (or a collection of grid cells) can increase many orders of magnitude from its original value. The increase is accelerated as more and more mass collapses into the cell at faster and faster rates. In order to run simulations beyond the stage where the forming core is no longer isothermal (and the isothermal equations no longer apply) a number of techniques which either modify the equation of state or alter the computational grid have been introduced by various authors. Boss [33] used the equation of state $P = P_T \left(\rho/\rho_T\right)^{1.4}$ (where $\rho_T = 3 \times 10^{-13} gcm^{-3}$) to allow for the collapse to continue into the near non-isothermal regime. On the other hand Boss and Black [47] introduced the "sink cell method" in which the cells where the density exceeds some isothermal threshold density (like ρ_T) are removed from the grid. Calculations regarding such core forming regions are therefore avoided and the hydrodynamic simulation of the rest of the collapsing cloud may continue.

Truelove et al. [2] showed that in order for a simulation to demonstrate the true nature of a collapsing cloud, the cell sizes would need to be have the following property:

$$\frac{\Delta x}{\lambda_J} \leq 0.25, \tag{2.39}$$

where Δx is the grid cell width and λ_J is the local Jeans number in that cell. They showed that if this condition is not met then artificial fragmentation could occur inside the cell giving rise to the formation of artificial cores.

2.5 Source Terms

Source terms play an important part in the simulation of star formation and they require special attention in the numerical solution. There are two types of source terms to be aware of when solving the relevant conservation laws: geometric source terms which arise purely from the choice of a coordinate system and source terms which contribute to the description of the physical model. Both of these terms are involved in the simulation of isothermal collapse. Numerically, the source terms can be approximated in the same time step as the flux terms – as shown in equations (2.28) and (2.29). Alternatively the terms could be approximated in a second time step that is free of the flux terms as follows

$$\begin{aligned} \tilde{\mathbf{Q}}_i^* &= \tilde{\mathbf{Q}}_i^n - \Delta t \frac{3\left(r_{i+1/2}^2 \tilde{\mathbf{F}}_{i+1/2} - r_{i-1/2}^2 \tilde{\mathbf{F}}_{i-1/2}\right)}{r_{i+1/2}^3 - r_{i-1/2}^3} \\ \tilde{\mathbf{Q}}_i^{n+1} &= \tilde{\mathbf{Q}}_i^* + \Delta t \mathbf{S}(\mathbf{Q}_i^*, r_i, t^n). \end{aligned}$$

Note that this does not change the system of conservation laws: substitution of one of these equations into the other would reduce to a single time-step method. This separation of the flux and source terms is similar to attributing an equation for each of the respective parts:

$$\begin{aligned} \frac{\partial \mathbf{Q}}{\partial t} + \nabla . \mathbf{F}(\mathbf{Q}) &= 0, \\ \frac{\partial \mathbf{Q}}{\partial t} &= \mathbf{S}(\mathbf{Q}, \mathbf{r}, t). \end{aligned}$$

There are benefits and drawbacks to each approach. Updating both fluxes and sources in a single time step is computationally efficient but a truly higher order scheme would be difficult to derive as the numerical methods for hyperbolic conservation laws is based on sourceless equations; in general a system in the form

$$\frac{\partial \mathbf{Q}}{\partial t} + A \frac{\partial \mathbf{Q}}{\partial x} = B\mathbf{Q}$$

cannot be decoupled because A and B cannot be simultaneously diagonalized with a characteristic variable. On the other hand treating the system as separate equations allows for the best techniques for each term to be used. A caveat to this is that the

geometric source terms should always be considered in conjunction with the source terms, so as to avoid the generation of artificial phenomena during the simulation.

2.5.1 Geometric Source Terms

When considering the system of hydrodynamic equations of spherically symmetric collapse the geometric source term appears in the radial momentum equation

$$\frac{\partial \rho u}{\partial t} + \frac{1}{r^2}\frac{\partial}{\partial r}\left(r^2(\rho u^2 + \rho c^2)\right) = \frac{2\rho c^2}{r} - \rho\frac{\partial \Phi}{\partial r}.$$

The geometric source term is $\frac{2\rho c^2}{r}$. Using the finite volume method these terms could be approximated using the trapezoidal rule:

$$\frac{1}{\Delta V_i}\int_{r_{i-1/2}}^{r_{i+1/2}} \left(\frac{2\rho c^2}{r}\right) 4\pi r^2 dr \approx \frac{3\left(r_{i+1/2}\rho_{i+1/2} + r_{i-1/2}\rho_{i-1/2}\right)c^2}{r_{i+1/2}^3 - r_{i-1/2}^3}.$$

However, it turns out that this approximation is not suitable as $r \to 0$ and a more appropriate approximation is provided by

$$\frac{1}{\Delta V_i}\int_{r_{i-1/2}}^{r_{i+1/2}} \left(\frac{2\rho c^2}{r}\right) 4\pi r^2 dr \approx \frac{3\rho_i c^2\left(r_{i+1/2}^2 - r_{i-1/2}^2\right)}{r_{i+1/2}^3 - r_{i-1/2}^3}.$$

This approximation can be viewed as taking ρ as constant in the cell being integrated in which case the integration portion is just $\int r dr$. To see why this approach is better we consider a series expansion (around $dr = 0$) of each of the terms to second order:

$$\frac{3\left(r_{i+1/2}\rho_{i+1/2} + r_{i-1/2}\rho_{i-1/2}\right)c^2}{r_{i+1/2}^3 - r_{i-1/2}^3} \approx \frac{2\rho c^2}{r} + dr^2\left(-\frac{\rho c^2}{6r^3} + \frac{2\rho_r + r\rho_{rrr}}{4r^2}\right) + O(dr^3), \quad (2.40)$$

by ρ_r we mean the derivative of ρ with respect to r. For the second approximation we obtain

$$\frac{3\rho_i c^2\left(r_{i+1/2}^2 - r_{i-1/2}^2\right)}{r_{i+1/2}^3 - r_{i-1/2}^3} \approx \frac{2\rho c^2}{r} + dr^2\left(-\frac{\rho c^2}{6r^3}\right) + O(dr^3). \quad (2.41)$$

The additional terms seen in equation (2.40) cause a numerical instability near the origin which causes the density at $r = 0$ to increase indefinitely in the absence of a gravitational field.

2.5.2 Gravitational Potential

Gravity is the driving force behind isothermal collapse with most other forces being opposed to it. It is a particularly difficult source term to handle due to the fact that the

gravitational potential is governed by the Poisson equation:

$$\nabla^2\Phi = 4\pi G\rho. \tag{2.42}$$

So the accuracy to which we can approximate Φ is dependent on two things: the numerical method we use to solve the Poisson equation and the accuracy with which the density ρ, is solved from the hyperbolic conservation laws. While equation (2.42) is linear, difficulties arise when the coordinate system is not Cartesian – for cylindrical and spherical coordinates care must be taken near $r = 0$ due to the singularity in the Poisson equation. Another difficulty occurs due to the fact that it is a second order partial differential equation which means that it can rapidly become computationally costly to solve. Given these issues, a number of numerical techniques have been developed to solve the Poisson equation (to find the gravitational potential) in as efficient a manner as possible.

In one-dimensional spherically symmetric collapse the Poisson equation is avoided entirely by using the fact that the structure of the gravitational potential is known:

$$\Phi = -\frac{GM_r}{r},$$

where M_r is the mass contained in a sphere of radius r. The mass may be found either by integrating the conservation of mass equation

$$\frac{\partial M_r}{\partial r} = 4\pi r^2\rho,$$

as has been done by most authors [19, 48, 49]. An alternative way, which is well suited to the time stepping structure of the hyperbolic part of the conservation laws, is to consider the continuity equation in spherical geometry and assume spherical symmetry:

$$\frac{\partial \rho}{\partial t} + \frac{1}{r^2}\frac{\partial}{\partial r}(r^2\rho u) = 0,$$

if we integrate this equation from the origin to some radius r we find an equation for the mass inside a sphere of radius r provided by:

$$\frac{\partial M_r}{\partial t} + 4\pi r^2\rho u = 0. \tag{2.43}$$

The form of this equation is convenient as it requires no approximation of spatial derivatives. Upon considering two-dimensional flow, the gradient of the potential is required in both directions of flow. In this case an alternative approach is needed to find the components of the gravitational force.

2.5.2.1 Direct Method

In the direct approach the Poisson equation is discretized and then solved numerically. A variety of methods are available for this approach; standard finite difference methods for instance, where the ADI method is a common example. Pseudospectral methods can also be used and are very effective in situations where Cartesian coordinates are employed. In general however, these are not the approaches employed. Due to the linear structure of the Laplacian it is generally possible to take a multipole expansion of the gravitational potential.

2.5.2.2 Multipole Expansion

For cylindrical coordinates many authors have used the multipole expansion to approximate the gravitational potential at the boundary of the system then numerically integrate the Poisson equation to find the potential at the interior points [50].

The spherical harmonic expansion is a method long used method in simulations performed in spherical coordinates, see [33]. The method entails expanding the density in terms of the spherical harmonic functions $Y_{lm}(\theta, \phi)$ and then solving for the weights $R_{lm}(r)$ for the gravitational potential. As such we consider

$$\Phi(r, \theta, \phi) = \sum_{l=0}^{\infty} \sum_{m=-l}^{l} \Phi_{lm}(r) Y_{lm}(\theta, \phi)$$

$$\rho(r, \theta, \phi) = \sum_{l=0}^{\infty} \sum_{m=-l}^{l} \rho_{lm}(r) Y_{lm}(\theta, \phi),$$

where ρ is the density, ρ_{lm} is a weight function and $Y_{lm}(\theta, \phi)$ are the spherical harmonics. Then the equation for Φ_{lm} can be shown to be

$$\Phi''_{lm} + \frac{2}{r}\Phi'_{lm} - \frac{l(l-1)}{r^2}\Phi_{lm} = 4\pi G \rho_{lm}. \tag{2.44}$$

Each equation is then solved using an appropriate numerical method. It should be noted that in practice only a few moments are taken: Boss in [33] found that $l \leq 6$ was sufficient for the numerical simulations he performed. An additional simplification arises when there is symmetry in the density field, for instance in the case of axisymmetry l is always even.

2.5.2.3 Diffusion Equation Approach

One of the techniques used by Bodenheimer and Black [10] is to solve a diffusive version of the Poisson equation provided by

$$\frac{\partial \Phi}{\partial t} = \nabla^2 \Phi - 4\pi G\rho.$$

The boundary condition used is related to the technique which uses a multipole expansion of the outer boundary. The solution to the Poisson equation at the outer boundary is easy to calculate since it must match the solution for the Poisson equation for a vacuum which is provided by

$$\nabla^2 \Phi = 0.$$

Using the solution to this equation as a boundary condition and solving the diffusion equation until a steady-state is reached provides the solution for the gravitational potential. The problem with such an approach is that the steady-state of the diffusive equation must be found at each time step of the hydrodynamic equations which is computationally expensive even when implicit techniques allow for larger time steps to be used.

2.5.2.4 Conservative Approach

The conventional approach of solving the Poisson equation in order to obtain the components of the gravitational force introduces computational error on two levels: first, error is incurred when solving the Poisson equation and then further error is introduced when differentiating the resulting potential in order to calculate the components of the force. Since only the components of the force are required in the momentum equations it is useful to derive an equation for them instead.

Consider the general Poisson equation for the gravitational field:

$$\nabla^2 \Phi = 4\pi G\rho. \tag{2.45}$$

Differentiating this with respect to time provides

$$\nabla^2 \Phi_t = \nabla . \nabla \Phi_t = 4\pi G\rho_t = -4\pi G \nabla . \left(\rho \mathbf{u}\right),$$

where . represents the scalar product. If we consider a conserved form of this equation we have that

$$\int_V \nabla . \nabla \Phi_t dV = \int_{\partial V} \nabla \Phi_t . \mathbf{dS} = -\int_V 4\pi G\rho \mathbf{u} dV = -\int_{\partial V} 4\pi G\rho \mathbf{u} . \mathbf{dS},$$

again, ∂V is the boundary of the volume of integration.

Thus if the force satisfies the equation

$$\nabla \Phi_t = -4\pi G \rho \mathbf{u}, \tag{2.46}$$

we may relinquish the need to find the gravitational potential and the force may be updated directly from the momentum density field.

It is of anecdotal interest to note that the structure of equation (2.46) is akin to the Einstein field equations in the following manner: consider the equation in component form

$$\Phi_{,i0} = -4\pi G \rho u_i.$$

Here , represent partial differentiation and i cycles through the spatial coordinates and 0 represents the time coordinate. Recalling that the force is related to the gradient of the potential we have that

$$F_{i,t} = -\Phi_{,i0}, \Rightarrow F_{i,t} = 4\pi G T_{i0}.$$

The Einstein equations are given by

$$G_{\mu\nu} = \frac{8\pi G}{c^2} T_{\mu\nu},$$

where $T_{\mu\nu}$ is the stress energy tensor. As long as no external mass is added to the system then equation (2.46) may be interpreted as stating that the rate of change of the force field in a hydrodynamic system is directly proportional to the momentum field.

2.6 Hydrodynamic Equations Governing Spherically Symmetric, Isothermal Collapse

In this Chapter we have discussed the theory of hyperbolic conservation laws highlighting the aspects that will be required in performing numerical simulations of the hydrodynamic equations governing isothermal collapse.

For one-dimensional, spherically symmetric, isothermal collapse the hydrodynamic equations are provided by

$$\frac{\partial \rho}{\partial t} + \frac{1}{r^2}\frac{\partial}{\partial r}\left(r^2 \rho u\right) = 0, \tag{2.47}$$

$$\frac{\partial \rho u}{\partial t} + \frac{1}{r^2}\frac{\partial}{\partial r}\left[r^2\left(\rho u^2 + \rho c^2\right)\right] = \frac{2\rho c^2}{r} - \rho \frac{\partial \Phi}{\partial r}. \tag{2.48}$$

The boundary and initial conditions will be discussed at a later stage. We will solve these equations approximately, using two different numerical approaches: the TVD-MUSCL scheme with a Roe flux and the third-order Runge-Kutta time-stepping scheme with a Marquina flux. While simulations performed with the TVD scheme updates the gravitational field in the same step as the flux, we have used a split scheme for the simulations performed with the Runge-Kutta time-stepping for comparison.

Using the solution for steady-state accretion, which we will derive in the next Chapter, as well as the Truelove criterion as a means of stopping the simulation, we will show that the steady-state solutions may be used as a tool in the determination of the protostellar core properties.

2.7 Concluding Remarks

This Chapter has highlighted the mathematical and computational aspects of hyperbolic conservation laws that will be used in the implementation as well as the analysis of the numerical methods used in our simulation. The Rankine-Hugoniot conditions have been discussed in the context of discontinuous solutions; we will use them to investigate the existence of discontinuous solutions for steady-state accretion in the context of the analytical solutions to be developed in Chapter 3.

Chapter 3

Isothermal Clouds: Stability and Steady-States

In this Chapter the stability conditions for isothermal collapse are discussed. First, we derive the Jeans criterion for collapse relating the result not only to the isothermal sphere but isothermal filaments, in the form of infinite cylinders, and isothermal planes in the form of infinite sheets. We also derive the solutions to the equations for hydrostatic equilibrium of the isothermal sphere, the infinite cylinder and the infinite sheet. The density profiles of these configurations are important for investigating the stability of clouds with a non-uniform density. Lastly, we discuss the importance of steady-state accretion in the process of star formation and introduce new solutions to the equations for steady-state accretion for the configurations mentioned.

3.1 Introduction

Sir James Jeans in his classical 1902 paper [51] considered the stability of an infinitely large isothermal cloud against gravitational collapse. Considering a first order perturbation on the Euler equations for an isothermal gas together with the Poisson equation for the gravitational field, Jeans was able to find the characteristic lengths associated with collapse. This is often regarded as the first mathematical modelling of a star. Because Jeans' approach was inconsistent with Newtonian gravity – due to the assumption of an infinite cloud – many authors attempted to derive a stability criterion for finite isothermal spheres. But it was Bonnor [16] and Ebert [17] who, independently, derived the criterion by considering the perturbations of a hydrostatic, isothermal sphere.

Star formation from non-spherical clouds are also of importance and have been investigated by several authors, see [52–54]. Perturbations of non-spherical clouds for the purpose of investigating gravitational stability are also of importance and the simplest of these non-spherical clouds is the infinite sheet and the infinite cylinder. The solutions for the density profiles of the hydrostatic equilibrium configurations of these two clouds have been found by Spitzer [55] and Ostricker [56] respectively. The fragmentation of such configurations has been investigated by Miyama et al. [53] using linear perturbation theory and later extending to nonlinear effects [57].

Many of the results found by these authors have been used in modern simulations involved in investigating late stage star formation with the aim of embedding protostellar cores into more realistic surroundings and also with the aim of investigating the evolutions of non-spherical fragments. In many of the simulations an accretion rate is required as an initial condition in order to evolve the fragment, and it is common practice to assume a free-fall accretion rate which may be derived from the equations of motion. The inclusion of a pressure in the accretion rate would be useful in that it would give a more accurate description of the movement of the gas being accreted by the fragment. While the solutions of free-fall accretion in most cases is known, the cases which include the pressure are rare with classical Bondi accretion standing out. Bondi investigated the steady-state accretion of gas onto a compact point mass [3] in spherical symmetry. In this paper Bondi related the accretion rate onto the compact object to the density at infinity, the sound speed and the mass of the accreting star. While the Bondi solution (for the velocity) appears both graphically and in implicit form, there has been no closed form solution for the velocity profile. Such a solution would be useful for initial conditions of late stage star formation, that is, after a compact core has formed. Cassen and Pettibone extended the solution of Bondi accretion to include rotation [36]. The three Sections presented here cover the derivation of the Jeans instability criterion, the derivation of the equilibrium profiles for the three mentioned configurations (spheres,

infinite cylinders and sheets) and lastly a novel Section in which the exact solutions for steady-state accretion onto the three simple fragments are presented.

3.2 Jeans Instability

The Jeans instability criterion is derived by investigating a first order perturbation of the fluid equations for self-gravitating isothermal flow. This may be seen by considering the hydrodynamic equations in vector form

$$\frac{\partial \rho}{\partial t} + \nabla.\left(\rho \mathbf{u}\right) = 0 \tag{3.1}$$

$$\frac{\partial \rho \mathbf{u}}{\partial t} + \nabla.\left(\rho \mathbf{u} \otimes \mathbf{u}\right) = -c^2 \nabla \rho - \rho \nabla \Phi, \tag{3.2}$$

where $\otimes$ is the tensor product. The independent variables t and r are the time and the radial distance; the dependent variables ρ and $\mathbf{u}$ are the density and velocity vector fields respectively. The sound speed is c and the gravitational potential Φ is coupled to the hydrodynamic equations by the Poisson equation

$$\nabla^2 \Phi = 4\pi G \rho. \tag{3.3}$$

We first consider motion in just one dimension and then define the linear perturbation in all the quantities as

$$\rho(\xi, t) = \rho_0 + \tilde{\rho}(\xi, t),\ u(\xi, t) = \tilde{u}(\xi, t),\ \Phi = \Phi_0 + \tilde{\Phi}(\xi, t),$$

where ξ is the spatial coordinate in either spherical, cylindrical or Cartesian coordinates. For the sake of brevity all the quantities with a zero subscript are taken as constant. Substituting the perturbed variables into the fluid equations (3.1) and (3.2) and retaining only the first order terms gives

$$\frac{\partial \tilde{\rho}}{\partial t} + \rho_0 \frac{1}{\xi^n} \frac{\partial}{\partial \xi} \left(\xi^n \tilde{u}\right) = 0, \tag{3.4}$$

$$\rho_0 \frac{\partial \tilde{u}}{\partial t} + c^2 \frac{\partial \tilde{\rho}}{\partial \xi} = -\rho_0 \frac{\partial \tilde{\Phi}}{\partial \xi}, \tag{3.5}$$

$$\frac{1}{\xi^n} \frac{\partial}{\partial \xi} \left(\xi^n \frac{\partial \tilde{\Phi}}{\partial \xi}\right) = 4\pi G \tilde{\rho},$$

where $n = 0, 1, 2$ represent the cases of planar, cylindrical and spherical geometry. Differentiating (3.4) with respect to t and operating on (3.5) with $\frac{1}{\xi^n}\frac{\partial}{\partial\xi}\xi^n$ gives

$$\frac{\partial^2\tilde{\rho}}{\partial t^2} + \frac{\rho_0}{\xi^n}\frac{\partial}{\partial\xi}\left(\xi^n\frac{\partial\tilde{u}}{\partial t}\right) = 0 \tag{3.6}$$

and

$$\frac{\rho_0}{\xi^n}\frac{\partial}{\partial\xi}\left(\xi^n\frac{\partial\tilde{u}}{\partial t}\right) = -\frac{c^2}{\xi^n}\frac{\partial}{\partial\xi}\left(\xi^n\frac{\partial\tilde{\rho}}{\partial\xi}\right) - \frac{\rho_0}{\xi^n}\frac{\partial}{\partial\xi}\left(\xi^n\frac{\partial\tilde{\Phi}}{\partial\xi}\right). \tag{3.7}$$

Eliminating $\tilde{u}$ from either of the equations results in a wave equation with a source term for $\tilde{\rho}$,

$$\frac{\partial^2\tilde{\rho}}{\partial t^2} = c^2\frac{1}{\xi^n}\frac{\partial}{\partial\xi}\left(\xi^n\frac{\partial\tilde{\rho}}{\partial\xi}\right) + \rho_0\frac{1}{\xi^n}\frac{\partial}{\partial\xi}\left(\xi^n\frac{\partial\tilde{\phi}}{\partial\xi}\right). \tag{3.8}$$

Substituting the perturbed Poisson equation (3.5) into equation (3.6) provides

$$\frac{\partial^2\tilde{\rho}}{\partial t^2} = c^2\frac{1}{\xi^n}\frac{\partial}{\partial\xi}\left(\xi^n\frac{\partial\tilde{\rho}}{\partial\xi}\right) + 4\pi G\rho_0\tilde{\rho}. \tag{3.9}$$

The equation can be solved in general by assuming the typical ansatz: $e^{i\omega t}$ for the temporal part and for the spatial part we have the complex exponential, the Bessel and the spherical Bessel functions for $n = 0, 1, 2$ respectively with some wave number k. Each of these cases lead to the dispersion relation

$$\omega = \pm\sqrt{k^2c^2 - 4\pi G\rho_0}. \tag{3.10}$$

It can be clearly seen that if ω is complex, that is if

$$k^2 < \frac{4\pi G\rho_0}{c^2}, \tag{3.11}$$

then density perturbations will grow over time and the cloud will collapse. By expressing the wave number as a wave length using the relation $k = \frac{2\pi}{\lambda}$, we may derive the Jeans length, λ_J. In this case the inequality (2.9) reads as follows

$$\lambda > \lambda_J = \sqrt{\frac{\pi c^2}{G\rho_0}}. \tag{3.12}$$

It is important to note that the Jeans instability criterion, (3.12), is independent of the geometry and is valid provided the collapse is taking place in one dimension (two-dimensional collapse would require another wave number). The forms of the instability criterion may be restructured in order to accommodate particular cloud shapes; this will be demonstrated below.

The criterion in (3.12) may be interpreted in a number of ways: two common ways are

in terms of the cloud radius and the cloud mass. Assuming that the characteristic length λ, is the cloud diameter, then in terms of the radius and cloud density the relation reads:

$$R > R_J = \sqrt{\frac{\pi c^2}{4G\rho_0}}.$$

If one assumes that $\rho_0 = \frac{3M}{4\pi R_J^3}$ the following expression for R in terms of the cloud mass is found:

$$R < R_J = \frac{3GM}{c^2\pi^2}. \tag{3.13}$$

It is possible to derive quantities of a similar order using the energy argument or by considering the stability of Bonnor-Ebert spheres – as will be shown in the next Section. In most literature an excepted quantity for R_J is given by

$$R_J = 0.41\frac{GM}{c^2}.$$

It is worth noting that this value is larger than the one quoted in (3.13). This difference will play an important role in the next Chapter where the limits of the cloud radius are more closely scrutinized.

The criterion may also be expressed in terms of the Jeans mass M_J:

$$M > M_J = \frac{4\pi}{3}R_J^3\rho_0 = \frac{\pi^{5/2}}{6\rho_0^{1/2}}\left(\frac{c^2}{G}\right)^{3/2}. \tag{3.14}$$

Note that as the density increases toward the centre the Jeans mass decreases pushing M and M_J further apart and keeping the criterion satisfied.

The form of equation (3.12) is useful in that the appearance of the density allows for the criterion to be extended to filamentary clouds and sheet layers which are commonly modeled (in practice) as infinite cylinders and sheets respectively, see Miyama [53]. For an infinite cylinder it is convenient to refer to line density (mass per unit length) which is simply defined as $\rho_{line} = \pi R^2\rho$ where R is the cylinder radius. Again, treating λ_J as the cylinder diameter gives rise to the following instability criterion:

$$\lambda_J^2 = \frac{\pi c^2}{G\rho_0} \quad \Rightarrow \quad \rho_{line} > \rho_0\pi R_J^2 = \frac{\pi^2 c^2}{4G}. \tag{3.15}$$

An important result here is that the instability criterion is dependent only on the temperature (through the sound speed) and not the density as in the spherical case. Uniform, infinite, isothermal cylinders whose line mass is greater than $\frac{\pi^2 c^2}{4G}$ will collapse. A similar expression is found when considering the hydrostatic infinite cylinder. In the case of infinite sheets the surface density (mass per unit area) takes the place of the mass

and is defined as $\rho_{surf} = \rho_0 L$ where L is the thickness of the sheet. Following the same procedure as above the criterion is easily seen to be

$$\rho_{surf} > \sqrt{\frac{\pi c^2 \rho_0}{4G}}. \tag{3.16}$$

This result is also interesting because while the Jeans mass for a sphere decreases with an increase in density, the mass per unit area increases with density.

3.3 Equilibrium Configurations

In this Section equilibrium configurations are considered. The most important of these is of course the Bonnor-Ebert sphere and as such we will provide the most detail in this instance. Ironically, the density profile of a Bonnor-Ebert sphere has no closed form solution while its counterparts, the hydrostatic, infinite cylinder and sheet have exact solutions. The equations for hydrostatic equilibrium may be derived from the static version of the momentum equation (3.2) and Poisson's equation for the gravitational field provided by

$$0 = -c^2 \frac{d\rho}{d\xi} - \rho \frac{d\Phi}{d\xi}, \tag{3.17}$$

$$\frac{1}{\xi^n} \frac{d}{\xi} \left(\xi^n \frac{d\Phi}{d\xi} \right) = 4\pi G \rho. \tag{3.18}$$

To non-dimensionalize the two equations we consider scaling transformations for each of the variables:

$$\xi = \alpha x, \quad \rho = \beta \bar{\rho}, \quad \Phi = \gamma \theta.$$

For the present moment α, β and γ are just scaling factors to be determined and $x, \bar{\rho}$ and θ are the dimensionless length, density and gravitational potential respectively. Substituting these into the hydrostatic equations gives

$$\begin{aligned} 0 &= -\frac{c^2 \beta}{\alpha} \frac{d\bar{\rho}}{dx} - \frac{\beta \gamma \bar{\rho}}{\alpha} \frac{d\theta}{dx}, \\ \frac{\gamma}{\alpha^2 x^2} \frac{d}{dx} \left(x^2 \frac{d\theta}{dx} \right) &= 4\pi G \beta \bar{\rho}. \end{aligned} \tag{3.19}$$

Rearranging the first of these equations gives

$$c^2 \frac{d \ln \bar{\rho}}{dx} = -\gamma \frac{d\theta}{dx}, \tag{3.20}$$

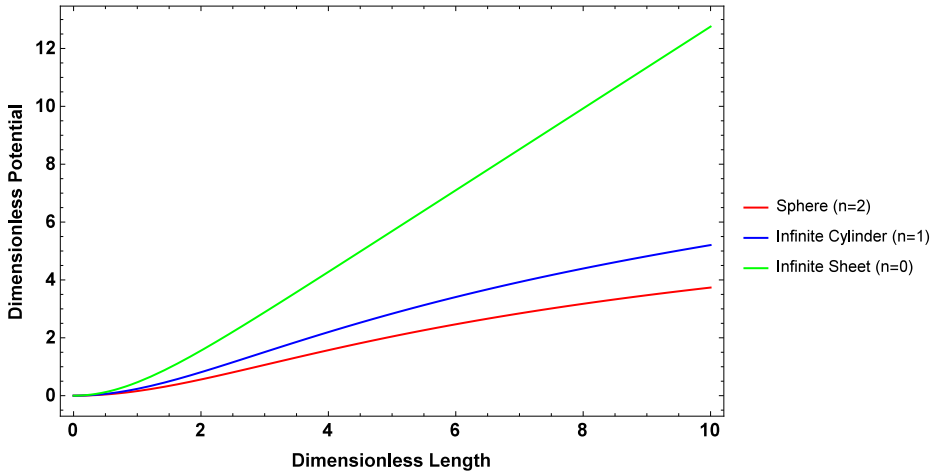


FIGURE 3.1: *The Figure shows plots of the solutions to the isothermal Lane-Emden equation. On the abscissa is the dimensionless length and the dimensionless potential in on the ordinate.*

suggesting that γ be chosen to be c^2. Equation (3.20) also implies that $\bar{\rho} = e^{-\theta}$. Substituting this into the second of equations (3.19) results in the equation

$$\frac{1}{x^n}\frac{d}{dx}\left(x^n\frac{d\theta}{dx}\right) = \frac{4\pi G\beta}{\gamma\alpha^2}e^{-\theta}. \tag{3.21}$$

Given the form of the dimensionless density it is clear that β should be chosen as the central density, ρ_0, that is, the density evaluated at $x = 0$. Since γ has already been chosen it follows that the length scale α must be equal to $\left(\frac{c^2}{4\pi G\rho_0}\right)^{1/2}$. This set of transformations results in the dimensionless Poisson equation provided by

$$\frac{1}{x^n}\frac{d}{dx}\left(x^n\frac{d\theta}{dx}\right) = e^{-\theta}, \quad \theta(0) = \theta'(0) = 0. \tag{3.22}$$

The equation in (3.22) is sometimes referred to as the isothermal Lane-Emden equation – the Dirichlet boundary condition is derived from the relation between the dimensionless density and the dimensionless potential. The Neumann condition is derived from the fact that the gravitational force must vanish in the absence of mass.

The isothermal Lane-Emden equation has analytical solutions for $n = 0$ and $n = 1$, that is, analytical solutions exist for the isothermal Lane-Emden equation in the case of the infinite cylinder and the infinite sheet. For $n = 2$ we have the Lane-Emden equation for the Bonnor-Ebert sphere; this has no analytical solution. Figure 3.1 shows the dimensionless density for each of the considered values of n. The most notable feature is related to the infinite sheet: the dimensionless potential rapidly tends to a linear profile. As a result of the rapid increase in the dimensionless potential the dimensionless density

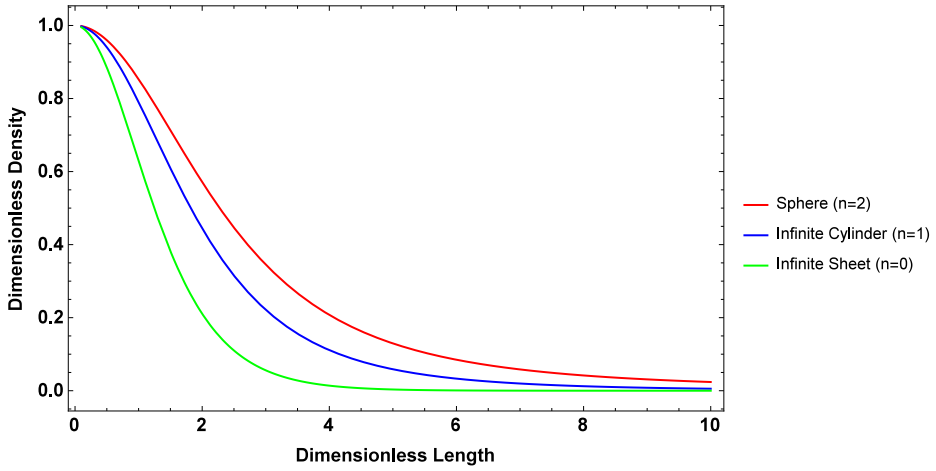


FIGURE 3.2: *The Figure shows plots of the dimensionless length against the dimensionless density for each case considered.*

of the infinite sheet decreases more sharply than the sphere and infinite cylinder, see Figure 3.2.

Unlike the density profiles of polytropic gasses which terminate at finite lengths, the isothermal clouds are not bounded [58]. As such a finite-sized, isothermal cloud can only exist if it is surrounded by a gas whose pressure at the boundary of the cloud is equal to the pressure of the cloud at that boundary. We now address the question of how stable these configurations are against gravitational collapse.

3.3.1 Gravitational Stability

We will now discuss the stability of the Bonnor-Ebert sphere. The mass of the Bonnor-Ebert sphere is given by

$$M(r) = \int_0^r 4\pi r^2 \rho(r) dr = 4\pi\rho_0\alpha^2 \int_0^x x^2 e^{-\theta(x)} dx. \tag{3.23}$$

In equation (3.23) we have chosen r to specifically mean the radius, all other quantities have their usual meaning. Using equation (3.22) and the fact that $\alpha = \frac{c}{\sqrt{4\pi G\rho_0}}$ we find that the mass equation (3.23) reduces to

$$M(x) = \frac{c^3}{\sqrt{4\pi G^3\rho_0}} x^2\theta'(x). \tag{3.24}$$

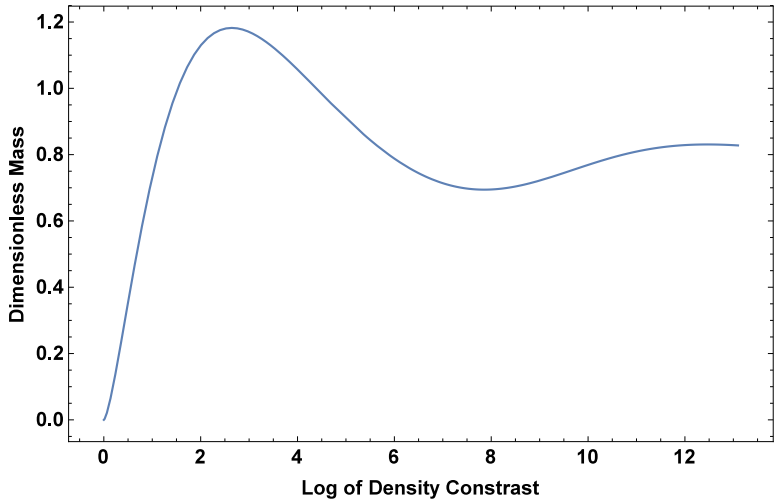


FIGURE 3.3: *In the above Figure the log of the central concentration (ratio of central to outer density) as been plot against the dimensionless mass. The fist maximum is associated with the maximum radius possible for a gravitationally stable Bonnor-Ebert sphere.*

If the mass is non-dimensionalized using the outer density together with the scaling factor in equation (3.24), the dimensionless mass is defined as

$$M(x) = \frac{c^3}{\sqrt{4\pi G^3 \rho_1}} m(x), \tag{3.25}$$

where $m(x)$ is the dimensionless mass and ρ_1 is the density at x. We find that the equation for the dimensionless mass is provided by

$$m(x) = \sqrt{\frac{\rho_1}{\rho_0}} x^2 \theta'(x). \tag{3.26}$$

It is common practice to plot this equation as a parametric plot with the natural log of the central concentration (which is defined as ρ_1/ρ_0) [7]. To see how Figure 3.3 is related to the stability of the cloud consider the following argument. If the dimensional mass is held fixed and the pressure is increased, then the dimensionless mass must increase. Figure 3.3 shows that this mass increase must result in an increase of the central concentration as long as the initial central concentration is below 14.1. But an increase in the central concentration results in an increase in the dimensionless radius since $\rho_1 = \rho_0 e^{-\theta(x_1)}$. This change in the dimensionless radius translates into a change in the dimensional radius r_1 by the scaling factor α. Since an increase in pressure will cause global compression, ρ_0 will increase resulting in a shrinking of r_1. Beyond the critical central concentration of 14.1 the reverse occurs and an increase in the pressure results in a decrease in dimensionless mass resulting in the collapse of the cloud.

The critical concentration of 14.1 can be shown (by numerically inverting the gravitational potential) to correspond to a critical dimensionless radius $x_{crit} = 6.451$. Calculating the critical radius for this shows that

$$r_{crit} = 6.541 \left(\frac{c^2}{4\pi G \rho_0} \right)^{1/2}. \tag{3.27}$$

By expressing the density in terms of the mass and radius equation (3.27) reduces to the stability criterion

$$R_{cloud} > r_{crit} = 0.41 \frac{GM}{c^2}. \tag{3.28}$$

So, Bonnor-Ebert spheres larger than r_{crit} will be unstable against gravitational collapse if subjected to any pressure perturbation. The simulation of isothermal collapse in this manner has been investigated by Foster and Chevalier as well as Aikawa et al. [19, 32].

Another approach used in the simulation of isothermal collapse is the case in which the initial velocity field is non-zero. The common choice for the profile is the free-fall speed [59]. In the work below we propose the use of a steady-state accretion velocity field in simulations where free-fall velocity profiles are used instead.

3.4 Steady-State Accretion

While the most common initial condition for the velocity field in the simulation of isothermal collapse has been the trivial one (an intially static cloud) – later investigations have included supersonic converging flows at the outer radius of the collapsing cloud [49]. Before deriving the solutions for state-state accretion we first introduce the Lambert function which is common to accretion in all three coordinate systems (Cartesian, cylindrical and spherical). All the solutions presented here are found using Mathematica's built-in function `Solve`, to find the velocity profiles.

3.4.1 Lambert's W-function

The Lambert function is also known as the product log and is defined as follows

$$\text{If } \; z = we^w, \;\; \text{then } \; w = W(z),$$

where W is the Lambert function. Due to the nature of the exponential we see that the Lambert function must in fact have two real branches: these are denoted W_0, the primary branch and W_{-1} the secondary branch cut. They exist on the domains $[-e^{-1}; \infty)$ and $[-e^{-1}, 0]$ respectively. Only these two functions are real valued.

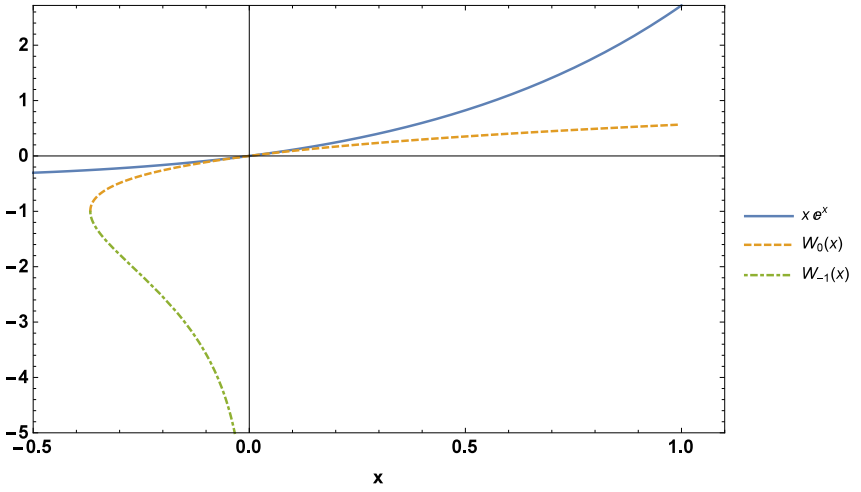


FIGURE 3.4: *The Figure shows plots of the two branches of the Lambert function together with their inverse. While the primary branch cut (dashed) is defined for all positive real numbers, the secondary branch cut is only defined on a small domain of negative real numbers.*

3.4.2 Analytical Solutions of Steady-State Accretion

The general equations for one-dimensional, isothermal steady flow may be written as

$$\frac{1}{\xi^n}\frac{d}{d\xi}\left(\xi^n \rho u\right) = 0, \tag{3.29}$$

$$u\frac{du}{d\xi} = -\frac{c^2}{\rho}\frac{d\rho}{d\xi} - \frac{d\Phi}{d\xi}. \tag{3.30}$$

Again we have chosen $n = 0, 1, 2$ to represent the case of planar, cylindrical and spherical flow respectively.

We first nondimensionalize the equations by introducing the dimensionless length, density, velocity and gravitational potential, $x, \bar{\rho}, \bar{u}$ and $\bar{\Phi}$ respectively:

$$\xi = \alpha x, \quad \rho = \rho_0 \bar{\rho}, \quad u = c\bar{u}, \quad \Phi = c^2\bar{\Phi}$$

We may use the first of equations (3.30) to eliminate the density from the second equation. This results in the equation

$$\frac{d}{dx}\left(\frac{1}{2}\bar{u}^2\right) = \frac{1}{x^n \bar{u}}\frac{d}{dx}\left(x^n \bar{u}\right) - \frac{d\Phi}{dx}.$$

This equation is easily integrable and it provides an implicit solution for the dimensionless velocity $\bar{u}$ that is of the form

$$\frac{1}{2}\bar{u}^2 - \ln\left(x^n \bar{u}\right) + \bar{\Phi} = k, \tag{3.31}$$

where k is the constant of integration. Using Mathematica it is possible to solve this equation to provide a general solution for the dimensionless velocity:

$$\bar{u}(x) = \pm i\sqrt{W_{0,-1}\left(-\frac{e^{2(\bar{\Phi}-k)}}{x^{2n}}\right)}, \tag{3.32}$$

where W_0 and W_{-1} are the primary and secondary branch cuts of the Lambert function. Equation (3.32) may be obtained in a particular coordinate system once n is chosen and the dimensionless gravitational potential $\bar{\Phi}$ has been calculated.

3.4.2.1 Calculation of Gravitational Potentials

Calculating the gravitational potentials in each of the coordinate systems is a trivial task (in the case of the one-dimensional accretion) which requires the solving of a single integral provided by

$$\Phi = -\int_V \frac{G\rho}{|\vec{\xi} - \vec{r}|} dV. \tag{3.33}$$

In this equation $|\vec{\xi} - \vec{r}|$ is the length of the vector starting from a point in the fragment to the point at which the potential is being measured, $\vec{\xi}$ being the position vector of the point where the potential is being measured and $\vec{r}$ being the position vector of a point in the fragment.

We first consider the spherical case; this corresponds to a point mass situated at the origin of the coordinate system. This reduces equation (3.33) to

$$\Phi = -\frac{GM}{r}. \tag{3.34}$$

where r is the radius. It is important to note that even if the mass has a finite radius (say R_{sph}), the potential outside the sphere would be the same up to an arbitrary constant. In dimensionless coordinates this may be expressed as

$$\bar{\Phi} = \frac{\Phi}{c^2} = -\frac{GM}{c^2 r}.$$

We wish to use M as a parameter for the steady-state accretion so if we nondimensionlize M such that $M = \frac{c^2\alpha}{G}m$ then the dimensionless gravitational potential reduces to

$$\bar{\Phi} = -\frac{m}{x}. \tag{3.35}$$

Next, we derive the gravitational potential due to an infinite cylinder. Consider a cylinder finite length (say $2a$), with a linear density of λ_{cyl}. The cylinder is orientated such that it is aligned with the z-axis of a cylindrical coordinate system and the centre of

the cylinder coincides with the origin of the coordinate system. Consider a point at a radial distance of ξ from the z-axis. Then, according to equation (3.33) the gravitational potential is defined as

$$\Phi = -\int_{-a}^{a} \frac{G\lambda_{cyl}}{\sqrt{\xi^2 + z^2}} dz. \tag{3.36}$$

Since the potential is only defined up to a scalar constant this integral evaluates to

$$\Phi = c_1 - 2G\lambda_{cyl} \tanh^{-1} \frac{a}{\sqrt{a^2 + \xi^2}},$$

here c_1 is the arbitrary constant and it is chosen so that the gravitational potential vanishes at the surface of the cylinder (i.e. at $\xi = R_{cyl}$). Enforcing this and taking the limit as $a \to \infty$ results in the gravitational potential for the infinite cylinder to be defined as

$$\Phi = -2G\lambda_{cyl} \ln\left(\frac{\xi}{R_{cyl}}\right). \tag{3.37}$$

Again we wish to nondmiensionalize this potential, this time retaining λ as a parameter. This results in a dimensionless potential provided by

$$\bar{\Phi} = 2\bar{\lambda}_{cyl} \ln x, \tag{3.38}$$

where $\bar{\lambda}_{cyl}$ is the dimensionless linear density. Finally, for the potential of the infinite sheet, consider, a thin disc (of radius R_{disc} and thickness h) in the $z = 0$ plane with the z axis passing through the disc's centre. Let the surface density of the disc be given by a constant, σ. The gravitational potential at a point ξ above the disc (and along the axis) , once again using equation (3.33), is provided by

$$\Phi = -\int_{0}^{R_{disc}} \frac{2\pi G\sigma r}{\sqrt{\xi^2 + r^2}} dr \tag{3.39}$$

Following the procedure as we did for the infinite cylinder, this time taking $R_{disc} \to \infty$, we find that the gravitational potential is given by

$$\Phi = 2\pi G\sigma(\xi - h), \tag{3.40}$$

where h is the thickness of the sheet. Choosing the scaling parameters appropriately we find the dimensionless gravitational potential may be defined as

$$\bar{\Phi} = \bar{\sigma}(x - 1), \tag{3.41}$$

where $\bar{\sigma}$ is the dimensionless surface density. We are now ready to derive the analytical solutions for steady-state accretion onto a spherical protostellar core as well as infinite cylinders and sheets. The work presented in this Section is novel.

3.4.3 Spherical Bondi Accretion

In order to find the solutions for the velocity profiles in the case of spherical accretion we begin by substituting the equation for the dimensionless potential (3.35) into the general solution for steady accretion given in equation (3.32) taking $n = 2$. This results in the following equation

$$\bar{u}(x) = \pm i\sqrt{W_{0,-1}\left(-\frac{e^{-2\left(\frac{m}{x}+k\right)}}{x^4}\right)}. \tag{3.42}$$

If we replace k with $\frac{m}{x^*}$ where x^* is a constant to be determined from the properties of the Lambert function, we note the following. The argument of the Lambert functions cannot exceed $-e^{-1}$ as seen in Figure 3.4. This may be expressed more conveniently with the introduction of another parameter γ. In this case the following may be said of the argument of the Lambert function in equation (3.42):

$$-\frac{e^{-2\left(\frac{m}{x}+\frac{m}{x^*}\right)}}{x^4} = -\gamma^4 e^{-1}, \tag{3.43}$$

where γ is the introduced parameter running from zero to one; outside of this range the solution will not be defined on the real plane. The forth power on γ has been chosen for convenience as will be seen in the solution. Since bounds for gamma have already been specified we need to determine x^* so that equation (3.43) is satisfied for x in general. To do this equation (3.43) is solved in terms of x^* using Mathematica. The resulting equation is indeed a function of x. The value of x is chosen so as to maximise the value of x^*. This is to say that the value of x^* is the largest possible value for which equation (3.43) is satisfied, which corresponds to $x = \frac{m}{2}$. The resulting value for x^* is therefore

$$x^* = \frac{2m}{4\ln\left(\frac{2}{\gamma m}\right) - 3}. \tag{3.44}$$

The corresponding dimensionless velocity profile is provided by

$$\bar{u}(x) = \pm i\sqrt{W_{\{0,-1\}}\left[-\left(\frac{\gamma m}{2x}\right)^4 e^{3-\frac{2m}{x}}\right]}. \tag{3.45}$$

In Figure 3.5 we see that for $0 < \gamma < 1$ flow is either subsonic in the case of the primary branch cut W_0 of supersonic in the case of the secondary branch cut. The solutions tend to zero and infinity respectively as x tends to zero. We see that the flow is transonic only when $\gamma = 1$. In this instance inflowing gas is either slowed down to subsonic speeds or sped up to supersonic speeds at the sonic point $\xi = m/2$. There are no physically relevant solutions for the case when $\gamma > 1$. The negative roots of the solution for the

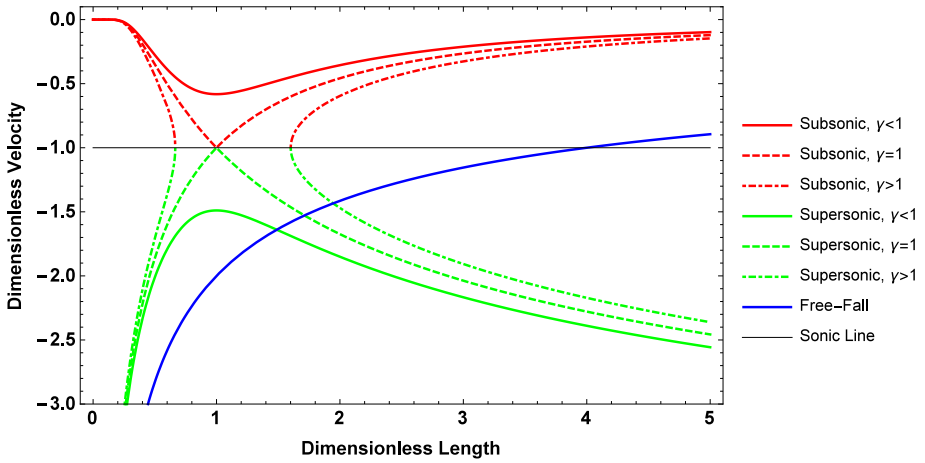


FIGURE 3.5: *The above Figure shows the two functions W_0 (red) and W_{-1} (green) for parameter values $\gamma = 0.9, 1.0, 1.1$ (corresponding to solid, dashed and dot-dashed lines) and $m = 2$. The solutions are exactly those of classical Bondi accretion. For the case of $\gamma = 1$ the solutions intersect $x = m/2$. The solid line in blue represents the free-fall velocity profile.*

velocity were chosen to signify gravitational attraction causing the gas to flow inward. The free-fall solution is found by solving the set of equations (3.30) with the pressure term dropped. In dimensionless coordinates this is provided by

$$\bar{u}\frac{d\bar{u}}{dx} = -\frac{m}{x^2}, \quad \bar{u}_{ff} = -\sqrt{\frac{2m}{x_m} - \frac{2m}{x}}. \tag{3.46}$$

We have chosen $\frac{2m}{x_m}$ as the arbitrary constant; in this case x_m would be equivalent to the core radius. This may be seen by noting that $\bar{u}_{ff}$ becomes imaginary as x gets smaller than x_m. The free-fall velocity profile appears to run parallel to the primary branch when x is large; it tends to the secondary branch cut as x tends to 0. Also of interest is the density profile shown in Figure 3.6. The density profile related to the case of subsonic flow increases to infinity much more rapidly than the supersonic and free-fall cases and while the density profile for the free-fall case matches with the supersonic flow case it only does so in the limit as $x \to 0$. Indeed a series expansion of the solutions for the density profiles makes this clearer. Using Mathematica we can show that the velocity profile in the subsonic case has the following limits:

$$\bar{\rho}_{sup} \sim x^{-3/2}, \quad \text{as} \quad x \to 0$$
$$\bar{\rho}_{sup} \sim x^{-2}, \quad \text{as} \quad x \to 0,$$

where $\bar{\rho}_{sup}$ is the density profile corresponding to supersonic flow. This result is in agreement with the work of Shu [21]. Next we derive the analytical solutions for steady-state accretion onto a cylindrical fragment.

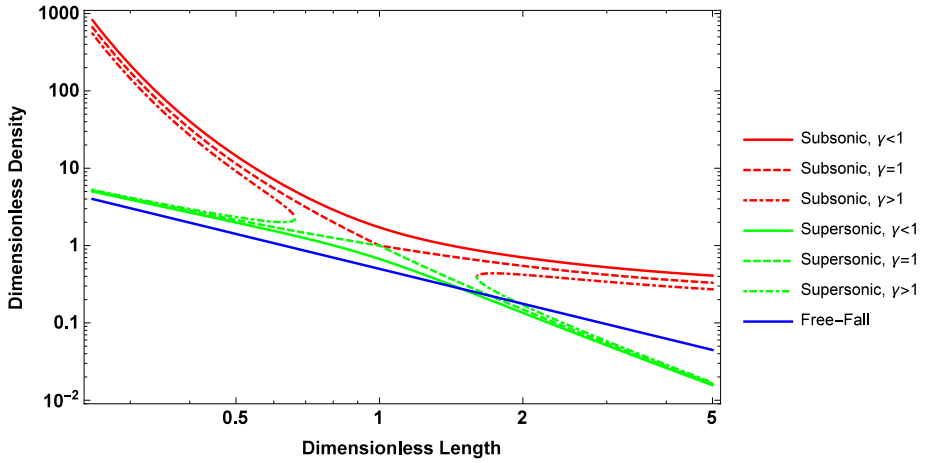


FIGURE 3.6: *The Figure shows a log scaled plot of the dimensionless length versus the dimensionless density. The density corresponding to subsonic flow is in red while the supersonic density profiles appear in green. Again, this has been done for parameter values of* $\gamma = 0.9, 1.0, 1.1$ *(solid, dashed, dotdashed) and* $m = 2$*. The solid blue line represents the density profile associated with free-fall.*

3.4.4 Cylindrical Accretion

The gravitational potential for the infinite cylinder, given in equation (3.38), may be substituted in to the general solution for steady-state accretion. This results in the following equation

$$\bar{u} = -i\sqrt{W_{\{0,-1\}}\left[-\left(\frac{x^{*\lambda}}{x^{\bar{\lambda}_{cyl}-1}}\right)^2\right]}. \tag{3.47}$$

Again, x^* is to be defined in the same manner as we did for the spherical case. The structure of the solutions show that there are in fact six possible flow types depending on the value of the dimensionless surface density $\bar{\lambda}_{cyl}$: three types for each of the two branch cuts of the Lambert function. The special case is when $\bar{\lambda}_{cyl} = 1$ then the flow is completely independent of x and is therefore constant everywhere. Before discussing the flow types in detail we derive the value of x^*.

Recall that the argument of the Lambert function cannot be smaller than $-e^{-1}$. This leads us to

$$-\left(\frac{x^{*\lambda}}{x^{\bar{\lambda}_{cyl}-1}}\right)^2 = -\gamma^2 e^{-1}.$$

Again the form of γ is chosen for convenience. We find that

$$x^* = \max\left[e^{\frac{1}{2\lambda}}\left(\gamma^2 x^{2-2\lambda}\right)^{-\frac{1}{2\lambda}}\right].$$

This depends on the sign of $\bar{\lambda}_{cyl} - 1$ where the value of x^* may be determined as follows:

$$x^* = \begin{cases} e^{\frac{1}{2\bar{\lambda}_{cyl}}} \left(\gamma^2 x^{2-2\bar{\lambda}_{cyl}}\right)^{-\frac{1}{2\bar{\lambda}_{cyl}}} \Big|_{x=1} & \text{if } \bar{\lambda}_{cyl} < 1 \\ e^{\frac{1}{2\bar{\lambda}_{cyl}}} \left(\gamma^2 x^{2-2\bar{\lambda}_{cyl}}\right)^{-\frac{1}{2\bar{\lambda}_{cyl}}} \Big|_{x=\max(x)} & \text{if } \bar{\lambda}_{cyl} > 1 \\ \sqrt{\frac{e}{\gamma^2}} & \text{if } \bar{\lambda}_{cyl} = 1. \end{cases} \tag{3.48}$$

If we let $\max(x) = x_m$ correspond to the dimensionless radius at the outer boundary of the accreting cloud, then the obtained values for x^* correspond to the following solutions for the velocity profiles:

$$\bar{u} = i\sqrt{W_{\{0,-1\}}\left(-\frac{\gamma^2}{e x^{2-2\bar{\lambda}_{cyl}}}\right)} \quad \text{if} \quad \bar{\lambda}_{cyl} < 1 \tag{3.49}$$

$$\bar{u} = i\sqrt{W_{\{0,-1\}}\left[-\left(\frac{\gamma^2}{e}\right)\left(\frac{x}{x_m}\right)^{2\bar{\lambda}_{cyl}-2}\right]} \quad \text{if} \quad \bar{\lambda}_{cyl} > 1 \tag{3.50}$$

$$\bar{u} = i\sqrt{W_{\{0,-1\}}\left(-\frac{\gamma^2}{e}\right)} \quad \text{if} \quad \bar{\lambda}_{cyl} = 1. \tag{3.51}$$

The free-fall velocity may be found by solving the equation provided by

$$\bar{u}\frac{d\bar{u}}{dx} = -\frac{\bar{\lambda}_{cyl}}{x}.$$

This is easily integrated to give

$$\bar{u}_{ff} = -\sqrt{2\bar{\lambda}_{cyl}\ln\left(\frac{x_m}{x}\right)}. \tag{3.52}$$

For the case of $\bar{\lambda}_{cyl} < 1$ the subsonic velocity profile increases in magnitude as x tends to one while the supersonic flow decreases in magnitude toward the infinite cylinder, see Figure 3.7 below. It is worth noting that the free-fall flow bears no resemblance to the subsonic or supersonic flows. This is likely due to the fact that $\bar{\lambda}_{cyl} < 1$ corresponds to the case where a self-gravitating infinite cylinder is stable against gravitational collapse. When $\bar{\lambda}_{cyl} > 1$ the flow structures are reversed with the subsonic flow decreasing in magnitude and the supersonic flow increasing in magnitude toward the cylinder. The free-fall velocity profile bears slight similarity to the supersonic flow toward the cylinder but does not resemble the subsonic flow anywhere, see Figure 3.8. Unlike spherically symmetric accretion there are no physically relevant, transonic solutions for both cases of cylindrical accretion. We end our discussion of steady-state accretion by deriving the solutions to the velocity profiles for steady-state accretion onto an infinite sheet.

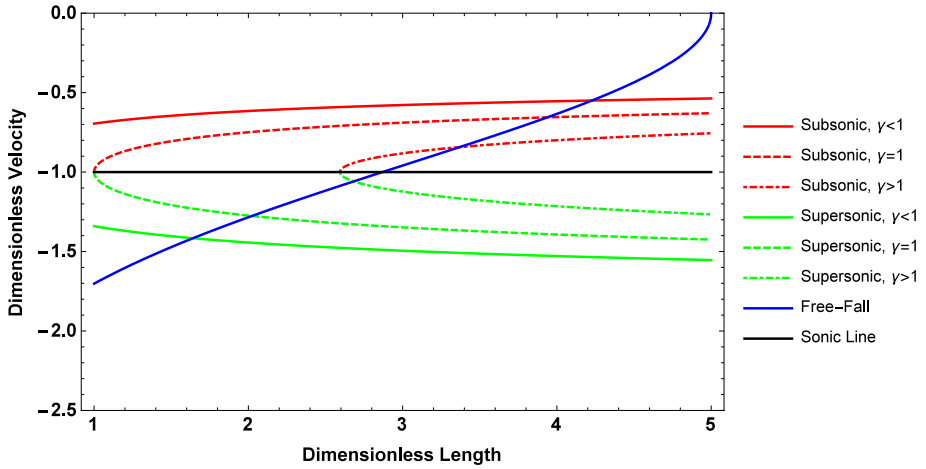


FIGURE 3.7: *The Figure shows the plot of the velocity profiles for cylindrical accretion in the case where* $\bar{\lambda}_{cyl} < 1$. *The red curves represent subsonic flow while curves in green represent supersonic flow. The single blue line represents the free-fall line. In these plots* $\bar{\lambda}_{cyl} = 0.9, x_m = 5$.

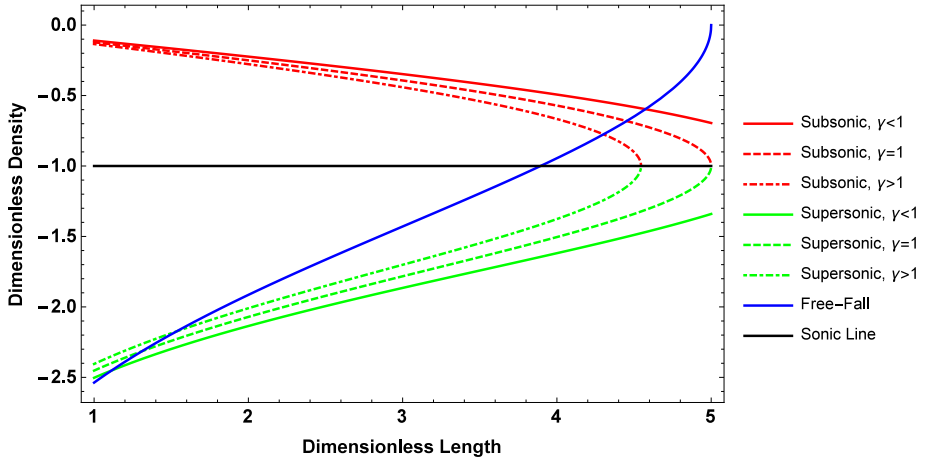


FIGURE 3.8: *The Figure shows the plot of the velocity profiles for cylindrical accretion in the case where* $\bar{\lambda}_{cyl} > 1$. *Again the red curves represent subsonic flow while curves in green represent supersonic flow. The single blue line represents the free-fall line. In these plots* $\bar{\lambda}_{cyl} = 2, x_m = 5$.

3.4.5 Planar Accretion

Once more, we use the general solution for steady-state accretion provided in equation (3.32) together with the gravitational potential for the infinite sheet given in equation (3.39) to solve for the velocity profile. This results in the velocity profile being given by

$$\bar{u} = i\sqrt{W_{\{0,-1\}}(-e^{2\sigma(x-x^*)})}. \tag{3.53}$$

The condition on x^* is similar to the one derived for the infinite cylinder in that it must be defined as the maximum value of x, again we will refer to this as x_m. This may be taken as the thickness of the accreting layer or any other length scale (in dimensionless

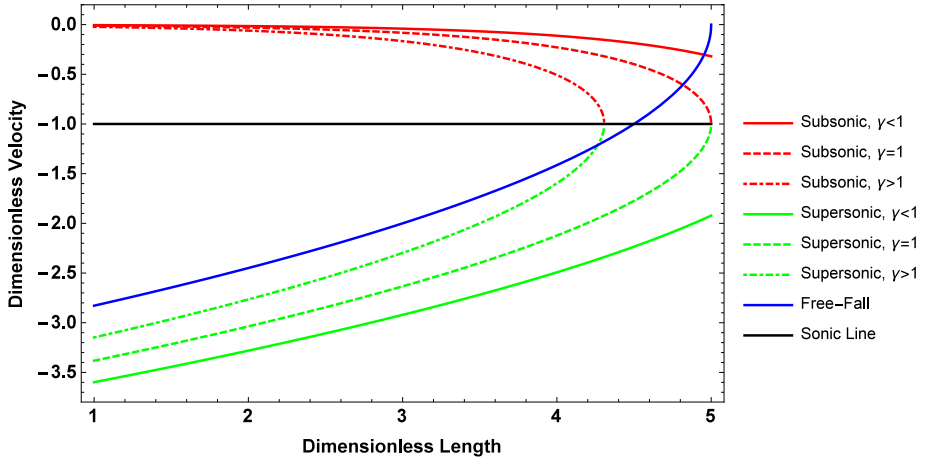


FIGURE 3.9: *The Figure shows the plot of the velocity profiles for steady planar accretion. The red curves represent subsonic flow while curves in green represent supersonic flow. The single blue line represents the free-fall line. In these plots* $\bar{\sigma} = 1, x_m = 5.$ *and the solid, dashed and dot-dashed, red and green curves represent* $\gamma = 0.25, 1, 4$ *respectively.*

units). In this case the velocity is provided by

$$\bar{u} = i\sqrt{W_{\{0,-1\}}\left(-\gamma e^{2\sigma(x-x_m)-1}\right)}. \tag{3.54}$$

The free-fall velocity profile is trivial to solve for and is given simply by

$$\bar{u}\frac{d\bar{u}}{dx} = -\sigma, \tag{3.55}$$

which means that

$$\bar{u} = -\sqrt{2\sigma(x_m - x)}. \tag{3.56}$$

We have followed the same argument as we did for the case of cylindrical accretion.

The velocity profiles of planar accretion are similar to that of cylindrical accretion in that there are no transonic solutions such as what was found for spherical accretion. The supersonic flow increases rapidly toward the sheet surface. The free-fall velocity profile agrees very well with the supersonic profile only in the critical case of $\gamma = 1$. The exception to this agreement occurs as $x \to x_m$, see Figure 3.9. In the cases of planar and cylindrical steady-accretion if x^m is greater than the domain of x there is no critical flow when $\gamma > 1$.

3.5 Concluding Remarks

In this Chapter we have reviewed and discussed Jeans criterion and considered the gravitational stability of Bonnor-Ebert spheres. This is necessary for the initialization

of the numerical simulations to be performed – isothermal clouds must be initialized with states that are unstable against collapse. The degree of this instability will be shown to determine the finer detail in the collapse; core bounce is one such detail to be discussed in the next two Chapters.

We have found new, analytical solutions for the velocity profiles for isothermal gas undergoing steady accretion onto spherical cores as well as infinite cylinders and infinite sheets. These solutions were found to be in terms of the primary and secondary branch cuts of the Lambert function. We have structured the solution in dimensionless quantities and used the mass, linear density and surface density as well as γ as parameters of the solutions in such a way that the solutions are physically relevant only when $0 \leq \gamma \leq 1$ with $\gamma = 1$ corresponding to a limiting case.

The steady-state solutions are relevant for current research in that they offer a new and alternative initial condition for exploring isothermal collapse. Lastly, and most importantly the steady-state accretion solutions could be used to infer protostellar core masses and sizes if velocity or density profile data could be matched up to a steady-state accretion velocity or velocity profile. In the next Chapter we will compare the density profiles (post free-fall time) obtained from numerical simulations with the analytical solutions derived here.

Chapter 4

Numerical Simulations of Isothermal Collapse: TVD-MUSCL Scheme

In this Chapter we perform numerical simulations of the gravitational collapse of spherically symmetric, isothermal clouds with two different types of initial conditions: clouds with initially unform densities and clouds with perturbed Bonnor-Ebert density profiles. In the case of the former, initial condition clouds have radii close to the Jeans radius. The clouds simulated are characterised by the ratio of free-fall to sound travel times (t_{ff}/t_s). The focus of the simulation is on the core bounce, which occurs close to the free-fall time, in relation to t_{ff}/t_s. The bounce of the core results in the formation of a shock wave which propagates outward as the collapse continues. For the collapse of perturbed Bonnor-Ebert spheres we have used the central concentration (ρ_c/ρ_0) to characterise the clouds. A weaker bounce is detected in the collapse of these clouds with no shock resulting from the outward pressure wave. The hydrodynamical equations are solved using the MUSCL scheme of van Leer [43] with a Roe flux on a uniform grid. This simulation is performed with the assumption of a fixed volume and the grid is setup so that the global mass is conserved exactly.

4.1 Introduction

The numerical simulation of isothermal collapse forms a fundamental part of our understanding of star formation. Numerical simulation is particularly important in that it acts as a link between observation and theory and provides potential insight into what may not be possibly observed. The numerical simulation of isothermal collapse has been investigated by several authors, see [6, 19, 21, 23]. In general, the solutions have been in agreement – collapse proceeds in a very non-homologous fashion, clouds with an initially uniform density collapse from the outside inward while clouds with an initially high central concentration collapse from the inside with a sound wave propagating outward. The hydrodynamic equations of isothermal collapse are of computational interest due to their structure. While the numerical schemes used to solve the hydrodynamic equations must be capable of handling the development of shock in the cloud they must also be robust enough to handle the gravitational source term which becomes increasingly dominant as the collapse proceeds.

Historically, the hydrodynamic equations have been solved using the Lagrangian formulation in which fluid particles are followed during the course of the collapse [6, 23, 48]. On the other hand authors such as Boss [10, 33] have used a moving grid which acts as a hybrid between the Lagrangian and Eulerian formulations. The solutions of Larson have become the most prominent in terms of numerical simulation with the main feature of his work being the resemblance his solution for the density profiles has that of the Bonnor-Ebert spheres, see Figure 4.1 below. The numerical solutions from the numerical simulation may be regarded as a collection of Bonnor-Ebert spheres at a fixed dimensional radius but with increasing central density, see Figure 4.2 below. The numerical and self-similar solutions of Larson[6] and equally Penston [60] led to deeper inverstigation of similarity solutions. Shu considered approaching the problem of isothermal collapse by using the singular isothermal sphere as an initial condition [21] and solving the problem using a similarity transform. While Shu was able to find analytical solutions in some cases (referred to in Chapter 1) the general self-similar equations (1.5) have no analytical closed form solution. Shu's solutions have also remained a prominent source for understanding self-similar collapse and his work has led to much advancement in the field, see [22, 27–29, 61].

A particularly interesting feature of isothermal collapse that is not frequently mentioned in numerical simulations of this problem is that of core bounce. Hayashi [24] noted that as the collapse proceeds the density gradient (and hence the pressure gradients) around the central region can become large enough to exceed that gravitational force resulting in a bounce of the core which sends a pressure wave propagating outward – the direction of the velocity around the centre is radially outward for a brief moment.

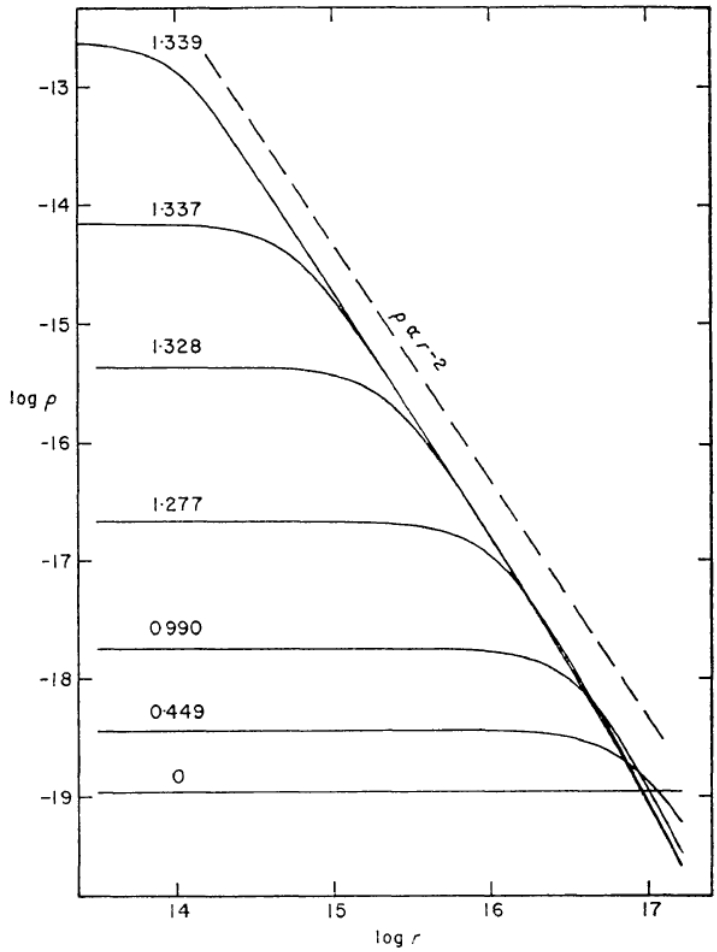


FIGURE 4.1: *A log-log plot of the density for a spherically symmetric cloud at different times during the collapse performed by Larson [6]. On the horizontal axis is the log of the dimensional radius and the vertical axis shows the log of the dimensional density. Simulations performed here were for an initial uniform cloud with a mass of* $1M_{\odot}$ [6].

Hayashi noted that this pressure wave later develops into a shock wave that is capable of ionizing the surrounding gas while the rest of the inner region of the cloud continues to collapse. It is surprising that Larson only mentions the need for shock fitting in the later stages of the collapse when the equation of radiative transfer becomes important in the simulation. Shocks and outflows in the collapse have been discussed mainly in the context of similarity solutions [27–29].

Since the radiative properties are not accounted for in our current simulations it is important that the computation be terminated before the central density exceeds $\sim 10^{-13} gcm^{-3}$ at which point the core region could be supported against collapse by radiation and adiabatic pressure. Most of the early numerical simulations, see [6, 18, 23], employ the Lagrangian approach meaning that fluid particles are followed throughout the collapse. This becomes computationally expensive because as the cloud collapses more and more fluid particles approach the centre. This results in an increase in the

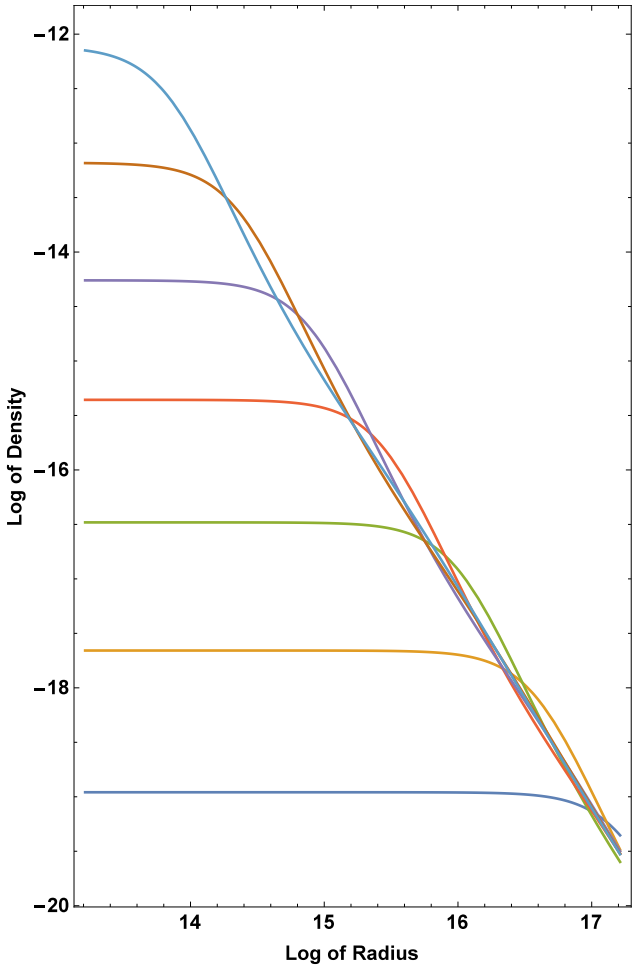


FIGURE 4.2: *A log-log plot of the density for Bonnor-Ebert spheres with increasing central densities but the same dimensional radius . On the horizontal axis is the log of the dimensional radius and the vertical axis shows the log of the dimensional density. The density profiles are very similar to those found by Larson, shown in Figure 4.1*

number of particles at the centre of the cloud. Computationally, this will inevitably cause numerical instability with regards to the rest of the cloud. A way around this is to introduce a threshold for the central density. Once the central density exceeds this point the central region is treated differently from the rest of the cloud. One such example is the sink particle method [47]. The Eulerian equivalent of this is the sink particle method introduced by Boss and Black who employed a moving Eulerian grid technique developed by Black and Bodenheimer [10]. Initializing their computation with a singular isothermal sphere similar to that of Shu [21], they then introduced a sink cell with a non-zero mass at the centre of the cloud which was numerically separated from the rest of the cloud but maintained the gravitational coupling between core and envelope. The sink cell is introduced once the central density reaches some threshold. While this approach has proven useful for many situations Whitworth et al. [31] have argued that it is biased against the formation of binary stars.

The need to avoid the collapsing cloud exceeding isothermal temperatures is compounded by another issue that is more central to numerical simulation – artificial fragmentation. Truelove et al. [2] introduced a criterion to avoid artificial fragmentation related to the cell size and the Jeans number. They showed that one must have

$$\delta r / \sqrt{\frac{\pi c_s^2}{G\rho}} < 0.25, \tag{4.1}$$

for this to occur. Given that the central density should not exceed $\sim 10^{-13} gcm^{-3}$ we find that the we may have $\sim 10^3$ grid points that are equidistant. Truelove et al. [2] also highlighted that fact that artificial viscosity methods violate their Jeans condition if used to halt the 'collapse process'.

The numerical simulation of spherically symmetric, isothermal collapse still remains insightful with regards to application [32] as well as the development of better numerical methods and alternative means of dealing with core formation. In this Chapter we perform numerical simulations of isothermal collapse using Roe's flux formula with the MUSCL-TVD of van Leer [43] for the hyperbolic part. The gravitational source term is incorporated by updating the gravitational force rather than the potential so as to avoid performing spatial integration. The geometric source term in approximated in such a way as to avoid numerical instabilities forming at the centre. The simulation is kept in the isothermal regime by using the Truelove criterion as a stopping condition. The solutions, when the simulation is terminated are compared to the density profiles for steady-state accretion which allows for the mass and radius of the core to be inferred. The difference between the collapse of an initially uniform cloud and a Bonnor-Ebert sphere is also investigated.

4.2 Numerical Simulation

4.2.1 The Model

While the process of star formation involves an increase in density by more than 20 orders of magnitude, the early stages of collapse (the formation of the protostellar core) are assumed to occur isothermally. That is to say that from the first instance of collapse (when density $\sim 10^{-19}$) to roughly 10^{-13} the gas remains at the same temperature; a temperature of $10K$ is commonly used [8]. This assumption is justified due to the fact that at these densities the gas is optically thin and any heating caused by gravitational collapse is quickly radiated away – this occurs over a time scale much shorter than the collapse time scale which is around t_{ff}. Thus an isothermal equation of state may be

used ($P = c^2\rho$, where c is a constant) and the equations governing the collapse are provided by

$$\frac{\partial \rho}{\partial t} + \frac{1}{r^2}\frac{\partial \left(r^2 \rho u\right)}{\partial r} = 0, \tag{4.2}$$

$$\frac{\partial \rho u}{\partial t} + \frac{1}{r^2}\frac{\partial}{\partial r}\left[r^2\left(\rho u^2 + \rho c^2\right)\right] = \frac{2\rho c^2}{r} - \rho\frac{\partial \Phi}{\partial r}, \tag{4.3}$$

$$\frac{1}{r^2}\frac{d}{dr}\left(r^2\frac{d\Phi}{dr}\right) = 4\pi G\rho. \tag{4.4}$$

Here t and r are the time and radius, ρ, u and Φ are the density, radial velocity and gravitational potential respectively. G and c are the gravitational constant and the sound speed respectively. Because of the magnitude of the numbers involved in the simulation – $\rho \sim 10^{-19}, r \sim 10^{17}$ – it is useful to nondimensionalize the system of equations. It also makes the comparison to the results found for steady-state accretion easy to perform. Foster and Chevalier [19] used the following scaling parameters:

$$\begin{aligned} \rho &= \rho_0\bar{\rho}, \\ u &= c\bar{u}, \\ t &= \frac{\bar{t}}{\sqrt{4\pi G\rho_0}}, \\ r &= \frac{c\bar{r}}{\sqrt{4\pi G\rho_0}}, \end{aligned}$$

where all the barred quantities are dimensionless and the gravitational potential is nondimensionlized as $\Phi = (4\pi G\rho_0)^2\bar{\Phi}$. Then the system of dimensionless equations to be solved numerically is given by

$$\frac{\partial \rho}{\partial t} + \frac{1}{r^2}\frac{\partial \left(r^2 \rho u\right)}{\partial r} = 0, \tag{4.5}$$

$$\frac{\partial \rho u}{\partial t} + \frac{1}{r^2}\frac{\partial}{\partial r}\left[r^2\left(\rho u^2 + \rho\right)\right] = \frac{2\rho}{r} - \rho\frac{\partial \Phi}{\partial r}, \tag{4.6}$$

$$\frac{\partial^2 \Phi}{\partial t \partial r} = -\rho u. \tag{4.7}$$

The initial and boundary conditions are provided by

$$\begin{aligned} &\rho(r,0) = 1 \text{ or } e^{-\psi(r)}, \ , \qquad u(r,0) = 0, \\ &\left.\frac{\partial \rho}{\partial r}\right|_{r=0} = \left.\frac{\partial \rho}{\partial r}\right|_{r=R} = 0, \quad u(0,t) = u(R,t) = 0. \end{aligned}$$

The initial condition for the density profile is model dependent and the function $\psi(r)$ is the solution to the isothermal Lane-Emden equation (see equation (3.22) in Chapter 2) and R is the dimensionless radius of the cloud. We have dropped the bars on all the quantities for the sake of simplicity. The boundary conditions are chosen so that the velocity vanishes at $r = 0$ as well as at the cloud radius. Neumann conditions on

the density are implemented at both the centre and outer boundary (which coincides with the cloud radius). This set of boundary conditions ensures that the gravitational force vanishes at the centre as it should since no mass production occurs in the system problem considered in this thesis. The initial conditions are grouped up into two sections: initially uniform clouds and perturbed Bonnor-Ebert spheres. The clouds in all cases are assumed to be static at the beginning of the simulation.

4.2.2 Derivation of Numerical Scheme

In Chapter 2 we gave a detailed description of the techniques involved in solving hyperbolic conservation laws. Given that the discussion was more focused on the structure of the numerical flux we did not describe the input of the numerical flux. In this Section we will first derive Roe's flux formula [62] and introduce the MUSCL scheme which will be used to solve the hyperbolic part of the hydrodynamic equations. Recall from Chapter 2 that we may approximate the flux at the $(i-1/2)^{th}$ interface by

$$\tilde{\mathbf{F}}_{i-1/2} = \mathbf{F}(\mathbf{Q}^n_{i-1}) + \mathcal{A}^- \Delta \mathbf{Q}^n_{i-1/2} \tag{4.8}$$

or similarly

$$\tilde{\mathbf{F}}_{i-1/2} = \mathbf{F}(\mathbf{Q}^n_{i}) - \mathcal{A}^+ \Delta \mathbf{Q}^n_{i-1/2}, \tag{4.9}$$

where $\mathbf{Q}$ is the state vector. Roe took the average of these two approximations for the flux formula [62]: this may be expressed in its usual form provided by

$$\mathbf{F}^{Roe}_{i-1/2} = \frac{1}{2}\left[\mathbf{F}(\mathbf{Q}^l_{i-1/2}) + \mathbf{F}(\mathbf{Q}^r_{i-1/2}) - \left|A\left(\mathbf{Q}^l_{i-1/2}, \mathbf{Q}^r_{i-1/2}\right)\right| \cdot \left(\mathbf{Q}^r_{i-1/2} - \mathbf{Q}^l_{i-1/2}\right)\right]. \tag{4.10}$$

Recall also that

$$\mathcal{A}^- = |A| - A, \quad \mathcal{A}^+ = |A| - A,$$

and A is the Jacobian of the flux. The Roe flux has the advantage of solving the Riemann problem exactly when the equation is linear.

It is to be noted that in equation (4.10) the quantities $\mathbf{Q}^l_{i-1/2}$ and $\mathbf{Q}^r_{i-1/2}$ are approximations of the left and right states of the system centred on the $(i+1/2)^{th}$ interface. Godunov's method is focused on using a piecewise constant approximation for the left and right state but van Leer [43] and later Colella and Woodward [39] derived a linear and quadratic reconstruction respectively. For the simulations performed here the MUSCL scheme of van Leer is used together with a van Albada limiter which has proven to be a very good combination, particularly for astrophysical gas dynamics [63] . In this

scheme the left and right states of the $(i+1/2)^{th}$ interface is provided by

$$\mathbf{Q}^{l}_{i-1/2} = \mathbf{Q}_{i-1} + 0.5\phi(\eta_{i-1})\left(\mathbf{Q}_i - \mathbf{Q}_{i-1}\right) \tag{4.11}$$

and

$$\mathbf{Q}^{r}_{i-1/2} = \mathbf{Q}_{i} - 0.5\phi(\eta_{i})\left(\mathbf{Q}_{i+1} - \mathbf{Q}_{i}\right) \tag{4.12}$$

respectively. The quantity $\phi(\eta)$ is the van Albada flux limiter [63] given by

$$\phi(\eta) = \frac{\eta^2 + \eta}{\eta^2 + 1}, \tag{4.13}$$

where η is a ratio of the gradients of the state vector for the adjacent cell:

$$\eta = \frac{\mathbf{Q}_i - \mathbf{Q}_{i-1}}{\mathbf{Q}_{i+1} - \mathbf{Q}_i}.$$

Since we have already described the finite volume structure in Chapter 2 we will only state the discrete system to be solved. In discrete form the hydrodynamic equations for isothermal collapse are given by

$$\begin{aligned}
\mathbf{Q}^{n+1}_i = \mathbf{Q}^{n}_i \quad &- \quad 3\Delta t \frac{r^2_{i+1/2}\tilde{\mathbf{F}}(\mathbf{Q}^{l}_{i+1/2}, \mathbf{Q}^{r}_{i+1/2}) - r^2_{i-1/2}\tilde{\mathbf{F}}(\mathbf{Q}^{l}_{i-1/2}, \mathbf{Q}^{r}_{i-1/2})}{r^3_{i+1/2} - r^3_{i-1/2}} \\
&+ \quad 3\Delta t \mathbf{S}_g(\mathbf{Q}^{n}_i) \frac{r^2_{i+1/2} - r^2_{i-1/2}}{r^3_{i+1/2} r^3_{i-1/2}} \\
&+ \quad 3\Delta t \Delta r \frac{r^2_{i+1/2}\mathbf{S}(\mathbf{Q}^{n}_{i+1/2}) + r^2_{i-1/2}\mathbf{S}(\mathbf{Q}^{n}_{i-1/2})}{2(r^3_{i+1/2} - r^3_{i-1/2})}.
\end{aligned} \tag{4.14}$$

The discretized equation for the gravitational force is given by

$$\left(\frac{\partial \Phi}{\partial r}\right)^{n+1}_{i-1/2} = \left(\frac{\partial \Phi}{\partial r}\right)^{n}_{i-1/2} - \rho u^{n}_{i+1/2}. \tag{4.15}$$

The state vector, geometric source and gravitational source terms are defined in the scheme as follows

$$\mathbf{Q} = \begin{pmatrix} \rho \\ \rho u \end{pmatrix}, \quad \mathbf{S}_g = \begin{pmatrix} 0 \\ \rho \end{pmatrix}, \quad \mathbf{S} = \begin{pmatrix} 0 \\ -\rho \frac{\partial \Phi}{\partial r} \end{pmatrix}.$$

The interface values that are not superscripted are calculated by taking the average of the left and right states around that interface.

Model	$R_{cloud}(10^{17}cm)$	$\rho_c(10^{-19}gcm^{-3})$	$\bar{\rho}(10^{-19}gcm^{-3})$	t_{ff}/t_s	$\rho_c/\bar{\rho}_m$
Uni 1	1.64	0.969	0.969	0.74	1
Uni 2	1.17	3.06	3.06	0.61	1
Uni 3	0.77	10.3	10.3	0.50	1
BE 1	1.59	5.89	1.17	0.72	5.02
BE 2	1.57	7.06	1.24	0.712	5.69
BE 3	1.52	11.52	1.35	0.701	8.51

TABLE 4.1: *In the above Table we provide initial data for the collapse of each presented model. The dimensional parameters are the clouds radius, the central density, and the mean density. The dimensionless quantities are the ratio of free-fall to sound travel time.*

4.2.3 Initializing Parameters for Numerical Simulation

Table 4.1 below presents the parameters of the six models for the isothermal clouds to be simulated. For the simulations presented here we have used a unform grid with 1500 grid cells.

4.3 Results and Discussion

Below, the results of the numerical simulations performed for the six cases under consideration are presented. Figure 4.3 and Figure 4.4 show the density profiles for each of the six simulated models at various times. The collapse of the uniform initially clouds occurs quicker than that of the perturbed Bonnor-Ebert cloud because the latter cloud is closer to its equilibrium than the former. While the collapse proceeds in a very similar way for both cloud types the bounce is more noticeable for the initially uniform spheres, see Figure 4.5 and Figure 4.6. Figure 4.7 illustrates that the bounce in the case of the Bonnor-Ebert spheres does not decrease the density but rather the rate of central density increase is slowed down temporarily. The results of the last iteration (when the Truelove condition is met) are shown to be in good agreement with the analytical solution found for steady-state accretion. The agreement of the two solutions deviates toward the edge and toward the centre of the cloud. This is due to the fact that the domain of the analytical solution goes from zero to infinity. The results from Table 4.2 show that the core masses of the Bonnor-Ebert spheres are larger than those found for the initially unform spheres. This result is expected given that the Bonnor-Ebert spheres had an initial central concentration. The free-fall density profiles agree only marginally toward the center.

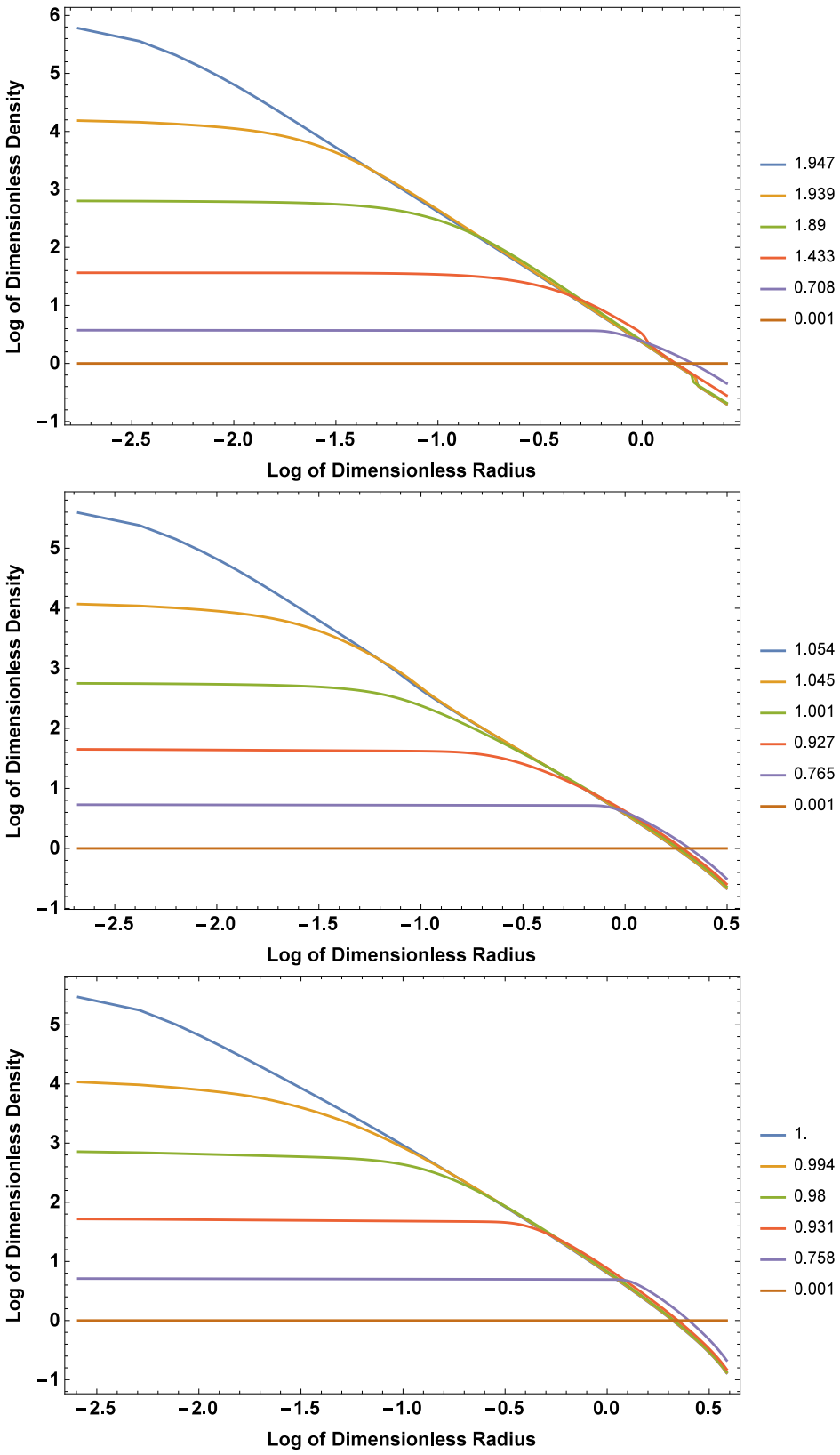


FIGURE 4.3: *The Figure shows log-log plots of the density profile for initially uniform spheres at various times (in units of t_{ff}), shown in the legend.*

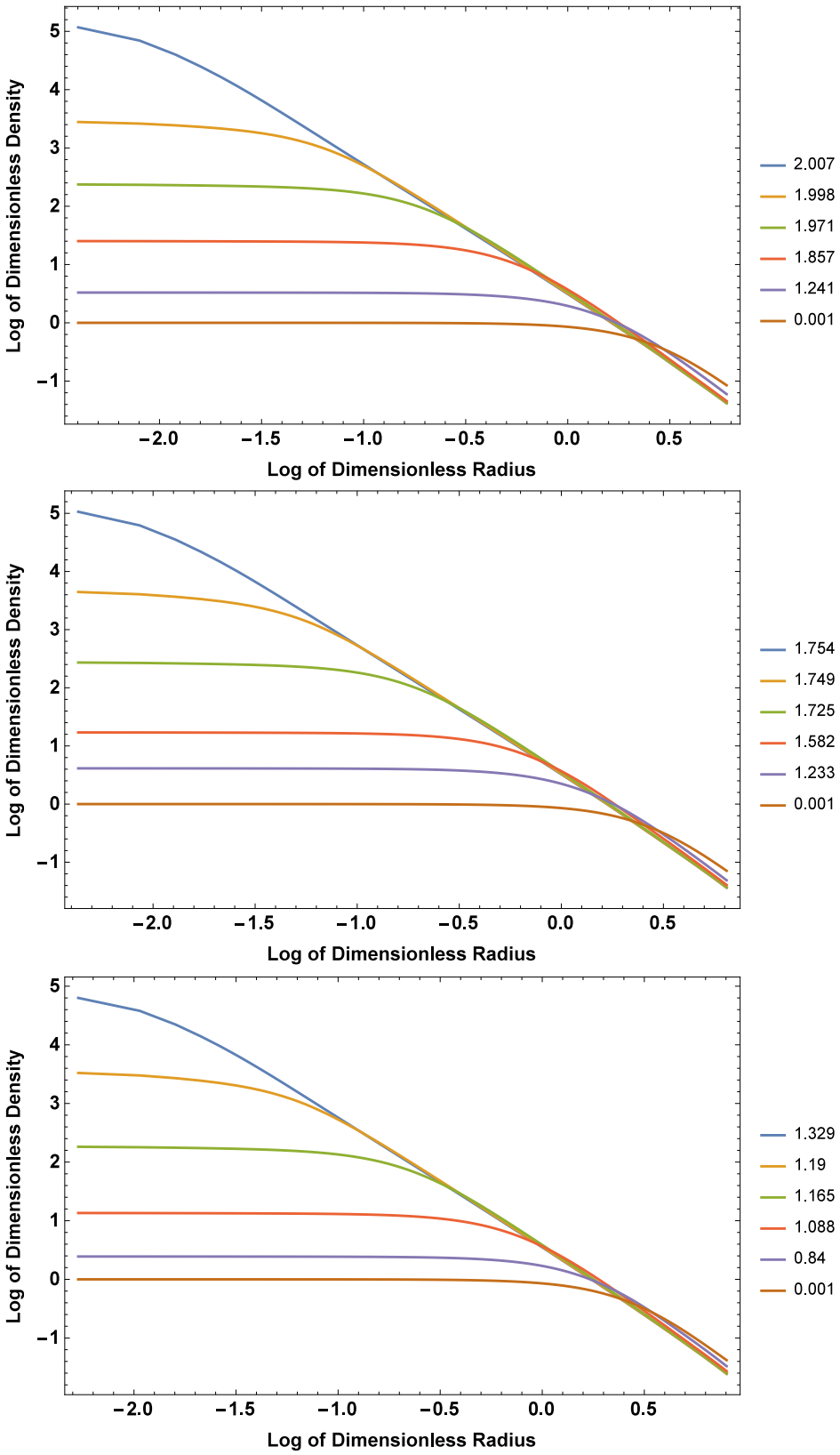


FIGURE 4.4: *The Figure shows plots of the density profile for perturbed Bonnor-Ebert sphere at various times (in units of t_{ff}), shown in the legend.*

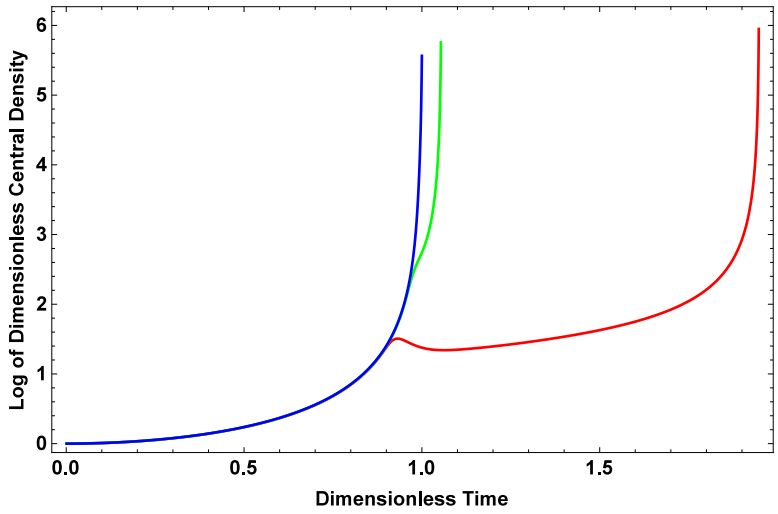


FIGURE 4.5: *The Figure illustrates the increase in central density for models* Uni 1 *(red),* Uni 2 *(blue) and* Uni 3 *(green). Core rebound is clearly seen in models one and two.*

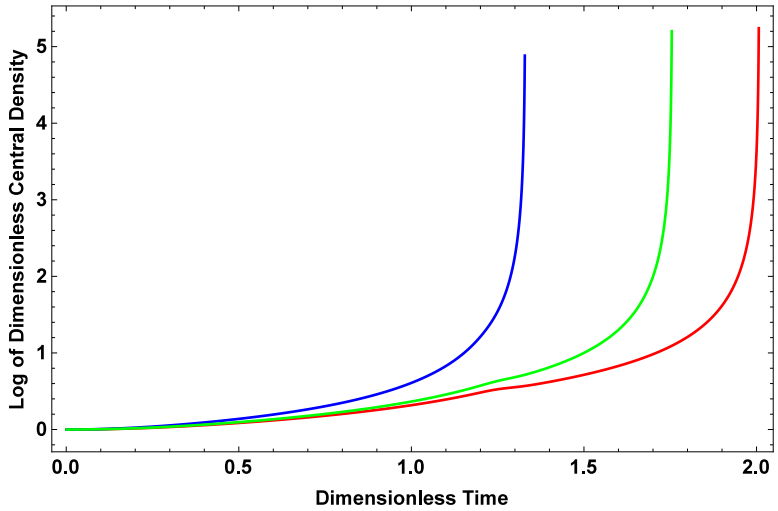


FIGURE 4.6: *The Figure illustrates the increase in central density for models* BE 1 *(red),* BE 2 *(blue) and* BE 3 *(green). No rebound is seen however the central accretion is temporarily decreased.*

Model	γ	m	k
Uni 1	0.66	0.022	13.2
Uni 2	0.42	0.029	16.4
Uni 3	0.11	0.10	32.2
BE 1	0.47	0.036	16.4
BE 2	0.51	0.063	14.2
BE 3	0.56	0.063	15.3

TABLE 4.2: *The Table shows the parameters that match the Bondi accretion solution to the numerical simulations performed using the TVD Runge-Kutta scheme.*

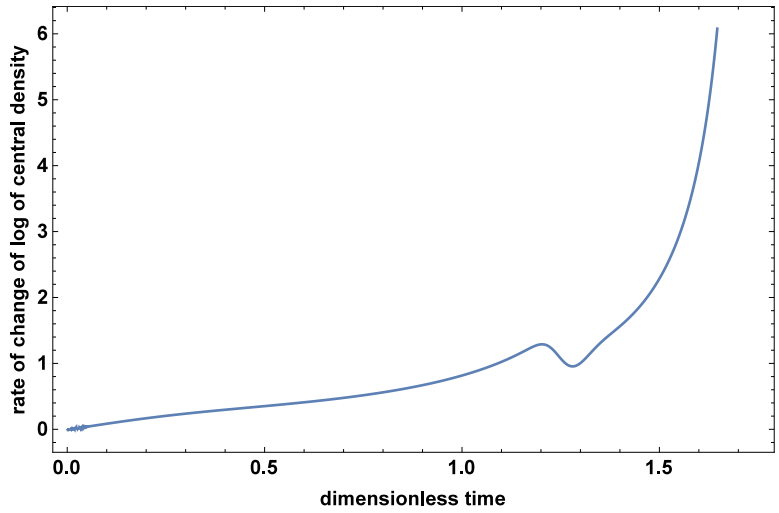


FIGURE 4.7: *The Figure illustrates the accretion rate at the centre for model* BE 1. *It is clear that the accretion rate is slowed down momentarily however gas continues to flow toward the centre.*

4.4 Concluding Remarks

In this Chapter we have used the TVD-MUSCL scheme with a Roe flux on a uniform grid to simulate the gravitational collapse of initially uniform clouds and perturbed Bonnor-Ebert spheres. We have found that core bounce will occur as long as the initial ratio of the free-fall to sound travel time satisfies the inequality

$$0.61 \lesssim \frac{t_{ff}}{t_s} \lesssim 0.75.$$

Collapse will occur without any bounce below 0.61 and the cloud will oscillate indefinitely if the ratio is larger than 0.75. We have shown that the core bounce mentioned by Hayashi and Nakano [1] is present in both the simulated models however it is significantly diminished in the case of the collapse of Bonnor-Ebert spheres. Using the analytical solutions for steady-state, Bondi accretion that we presented in the previous Chapter we have shown that effects of pressure are still important even as the collapsing cloud core becomes dense enough that radiative properties must be considered; Bondi accretion-type velocity and density profiles are more appropriate than free-fall ones. A caveat to this is the the velocity profiles derived from constant volume simulations will not match the Bondi accretion-type velocity profile since the velocity must vanish at the outer boundary.

In the next Chapter the problem of isothermal collapse is investigated with another scheme. The use of finite volumes is retained but the Marquina flux is used and the backward Euler time stepping is replaced with TVD Runge-Kutta time stepping.

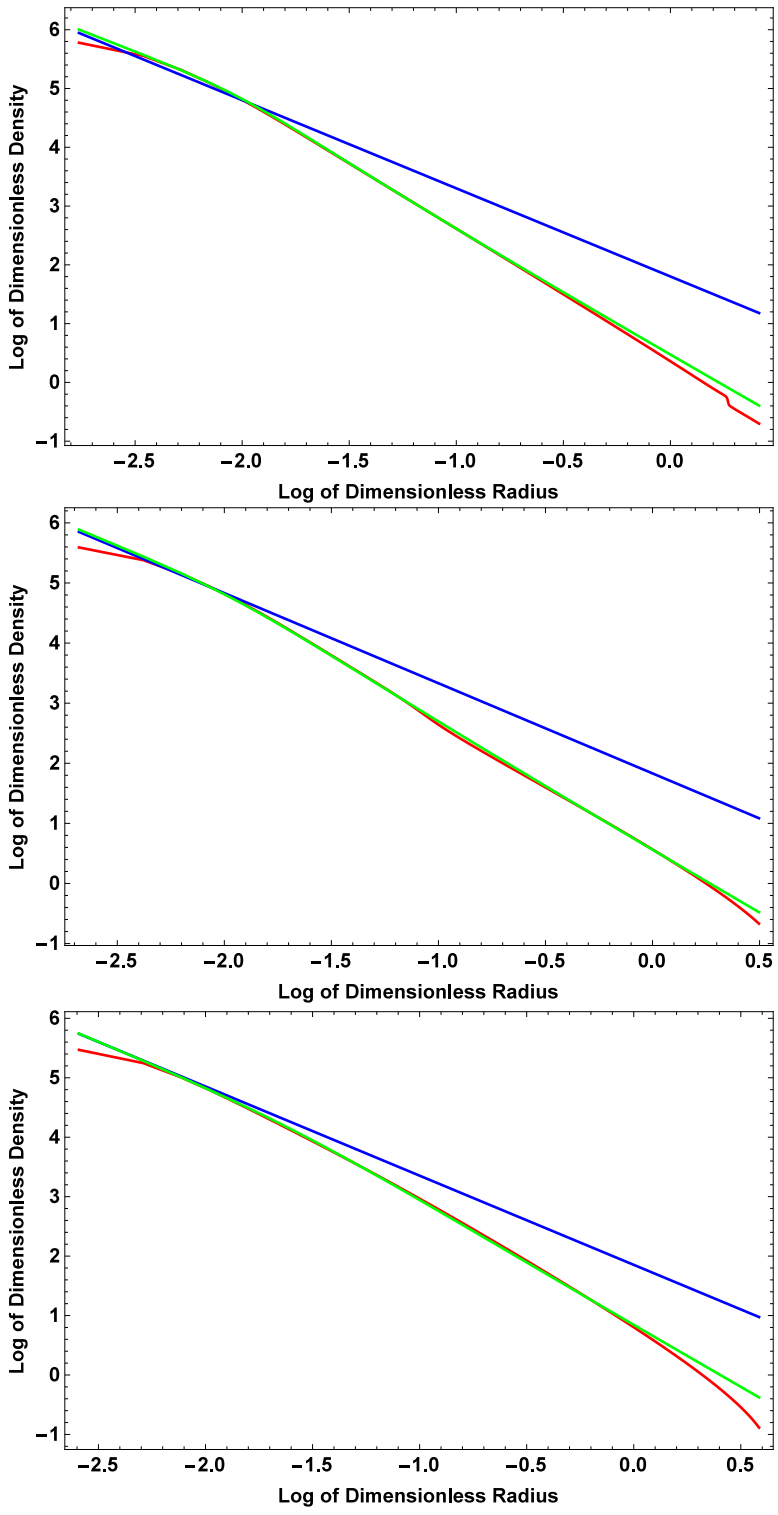


FIGURE 4.8: *The plots illustrate the density profiles of the initially uniform spheres for the last iteration together with the solution for steady-state accretion as well as the free-fall profile. The analytical solutions for steady-state accretion match closely with the numerical solution.*

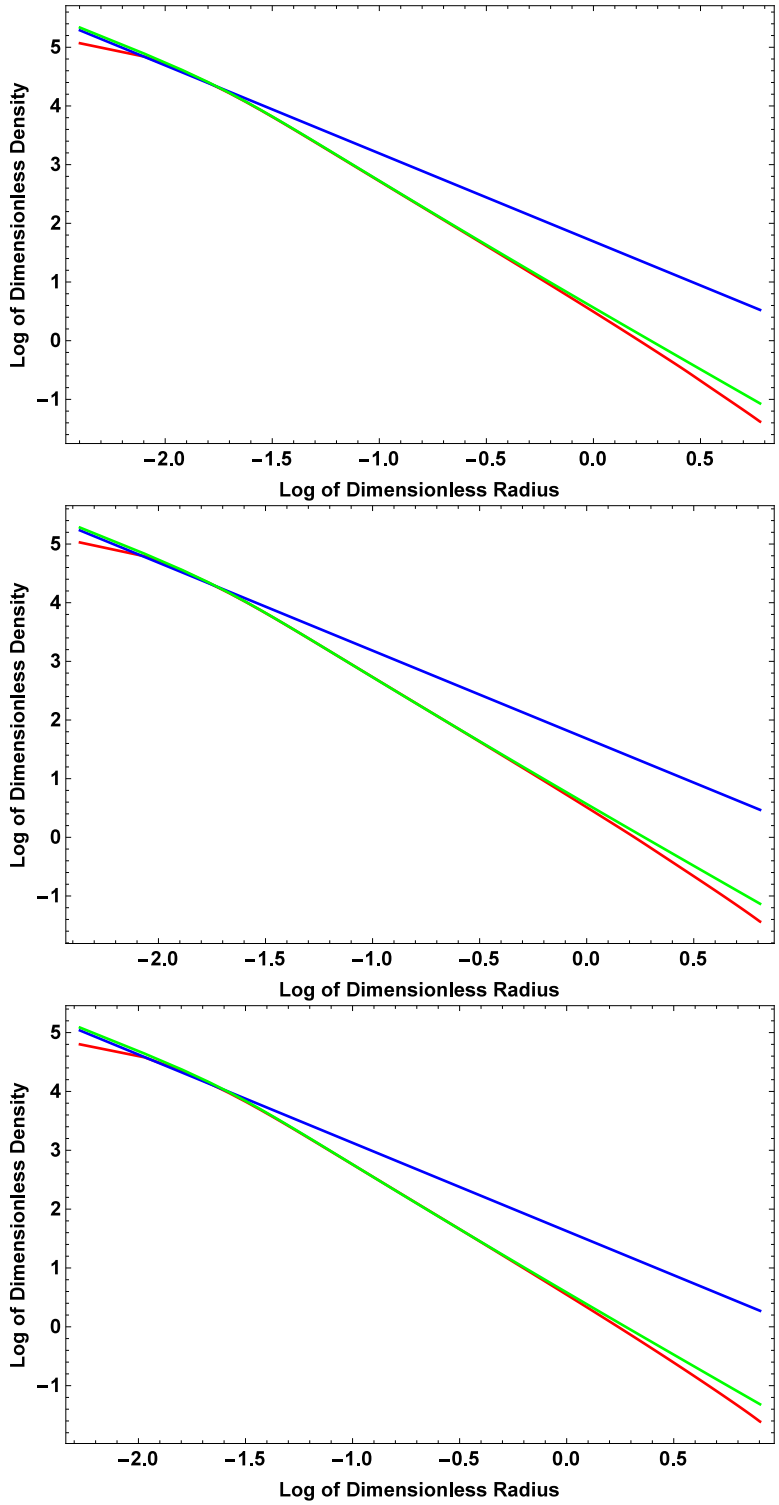


FIGURE 4.9: *The plots illustrate the density profiles of the perturbed Bonnor-Ebert spheres for the last iteration together with the solution for steady-state accretion as well as the free-fall profile. The analytical solutions for steady-state accretion match closely with the numerical solution.*

Chapter 5

Numerical Simulations of Isothermal Collapse: TVD Runge-Kutta Scheme

The six models introduced in the previous Chapter are simulated using the TVD Runge-Kutta time-stepping scheme with a Marquina flux. We have implemented a scheme that is second order accurate in space and first order in time in the previous chapter; the scheme implemented here is second order in space (in the smooth, continuous regions) but third-order in time. The simulations are performed for the sake of comparison with the simulations from the previous chapter. The results show very good agreement with the results of Chapter 4. This agreement is significant as it confirms the presence of the core bounce in both the initially uniform cloud and the Bonnor-Ebert sphere even though it is drastically reduced in the case of the Bonnor-Ebert sphere.

5.1 Introduction

The Euler time stepping used in the previous Chapter is easy to implement however it only offers first order temporal accuracy. If we consider the hydrodynamic equations in the weaker integral from, see equation (2.23) then the problem may be treated as a collection of first order coupled ordinary differential equations in time. Shu and Osher used this approach in their development of essentially non-oscillatory schemes (ENO schemes), [41]. Gottlieb and Shu extended this investigation [64] and found that the third order scheme was optimal.

While the Roe flux formula has proven to be extremely efficient for many problems in hydrodynamics it suffers from instability issues for other problems such as the shock reflection problem. Donat and Marquina proposed a hybrid between the Roe flux formula and the more diffusive local Lax-Friedrichs formula [65]. This approach has proven to be highly robust and has been used in situations where the circumstances of the flow are extreme. One example of this is the application of the scheme to problems in relativistic hydrodynamics [66, 67].

The Marquina flux is relevant to simulation of hydrodynamic collapse due to the core bounce that was observed previously. The same models are retained with only the numerics changing. In addition to the use of the Marquina flux formula and the third-order Runge-Kutta we have treated the gravitational source term in a separate time step that is encorporated into the Runge-Kutta time stepping.

5.2 Numerical Simulation

Before discussing the Marquina flux we highlight the main features of the local Lax-Friedrichs flux formula.

5.2.1 The Marqnuina Flux

Since the Roe scheme has been derived in the previous Section we will only discuss the local Lax-Friedrichs flux in the context of the Marquina flux. The LLF scheme for systems uses the largest characteristic speed to calculate the numerical flux:

$$\tilde{\mathbf{F}}^{LLF}_{i+1/2} = \frac{1}{2}\left[\mathbf{F}_i + \mathbf{F}_{i+1} - \left|A(\mathbf{Q}_i, \mathbf{Q}_{i+1})\right|\left(\mathbf{Q}_{i+1} - \mathbf{Q}_i\right)\right], \tag{5.1}$$

where

$$\left|A(\mathbf{Q}_i, \mathbf{Q}_{i+1})\right| = R^{-1}\left|\Lambda\right| R\Big|_{\mathbf{Q}:\max\{|\Lambda(\mathbf{Q}_i)|,|\Lambda(\mathbf{Q}_{i+1})|\}}.$$

From equation (5.1) and equation (4.10) from the previous Section the Marquina flux may be derived in component form with the following algorithm: define the two functions

$$\omega^{pl} = \mathbf{l}^p(\mathbf{Q}^l).\mathbf{Q}^l, \quad \phi^{pl} = \mathbf{l}^p(\mathbf{Q}^l).\mathbf{F}(\mathbf{Q}^l),$$

similarly

$$\omega^{pr} = \mathbf{l}^p(\mathbf{Q}^r).\mathbf{Q}^r, \quad \phi^{pr} = \mathbf{l}^p(\mathbf{Q}^r).\mathbf{F}(\mathbf{Q}^r).$$

The indices l and r indicate that respective quantities have been evaluated from the left and right states, $\mathbf{l}^p$ is the p^{th} left eigenvector of the Jacobian of $\mathbf{F}$, $\mathbf{Q}$ is the state vector and $\mathbf{F}$ is the flux function appearing in the fluid equations. Now, if the p^{th} eigenvalue, $\lambda^p(\mathbf{Q})$ does not change from one grid cell to the next then

$$\phi^{p+} = \phi^{pl} \quad \text{and} \quad \phi^{p-} = 0 \quad \text{if} \quad \lambda^p(\mathbf{Q}^l) > 0, \quad \text{else}$$

$$\phi^{p+} = 0 \quad \text{and} \quad \phi^{p-} = \phi^{pr} \quad \text{if} \quad \lambda^p(\mathbf{Q}^l) < 0.$$

If the eigenvalues change sign between neighbouring cells then with $\alpha^p = \max(\lambda^p(\mathbf{Q}^l), \lambda^p(\mathbf{Q}^r))$

$$\phi^{p+} = \phi^{pl} + 0.5\alpha^p\omega^{pl}, \quad \text{and} \quad \phi^{p-} = \phi^{pr} - 0.5\alpha^p\omega^{pr}.$$

From these quantities the Marquina flux may be found by computing

$$\mathbf{F}^{Marquina} = \sum_p \left(\phi^{p+}\mathbf{r}^p(\mathbf{Q}^l) + \phi^{p-}\mathbf{r}^p(\mathbf{Q}^r)\right).$$

The sum runs from one to the number of conservation laws.

Although a piecewise constant approximation is used in the simulations performed here the Marquina flux is easily adaptable to LPM and PPM (linear and parabolic piecewise methods).

5.2.2 Runge-Kutta Time-Stepping

Runge-Kutta time-stepping was introduced by Shu and Osher [41] when they first proposed essentially non-oscillatory (ENO) schemes and it has proven useful in achieving higher order temporal accuracy. Gottlieb and Shu [64] extended this work giving a detailed discussion of the TVD properties.

In order to implement the Runge-Kutta time-stepping method the Euler equations are integrated over the volume elements to obtain the method of lines form of the hyperbolic

conservation laws. This results in the following equation:

$$\frac{d\mathbf{Q}(t,r_i)}{dt}+\frac{r_{i+1/2}^2\mathbf{F}\left(\mathbf{Q}(t,r_{i+1/2})\right)-r_{i-1/2}^2\mathbf{F}\left(\mathbf{Q}(t,r_{i-1/2})\right)}{r_{i+1/2}^3-r_{i-1/2}^3}=\int_{\delta V_i}\mathbf{S}_g dV+\int_{\delta V_i}\mathbf{S}dV \quad (5.2)$$

Gottlieb and Shu [64] showed that a third order Runge-Kutta scheme with a CFL number of 3.2 resulted in a TVD scheme.

$$\begin{aligned}
\mathbf{Q}^{(1)} &= \mathbf{Q}^n-3\Delta t\left(\frac{r_{i+1/2}^2\tilde{\mathbf{F}}_{i+1/2}^n-r_{i-1/2}^2\tilde{\mathbf{F}}_{i-1/2}^n}{r_{i+1/2}^3-r_{i-1/2}^3}\right)\\
&+ 3\Delta t\mathbf{S}_g(\mathbf{Q}^n)\left(\frac{r_{i+1/2}^2-r_{i-1/2}^2}{r_{i+1/2}^3-r_{i-1/2}^3}\right)+\frac{3\Delta t\Delta r}{2}\frac{r_{i+1/2}^2\mathbf{S}(\mathbf{Q}_{i+1/2}^n)+r_{i-1/2}^2\mathbf{S}(\mathbf{Q}_{i-1/2}^n)}{r_{i+1/2}^3-r_{i-1/2}^3},\\
\mathbf{Q}^{(2)} &= \frac{3}{4}\mathbf{Q}^n+\frac{1}{4}\mathbf{Q}^{(1)}-\frac{3}{4}\Delta t\left(\frac{r_{i+1/2}^2\tilde{\mathbf{F}}_{i+1/2}^{(1)}-r_{i-1/2}^2\tilde{\mathbf{F}}_{i-1/2}^{(1)}}{r_{i+1/2}^3-r_{i-1/2}^3}\right)\\
&+ \frac{3}{4}\Delta t\mathbf{S}_g(\mathbf{Q}^{(1)})\left(\frac{r_{i+1/2}^2-r_{i-1/2}^2}{r_{i+1/2}^3-r_{i-1/2}^3}\right)+\frac{3\Delta t\Delta r}{8}\frac{r_{i+1/2}^2\mathbf{S}(\mathbf{Q}_{i+1/2}^n)+r_{i-1/2}^2\mathbf{S}(\mathbf{Q}_{i-1/2}^{(1)})}{r_{i+1/2}^3-r_{i-1/2}^3},\\
\mathbf{Q}^{n+1} &= \frac{1}{3}\mathbf{Q}^n+\frac{2}{3}\mathbf{Q}^{(2)}-2\Delta t\left(\frac{r_{i+1/2}^2\tilde{\mathbf{F}}_{i+1/2}^{(2)}-r_{i-1/2}^2\tilde{\mathbf{F}}_{i-1/2}^{(2)}}{r_{i+1/2}^3-r_{i-1/2}^3}\right)\\
&+ 2\Delta t\mathbf{S}_g(\mathbf{Q}^{(2)})\left(\frac{r_{i+1/2}^2-r_{i-1/2}^2}{r_{i+1/2}^3-r_{i-1/2}^3}\right)\frac{3\Delta t\Delta r}{8}\frac{r_{i+1/2}^2\mathbf{S}(\mathbf{Q}_{i+1/2}^n)+r_{i-1/2}^2\mathbf{S}(\mathbf{Q}_{i-1/2}^{(2)})}{r_{i+1/2}^3-r_{i-1/2}^3} \quad (5.3)
\end{aligned}$$

5.2.3 Non-uniform Grid Construction

In the simulations we have used a non-uniform grid which increases in resolution toward the centre. Such a non-uniform grid has been implemented by several authors, one example is the work by Foster and Chevalier [19]. Assume we want the thickness of the i^{th} cell to be larger than the $(i-1)^{th}$ cell by some fraction δ, then the thickness of the i^{th} cell will be given by

$$\Delta r_i=\Delta r_0(1+\delta)^{i-1}, \quad (5.4)$$

where Δr_0 is the thickness of the smallest cell – the radius of the central grid cell. Given that we want to have the outer boundary (not including the ghost cells) of the last cell coinciding with the radius of the cloud (we will call this R_c for now) we can find Δr_0 by solving the equation

$$\sum_{i=1}^{N}\Delta r_i=R_c, \quad (5.5)$$

where N is the number of grid cells. We find the following solution for equation (5.4)

$$\Delta r_i=\frac{R_c\delta}{(1+\delta)^N-1}(1+\delta)^{i-1}. \quad (5.6)$$

This can be shown to reduce to the constant $\frac{R_c}{N}$ as δ goes to zero. For the simulations performed in this Section we have chosen $N = 500$ and δ has been chosen so that the size of the central cell is the same as that of the previous Chapter. The result of this is that the simulations will terminate at roughly the same central density for both numerical methods since we have used the Truelove criterion [2] as a stopping condition.

5.2.4 Initializing Parameters for Numerical Simulations

Table 5.1 reiterates the parameters of each model.

Model	$R_{cloud}(10^{17}cm)$	$\rho_c(10^{-19}gcm^{-3})$	$\bar{\rho}(10^{-19}gcm^{-3})$	t_{ff}/t_s	$\rho_c/\bar{\rho}_m$
Uni 1	1.64	0.969	0.969	0.74	1
Uni 2	1.17	3.06	3.06	0.61	1
Uni 3	0.77	10.3	10.3	0.50	1
BE 1	1.59	5.89	1.17	0.72	5.02
BE 2	1.57	7.06	1.24	0.712	5.69
BE 3	1.52	11.52	1.35	0.701	8.51

TABLE 5.1: *In the above Table we provide initial data for the collapse of each presented model. The dimensional parameters are the clouds radius, the central density, and the mean density. The dimensionless quantities are the ratio of free-fall to sound travel time.*

5.3 Results and Discussion

Below, the results of the numerical simulations performed for the six cases under consideration are presented. Figures 5.1 and 5.2 show the density profile at various times, in units of free-fall time, for each model. While the bounce is a clear and distinct feature in the case of the uniform sphere, it appears only as a subtle decrease in central accretion in the case of the Bonnor-Ebert sphere. The core bounce does not result in an outward propagating pressure wave that develops into a shock. This is not unreasonable as the Bonnor-Ebert spheres increase in density toward the centre in such a way as to keep the cloud in hydrostatic equilibrium. As such the pressure gradient and gravitational force are similar in magnitude which is opposed to the situation in an initially uniform sphere. Table 5.2 below illustrates the parameter values that best match the Bondi accretion solutions found in Chapter 3 to the numerical simulations performed in this Chapter.

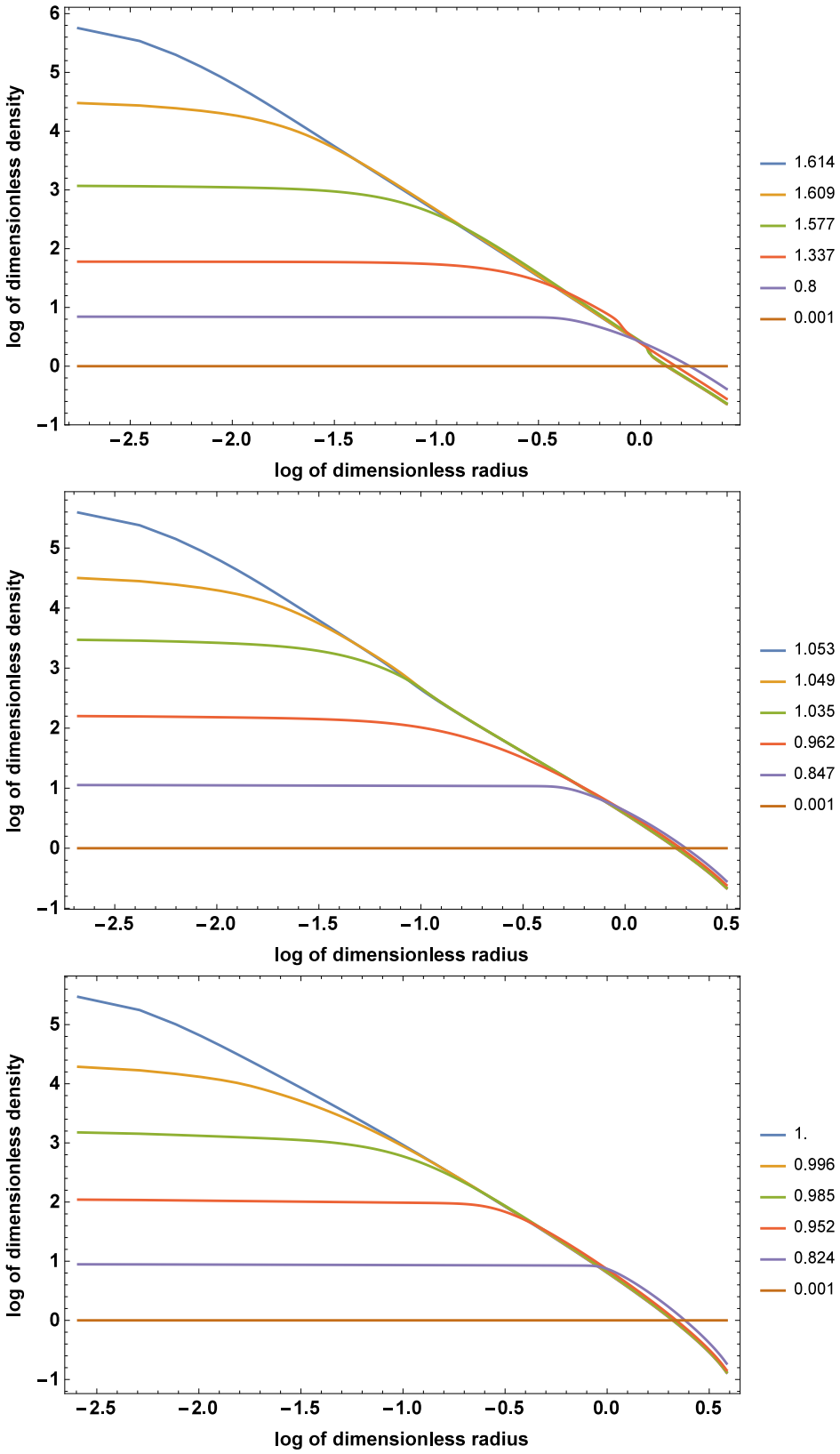


FIGURE 5.1: *The Figure shows plots of the density profile at various times (in units of t_{ff}), shown in the legend.*

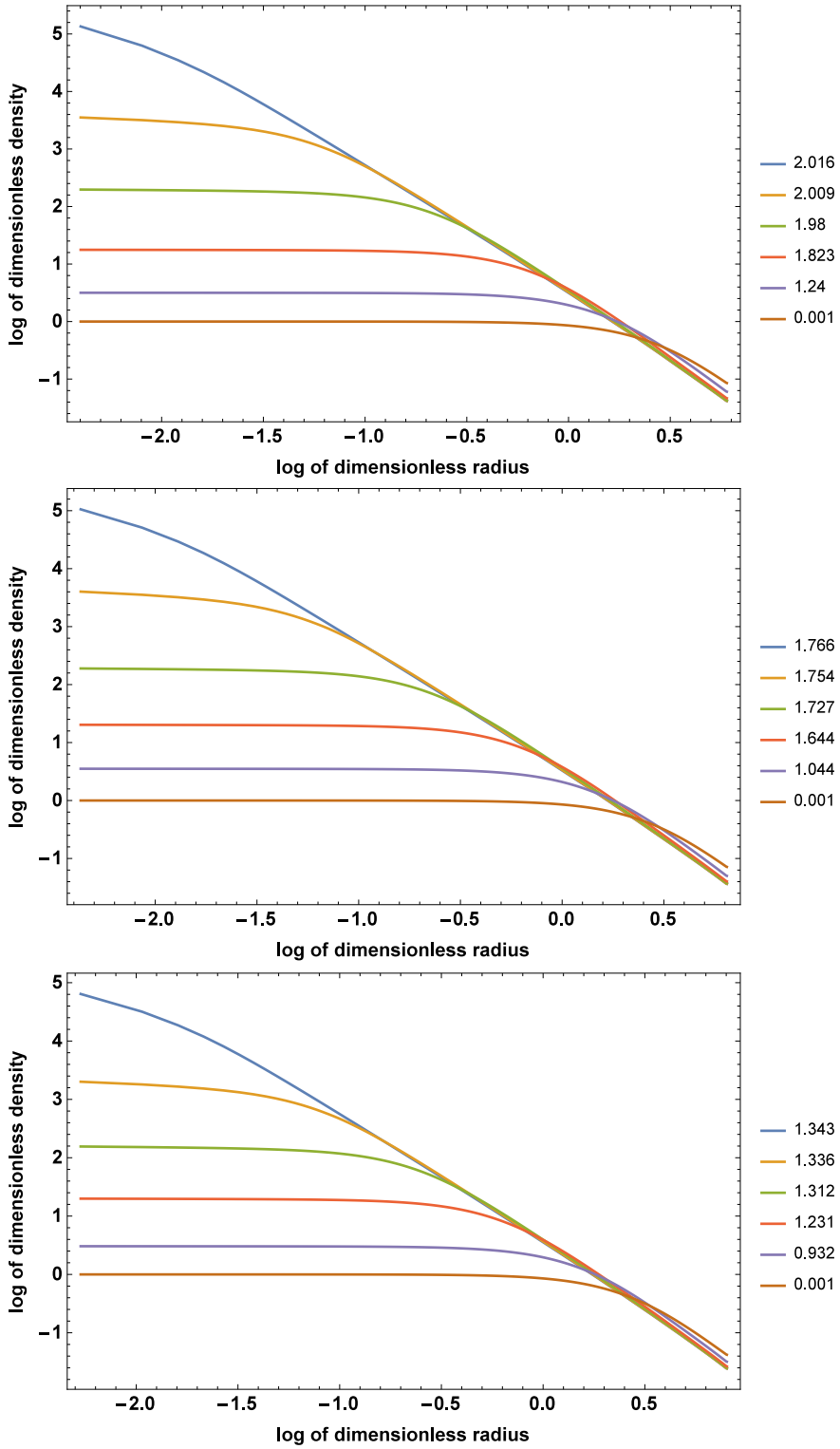


FIGURE 5.2: *The density profiles at various times for the three models with initially uniform density. All three clouds collapse in a similar fashion with subtle differences in the most dense cloud: collapse occurs in the central region slightly quicker while the rest of the cloud collapses and hence no core rebound is observed.*

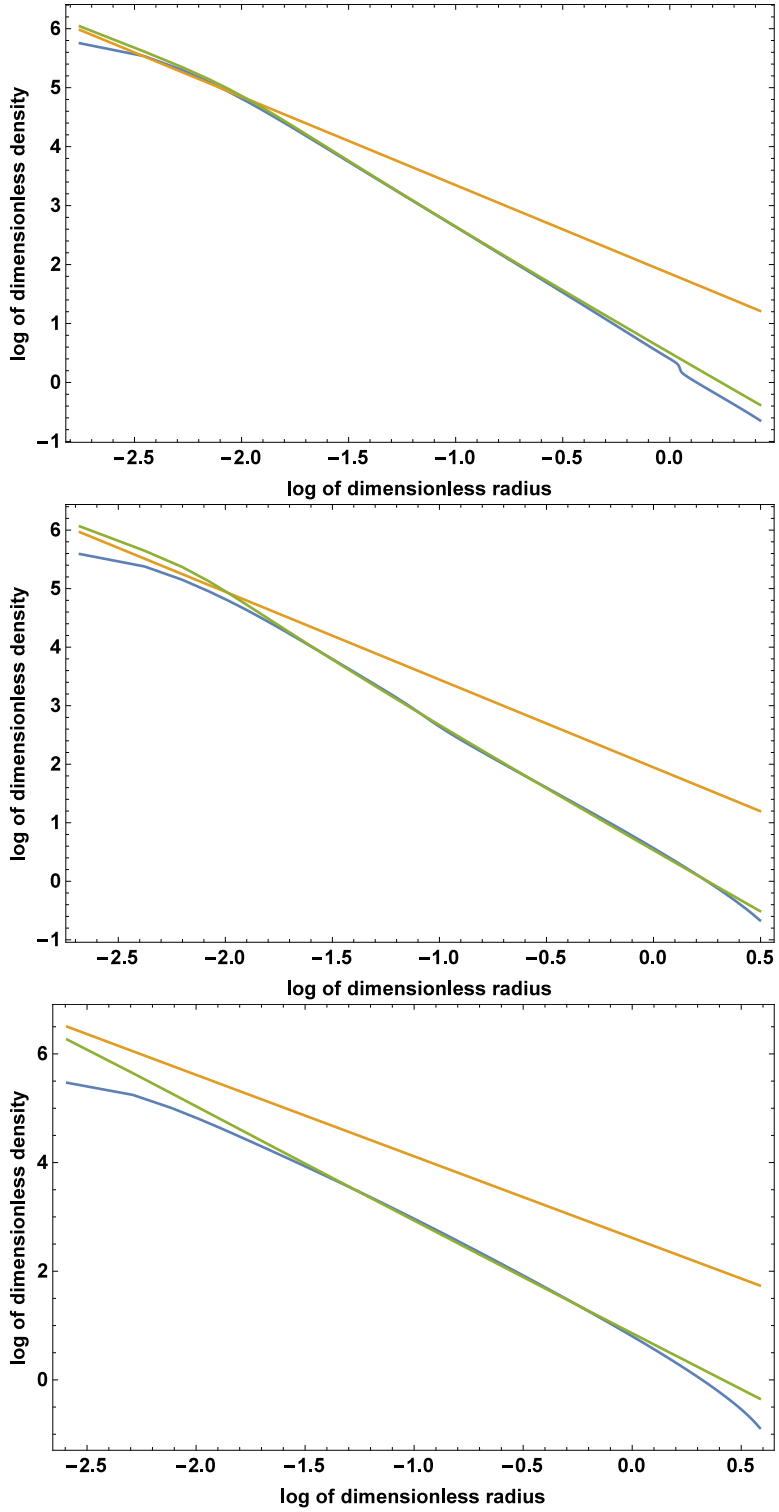


FIGURE 5.3: *The plots illustrate the density profiles for the last iteration together with the solution for steady-state accretion for the initially uniform clouds. The analytical solutions for steady-state accretion match closely with the numerical solution.*

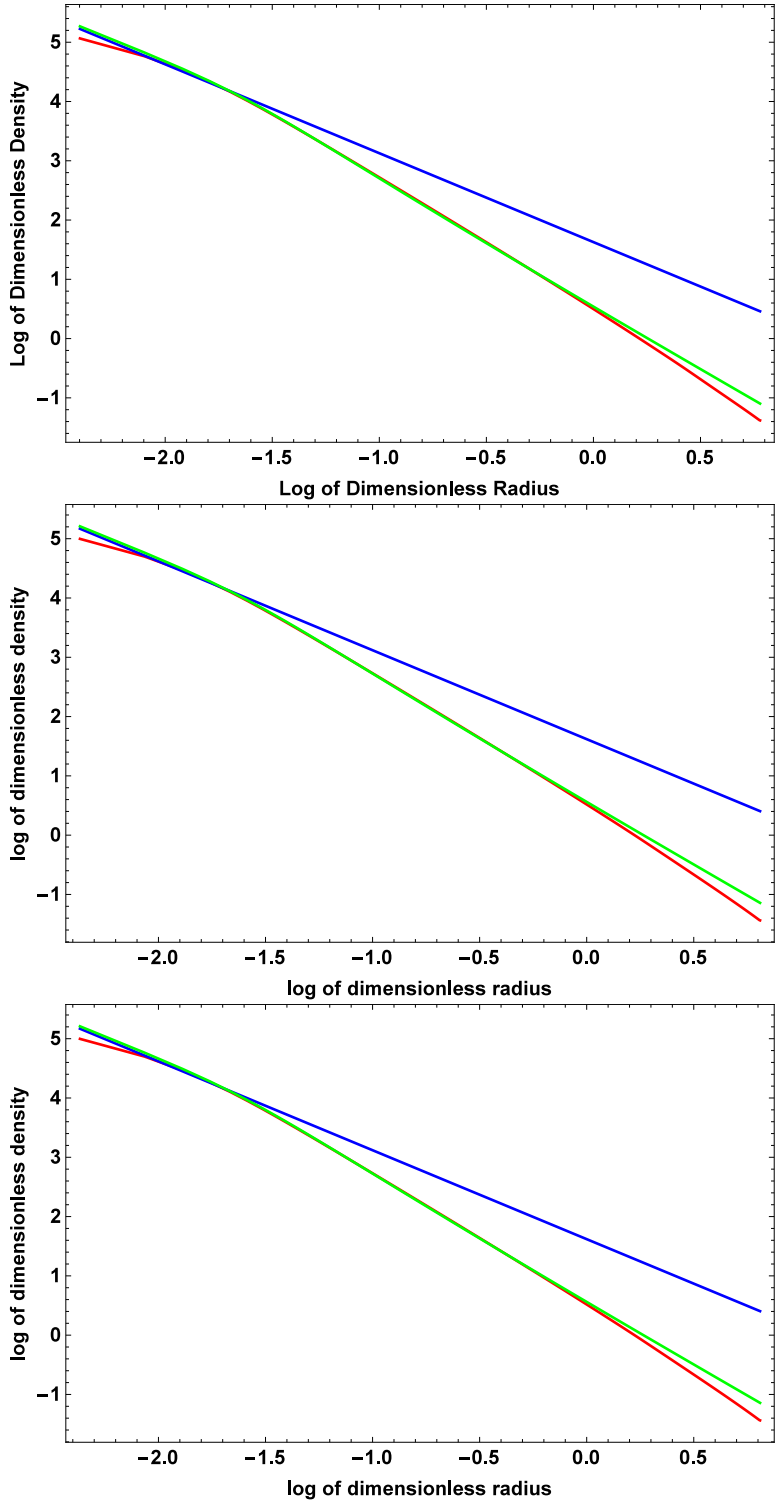


FIGURE 5.4: *The plots illustrate the density profiles for the last iteration together with the solution for steady-state accretion for the perturbed Bonnor-Ebert spheres. The analytical solutions for steady-state accretion match closely with the numerical solution.*

5.4 Concluding Remarks

In this Chapter we performed numerical simulations like that of the previous Chapter using the TVD Runge-Kutta scheme. We have used a non-uniform grid so as to decrease

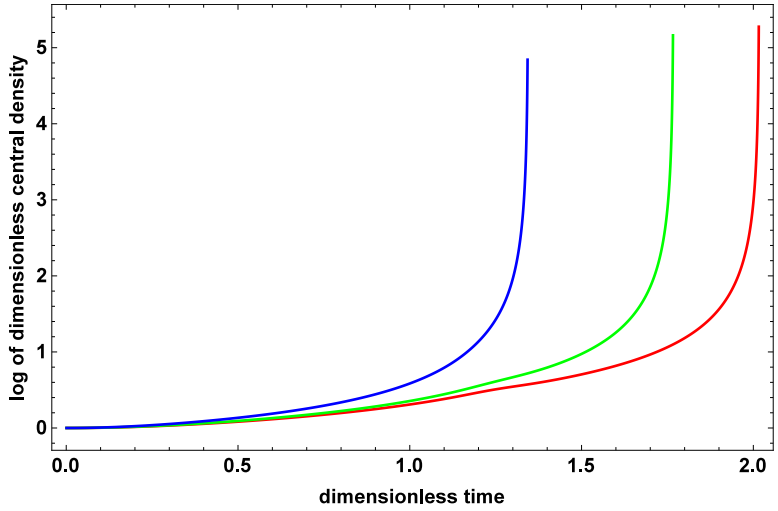


FIGURE 5.5: *The Figure illustrates the increase in central density for Bonnor-Ebert spheres with red, green, blue representing the order of increasing density. The core bounce is much less pronounced in the case of the Bonnor-Ebert spheres.*

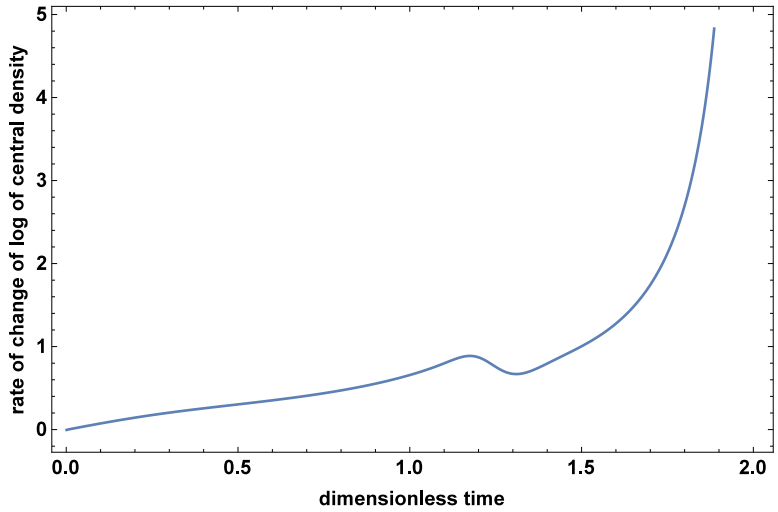


FIGURE 5.6: *The Figure illustrates the accretion rate at the centre for model* BE 1. *It is clear that the accretion rate is slowed down momentarily however gas continues to flow toward the centre.*

the number of grid cells but maintain the resolution of the central cell. The effect of this is that while time-stepping occurs in multiple steps the reduction in grid cells speeds up the numerical simulations. As a result the overall simulation takes roughly as long as that of a uniform grid. The simulations agree very well with those found in the previous Chapter which is significant because of the consequences regarding the physical interpretation of the solutions. The subtle differences in the solutions is due to the differences in the numerical methods. Table 5.2 shows the parameter values for the analytical solution of the density profiles. In the next Chapter we will discuss the convergence properties of the two numerical methods employed in this thesis.

Model	γ	m	k
Uni 1	0.675	0.021	13.2
Uni 2	0.45	0.027	16.4
Uni 3	0.10	0.11	32.2
BE 1	0.49	0.039	16.4
BE 2	0.04	0.061	14.2
BE 3	0.56	0.065	15.3

TABLE 5.2: *The Table shows the parameters that match the Bondi accretion solution to the numerical simulations performed using the TVD Runge-Kutta scheme.*

Chapter 6

Comparison of Numerical Schemes

Given the results found in Chapter 4 and Chapter 5 we consider the convergence properties of the two schemes with the aim of validating the results we have found. The convergence is investigated using two different approaches: the Lax-Wendroff theorem and a more computational technique in which we simulate the same model at different resolutions. We also investigate the existence of discontinuous solutions for steady-state accretion. This is relevant to our simulation since we have shown that when core bounce occurs it results in a outward propagating shock. For the sake of completeness the discontinuous solutions for accretion onto infinite cylinders and sheets are also discussed.

6.1 Introduction

In Chapter 3 we highlighted the importance of consistency, stability and convergence. In this chapter we will consider these features for the TVD-MUSCL scheme and the TVD-RK scheme. We have employed a Roe flux formula for the former scheme and a Maqruina flux for the latter. While the mentioned properties are well documented for the TVD-MUSCL scheme , the stability properties of Marquina flux presented [65] are directly inferred from those of the Roe and the local Lax-Fredrichs fluxes – the Marquina flux being a hybrid of the two. The equations modeled here are more complex than the sourceless hydrodynamic equations because of the presence of a source terms. One of the necessary conditions have already been met for both numerical methods, the CFL condition. Further principals of convergence have been considered here.

6.2 Analysis of the TVD-MUSCL Scheme

In this Section we will discuss the consistency, stability and convergence of the TVD-MUSCL scheme in the context of the numerical simulations performed here.

6.2.1 Consistency

In Chapter 4 we provided Roe's formula for the numerical flux

$$\tilde{\mathbf{F}}^{Roe}_{i+1/2}\left(\mathbf{Q}_i, \mathbf{Q}_{i+1}\right) = \frac{1}{2}\left[\mathbf{F}(\mathbf{Q}_i) + \mathbf{F}(\mathbf{Q}_{i+1}) - \left|A(\mathbf{Q}_{i+1/2})\right| \Delta\mathbf{Q}_{i+1/2}\right].$$

To check the consistency of the hyperbolic part we note that $\tilde{\mathbf{F}}\left(\mathbf{Q}, \mathbf{Q}\right) = \mathbf{F}(\mathbf{Q})$. To check the consistency of the rest of the numerical scheme we take a Taylor series expansion of the geometric and physical source terms which are provided by

$$\delta t \mathbf{S}_g \frac{\left(S_{i+1/2} - S_{i-1/2}\right)}{\delta V_i} \tag{6.1}$$

and

$$\frac{S_{i+1/2}\mathbf{S}_{i+1/2} + S_{i-1/2}\mathbf{S}_{i-1/2}}{2\delta V_i}, \tag{6.2}$$

respectively.

In the hydrodynamic equations the geometric source term is given by $\frac{2\rho c^2}{r}$ and it is approximated in the numerical method by equation (6.1). A Taylor series expansion of

this to second order provides the following

$$\rho(r_i,t)c^2\left(\frac{(r_i+\Delta r/2)^2-(r_i-\Delta r/2)^2}{(r_i+\Delta r/2)^3-(r_i-\Delta r/2)^3}\right)=\frac{2\rho(r_i,t)c^2}{r_i}-\frac{\Delta r^2\rho(r_i,t)c^2}{6r_i^3}+O(\Delta r^3). \quad (6.3)$$

Similarly, taking a Taylor series of the physical source term provides

$$\frac{3\left((r_i+\Delta r/2)^2S(r_i+\Delta r/2,t)+(r_i-\Delta r/2)^2S(r_i-\Delta r/2,t)\right)}{2\left((r_i+\Delta r/2)^3-(r_i-\Delta r/2)^3\right)} \quad (6.4)$$

$$=S(r_i,t)+\Delta r\frac{4S(r_i,t)+12rS_r(r_i,t)+3r^2S_{rr}(r_i,t)}{24r_i^2}. \quad (6.5)$$

Recall that in equation (6.5) the physical source term $S=-\rho\Phi_r$ where the subscripted r represents differentiation with respects to r. While the approximations are very good away from the centre of the cloud it should be noted that as $r\to dr$ the pressure is underestimated as $\frac{11\rho c^2}{6r}$ and the gravitational term is overestimated as $\frac{7\rho\Phi_r}{6}$ (plus some first and second order terms). This concern is eased by the fact that the gravitational force vanishes toward the centre of the cloud. Because of the piecewise linear approximation [43] of the grid cells as well as the numerical approximations used for the geometric and physical source terms we have second order spatial accuracy in smooth regions.

6.2.2 Stability

A detailed discussion of the stability properties of the TVD-MUSCL scheme can be found in [43].We will note however that the flux part of the numerical scheme is TVD thanks to the use of the van Albada limiter [63]. Additionally, the time step in the numerical scheme used here is chosen so that the CFL condition is met; thus we have implemented a scheme that is TVD and has met the necessary stability condition required.

6.2.3 Convergence

When discussing the convergence of hyperbolic problems the subtle point to note is that these equations do not converge to a particular solution after some given time. We can therefore only speak of the convergence of the numerical scheme to a particular solution after some time T has passed. Fortunately, due to the Lax-Wendroff theorem if we have a numerical scheme that is consistent as well as stable then that numerical scheme will converge to a weak solution [45]. We also test the convergence by showing that increasing the resolution of the grid between two simulations decreases the difference in the numerical solution generated by the scheme at the two different resolutions. In Figure 6.1 the plots in red, green and blue represent simulations run with increasing resolution (125,250 and 500 points respectively). The density at the cloud surface was

plot as a function of time for each resolution; the surface of the cloud was used as opposed to the centre because simulations run at different resolutions will terminate at different central densities due to the Truelove condition being used to stop the simulation. The difference between the blue and green plots is smaller than the difference between the green and red plot. This suggests that further increases in resolution will not change the density at the surface significantly; that is to say that the numerical scheme will converge to some solution. Thanks to the Lax-Wendroff theorem that solution will be a weak solution to the hydrodynamic equations.

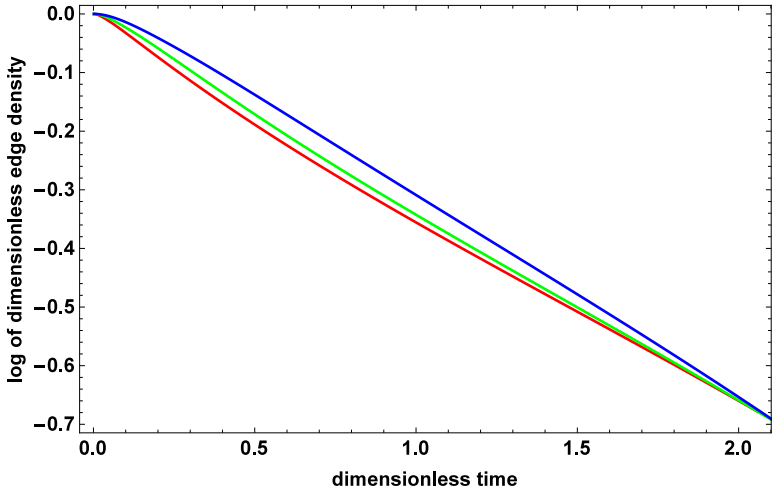


FIGURE 6.1: *The Figure illustrates the increase in central density for models one (red), two (blue) and three (green). Core rebound is clearly seen in models one and two.*

6.3 Analysis of TVD Runge-Kutta Scheme

In Chapter 5 we performed numerical simulations using the TVD Runge-Kutta scheme with a Marquina flux. Below we discuss the consistency, stability and convergence properties of the scheme. The stability properties of the third order Runge-Kutta scheme have been discussed in the work by Gottlieb [64] and will be commented on here. We then present the convergence features of the scheme by comparing simulations with increasing resolution.

6.3.1 Consistency

The consistency of the flux term is implicit in that $\tilde{\mathbf{F}}^{Maqruina}(\mathbf{Q},\mathbf{Q}) = \mathbf{F}(\mathbf{Q})$, where $\mathbf{F}$ is the flux in the exact equation. The consistency of the geometric and physical source terms remain unchanged and is identical to the results provided above.

6.3.2 Stability

Gottlieb and Shu [64] have shown that the third order Runge-Kutta time-stepping method is TVD when the CFL number is 0.32 and thus we are guaranteed TVD stability if we choose the time step such that $\Delta t \leq 0.32 \frac{\Delta r}{|\max(\lambda^i)|}$. As such stability is maintained without any restrictions on parameter choices.

6.3.3 Convergence

We have performed three numerical simulations of the collapse of a Bonner-Ebert sphere with $100, 200$ and 400 grid cells. Figure 6.2 shows the density at the surface of the collapsing cloud and the simulations are shown to converge as the grid resolution is increased.

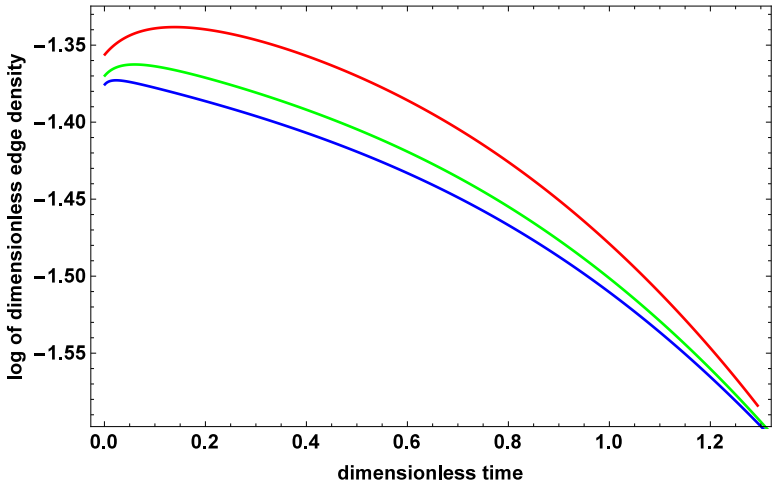


FIGURE 6.2: *The Figure illustrates the increase in central density for models one (red), two (blue) and three (green). Core rebound is clearly seen in models one and two.*

Lastly, we compare the solutions produced by each of the presented numerical methods. This has been performed by simulating the collapse of a uniform sphere. The results of this comparison are given in Figure 6.3 with the two plots seen to be in good agreement. The TVD Runge-Kutta scheme has a slightly higher central density due to the lower CFL number required for stability. We have shown the presence of the core bounce which leads to a discontinuity in the density and velocity profiles. Matching the numerical simulations to the analytical solutions found for steady-state accretion leads to the question of the existence of discontinuous solutions in terms of the analytical solutions presented in Chapter 3. We present the results of this investigation in the next Section.

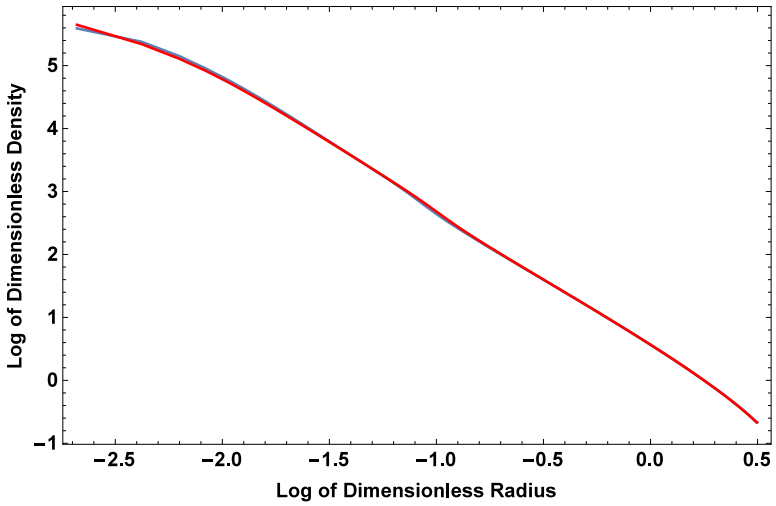


FIGURE 6.3: *The Figure illustrates the density profile at the last iteration for each numerical scheme presented in this thesis. The two methods are shown to be in very good agreement with each other despite the difference in their numerical structure. The TVD-MUSCL scheme appears in blue while the red plot corresponds to the TVD Runge-Kutta scheme.*

6.4 The Rankine-Hugoniot Conditions for Steady-State Accretion

In previous Chapters we have shown that the Bondi accretion solutions match reasonable with our numerical results and we have also shown that the core bounce results in a shock wave which propagates outward. This raises an important question: can the analytical solutions be connected by a discontinuity? The answer to this question is yes, however, the discontinuity must connect the two analytical solutions in a manner which is consistent with the Rankine-Hugoniot conditions. This is so that piecewise analytical solution is consistent with the integral form of the hydrodynamic equations.

It is clear from the analytical solutions that there are no continuous, transonic velocity profiles except in the spherical case (when $\gamma = 1$). In order to investigate the existence of discontinuous solutions the Rankine-Hugoniot conditions must be consulted. There are two jumps that are of interest: a transonic jump that would connect subsonic flow to supersonic flow – that is the solution moving from W_0 to W_{-1} or vice versa. The second type of jump would be restricted to the same flow type but with two different parameters. An example of this would be supersonic fluid colliding with slower, supersonic fluid.

6.4.1 Stationary Shocks

Since we are interested in relating the analytical solutions found for steady-state accretion we will focus our attention on stationary shock only.

First, consider the steady state continuity equation:

$$\frac{1}{\xi^n}\frac{d}{d\xi}\left(\xi^n \rho u\right) = 0, \tag{6.6}$$

and suppose that there is a discontinuity in the solution at ξ_s in the interval $\{\xi_1, \xi_2\}$. We know that the Rankine-Hugoniot condition for the density flux (in the case of stationary shocks) is given by

$$\rho u_1 = \rho u_2,$$

where ρu_1 and ρu_2 are the momentum densities on left and right hand sides of the discontinuity, that is

$$\lim_{\xi \to \xi_s^-} \rho u = \rho u_1, \quad \text{and} \quad \lim_{\xi \to \xi_s^+} \rho u = \rho u_2.$$

The Rankine-Hugonoit conditions are identically satisfied since the exact solution of equation (6.6) is given by $\rho u = \frac{k}{\xi^n}$ and therefore $\rho u_1 = \frac{k}{\xi_s} = \rho u_2$.

For the momentum flux the integral form of the momentum equation must be employed:

$$\begin{aligned}\int_{\xi_1}^{\xi_s}\left[\frac{1}{\xi^n}\frac{d}{d\xi}\left(\xi^n(\rho u^2 + \rho c^2)\right)\right]\xi^n d\xi \quad &+ \quad \int_{\xi_s}^{\xi_2}\left[\frac{1}{\xi^n}\frac{d}{d\xi}\left(\xi^n(\rho u^2 + \rho c^2)\right)\right]\xi^n d\xi \\ &= \int_{\xi_1}^{\xi_s}\frac{n\rho c^2}{\xi}\xi^n d\xi + \int_{\xi_s}^{\xi_2}\frac{n\rho c^2}{\xi}\xi^n d\xi \\ &- \int_{\xi_1}^{\xi_s}\rho\frac{d\Phi}{d\xi}\xi^n d\xi - \int_{\xi_s}^{\xi_2}\rho\frac{d\Phi}{d\xi}\xi^n d\xi.\end{aligned} \tag{6.7}$$

The above equation reduces to

$$\xi_2^n\left(\rho u_2^2 + \rho_2 c^2\right) - \xi_1^n\left(\rho u_1^2 + \rho_1 c^2\right) = \int_{\xi_1}^{\xi_2}\frac{n\rho c^2}{\xi}\xi^n d\xi - \int_{\xi_1}^{\xi_2}\rho\frac{d\Phi}{d\xi}\xi^n d\xi. \tag{6.8}$$

Now ξ_1 and ξ_2 tend to ξ_s from the left and right respectively and the right hand side of the integral vanishes since neither of the terms on the right hand side are singular. Using the solution for the continuity equation (and the limits mentioned above) the jump conditions may be rewritten as

$$\frac{k^2}{\rho_1 \xi_s^{2n}} + \rho_1 c^2 = \frac{k^2}{\rho_2 \xi_s^{2n}} + \rho_2 c^2. \tag{6.9}$$

Now, since a closed form solution for ρ is known it is possible to test this condition by checking if equation (6.9) is satisfied by the known density functions. Figures 6.4 to 6.7

show this for the three cases as well as the intersection of the two fluxes. In each case we have looked for the existence of discontinuous solutions resulting in transonic, subsonic and supersonic flow. Discontinuities consistent with the Rankine-Hugoniot conditions have been found for all but two cases: cylindrical subsonic flow when $\lambda < 1$ and planar transonic flow.

6.5 Discussion and Concluding Remarks

In this Chapter we have considered the convergence properties of the numerical schemes employed in this thesis. We have argued that they are convergent via the Lax-Wendroff theorem given that we have shown consistency and highlighted their stability features as discussed by their respective originators. We have also shown convergence of each solution independently by simulating the collapse of a single model at three different resolutions (100, 200 and 400 grid points). We have also shown convergence of the numerical schemes to the same solution graphically.

Lastly, we have shown that the core bounce can be represented by the connection of two analytical solutions via the Rankine -Hugoniot conditions. We have also shown that transonic solutions can exist in all cases when connected by a discontinuity. This was shown for one-dimensional flow only (spherical, cylindrical and planar).

In summary, the core bounce that has been observed in both cases should be regarded as a physical phenomenon whose observational effects have been mentioned by Hayashi [24]. More particularly, because of the difference in the appearance of the bounce in the two types of clouds it would be possible to infer the uniformity of Bok globules in the process of collapse. Clouds that are close to hydrostatic equilibrium are not prone to core bounce due to the increase in their internal pressure toward their centres. In the event of a discontinuity in the density, as a result of core bounce, it is still possible to match the analytical solutions of Bondi accretion by using the Rankine-Hugoniot conditions. This discontinuity would separate the cloud into three sections: the nascent core, a shell which feeds the core and a surrounding envelope. The exact nature of the shell requires further investigation since the gas contained in the shell may be ionized due to the shock wave which forms the outer boundary of the shell.

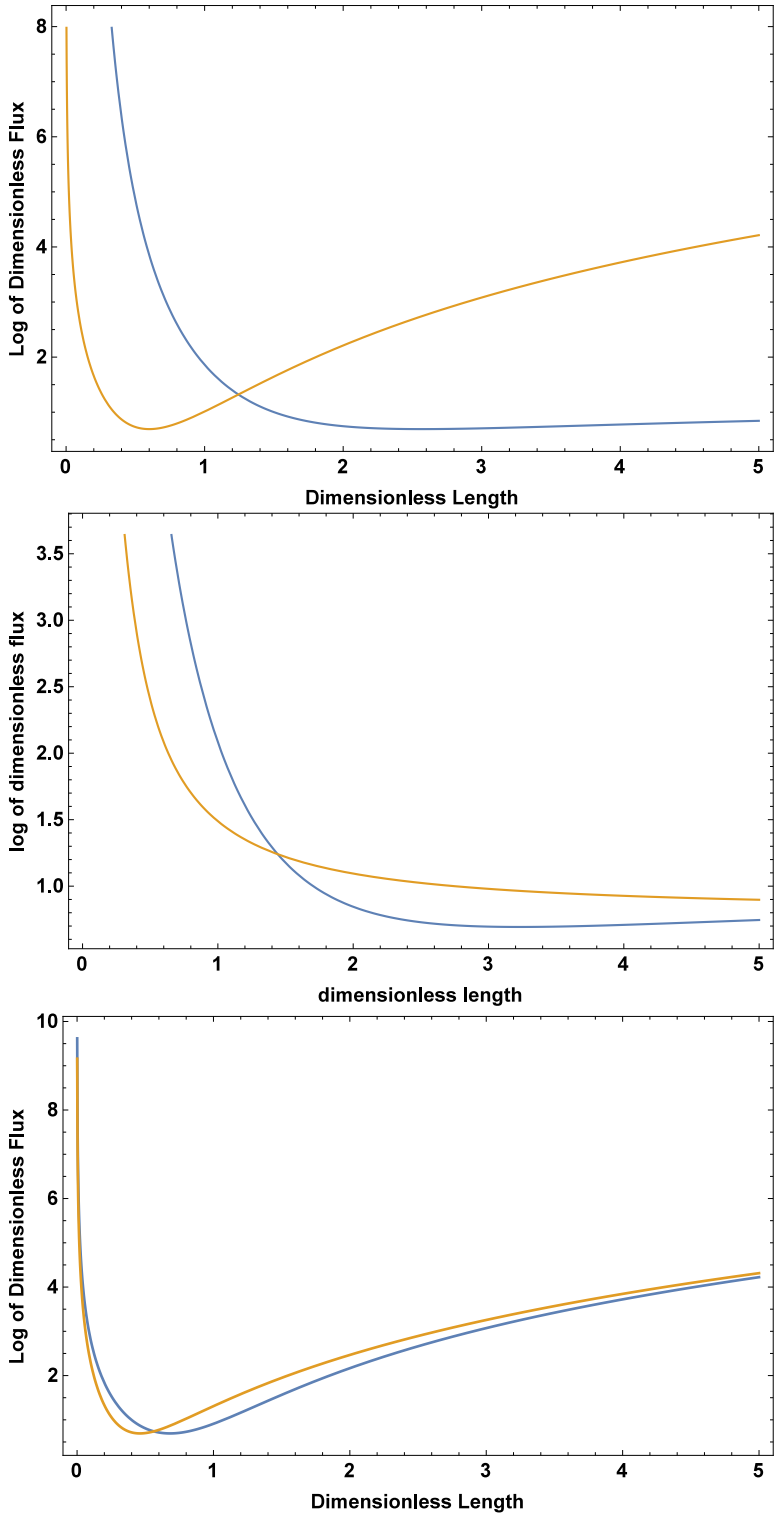


FIGURE 6.4: *The plots show the Rankine-Hugoniot conditions for transonic, subsonic and supersonic jumps for a spherical fragment.*

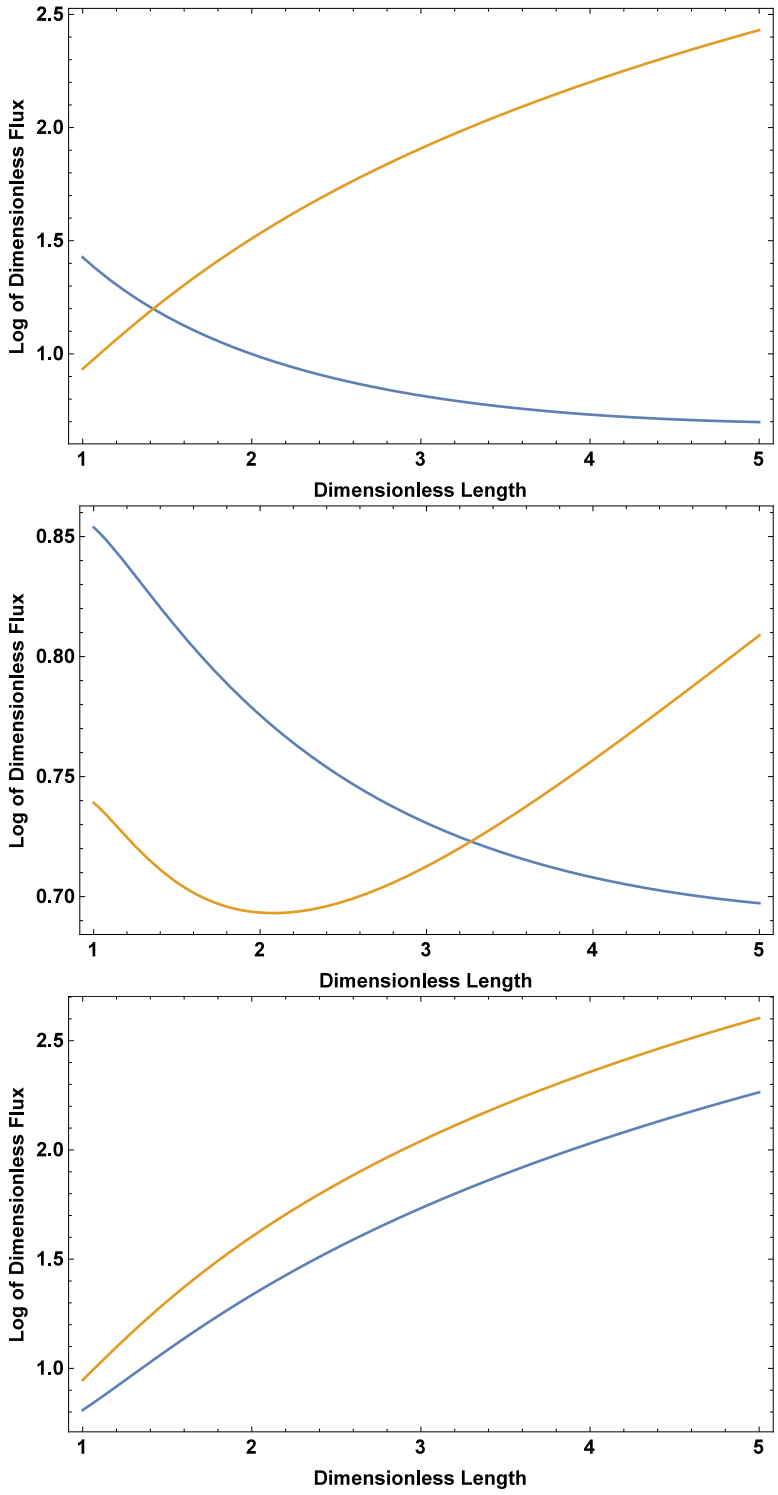


FIGURE 6.5: *The plots show the Rankine-Hugoniot conditions for transonic, subsonic and supersonic jumps for an infinite cylinder when* $\lambda < 1$*.Note that supersonic jumps are not possible as the two plots do not intersect meaning that the Rankine-Hugoniot conditions are not satisfied.*

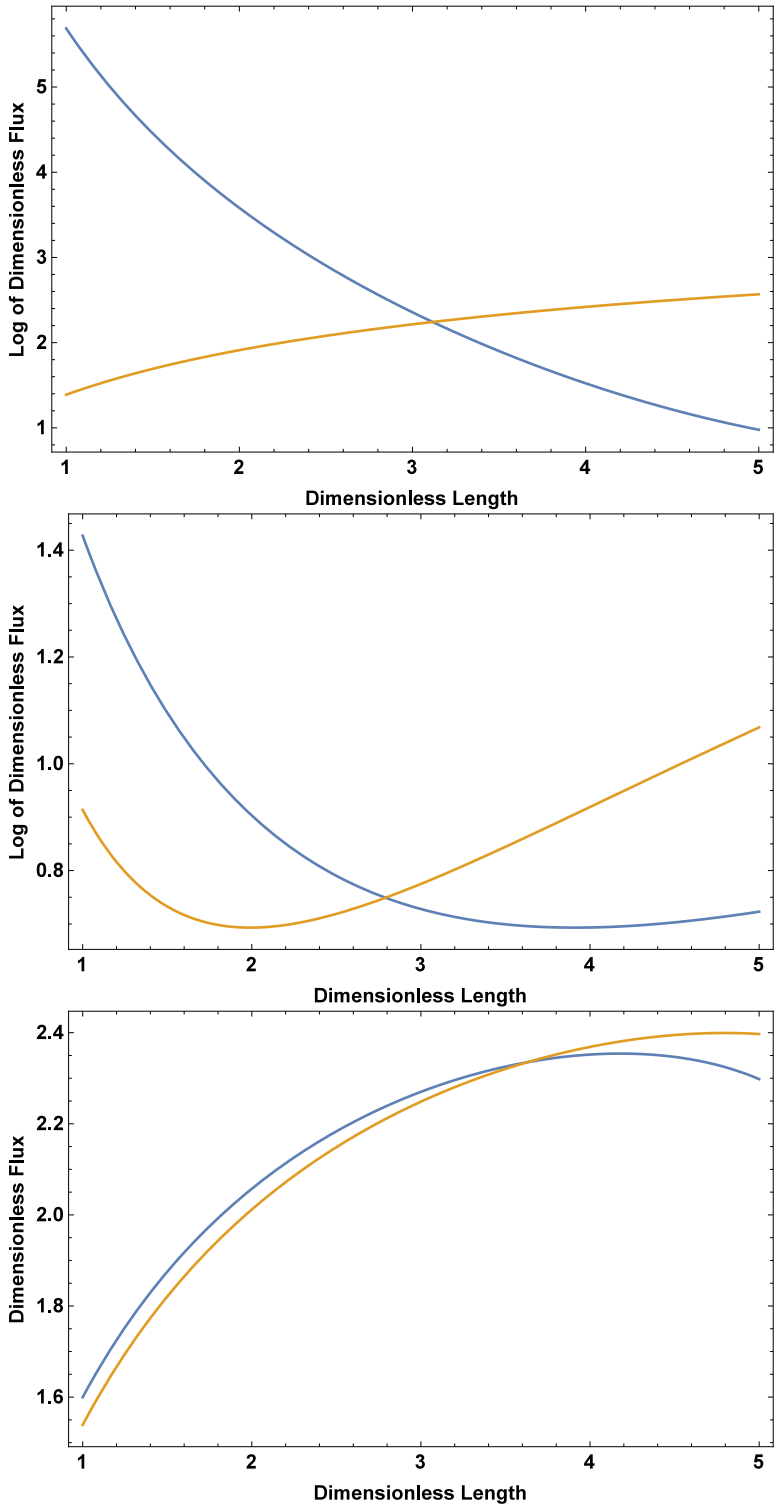


FIGURE 6.6: *The plots show the Rankine-Hugoniot conditions for transonic, subsonic and supersonic jumps for an infinite cylinder when* $\lambda > 1$.

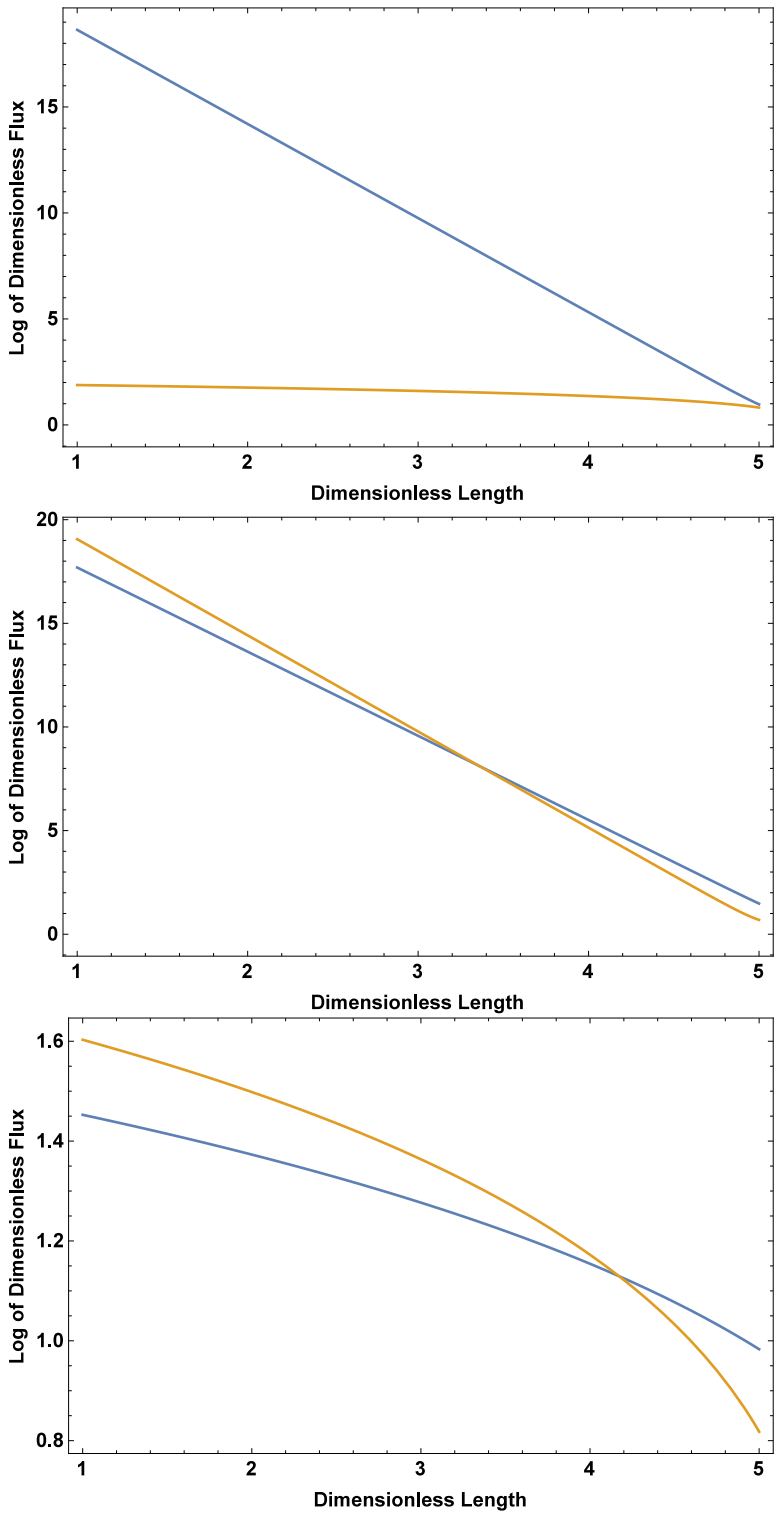


FIGURE 6.7: *The plots show the Rankine-Hugoniot conditions for transonic, subsonic and supersonic jumps from the top down. The condition for a transonic jump is not satisfied in the case of the infinite sheet as the two graphs intersect only at the maximum length x_m and both solutions are complex beyond that point.*

Chapter 7

Conclusion and Closing Statements

In this thesis numerical simulations of the spherically symmetric collapse of isothermal spheres have been performed with two questions in mind: is the bounce described by Hayashi and Nakano [1] observed in the numerical simulations (how it is related to the initial condition), and how similar are the density profiles of the collapsing spheres (in the late stages of the isothermal collapse) to the density profiles of a gas undergoing steady accretion onto a spherical protostellar core?

The importance of the bounce has been illustrated by Hayashi and Nakano [1] and it is that the resulting shock wave that propagates outward is capable of ionizing the hydrogen gas that it passes through. Through our one-dimensional simulations we have shown that the core bounce occurs when the initial ratio of free-fall to sound travel is between 0.61 and 0.75. Above this domain the cloud will not undergo collapse and below it the core bounce ceases to exist. The bounce in severely diminished in the collapse of the Bonnor-Ebert sphere; in fact the central density does not increase then decrease momentarily as it does in the initially uniform sphere. Instead, the accretion rate at the centre is reduced slightly.

To ensure validity of the results found in the simulations we employed two numerical methods: the TVD-MUSCL scheme of van Leer [43] and the TVD Runge-Kutta time stepping method due to Shu and Osher [41]. We have shown, through the Lax-Wendroff theorem as well as via simulations with increasing resolution, that both of the employed schemes converge. We can therefore say that the effect of core bounce observed in our numerical simulations are of physical relevance. To this end we can in future extend our investigation (through further numerical simulation) the ionizing ability of the outward propagating shock waves and the resulting effect on the collapse of the isothermal sphere.

We have also introduced novel, analytical solutions for steady-state accretion in one-dimensional flow – this has included planar, cylindrical and spherical accretion. The analytical solutions to the velocity profiles have been presented in terms of the primary and secondary branch cuts of the Lambert function and two parameters: m, the dimensionless mass and γ which is related to the bounds of the velocity. The analytical solution for the case of spherical accretion have been shown to replicate the solutions of Bondi [3] exactly, the adiabatic constant equal to one. The density profiles associated with the analytical solutions for spherical accretion have been compared to the density profiles found through our numerical simulation. While we have acknowledged the fact that the analytical solutions of steady accretion cannot be matched to the entire cloud (due to the boundary condition employed in the numerical simulation) we have shown that there is good agreement away from the centre (which should be interpreted as outside of the nascent core) and away from the surface of the cloud. This agreement has led us to using the exact solutions found for spherical, steady accretion to estimate physical properties of the forming protostellar core. Results from this experiment were found to be consistent with the literature, see [7]. In future work we will investigate isothermal collapse with different boundary conditions to explore the possibility of improving the agreement between the numerical and analytical solutions. The importance of the results presented in Chapter 3 is that isothermal collapse may be investigated using steady accretion as an initial condition, particularly in the case of supersonic converging flows.

Bibliography

[1] C. Hayashi and T. Nakano. Thermal and dynamical properties of a protostar and its contraction to the stage of quasi-static equilibrium. *Progress of Theoretical Physics*, 34:754–775, 1965.

[2] J. K. Truelove, R. I. Klein, C. F. McKee, J. H. Holliman II, L. H. Howell, and J. A. Greenough. The jeans condition: a new constraint on spatial resolution in simulations of isothermal self-gravitational hydrodynamics. *The Astrophysical Journal Letters*, 489:L179–L183, 1997.

[3] H. J. Bondi. On spherically symmetrical accretion. *Monthly Notices of the Royal Astronomical Society*, 112:195–204, 1952.

[4] Orion molecular cloud. URL http://apod.nasa.gov/apod/ap101023.html.

[5] Bok globules. URL http://www.wolaver.org/space/globules.htm.

[6] R. B. Larson. Numerical calculations of the dynamics of collapsing proto-star. *Monthly Notices of the Royal Astronomical Society*, 145:271–295, 1969.

[7] S. W. Stahler and F. Palla. *The formation of stars*. John Wiley & Sons, 2008.

[8] P. Bodenheimer. *Principles of star formation*. Springer Science & Business Media, 2011.

[9] R. B. Larson. The collapse of a rotating cloud. *Monthly Notices of the Royal Astronomical Society*, 156:437–458, 1972.

[10] D. C. Black and P. Bodenheimer. Evolution of rotating interstellar clouds. i-numerical techniques. *The Astrophysical Journal*, 199:619–632, 1975.

[11] A. P. Boss. Protostellar formation in rotating interstellar clouds. ii-axially symmetric collapse. *The Astrophysical Journal*, 237:563–573, 1980.

[12] M. L. Norman, J. R. Wilson, and R. T. Barton. A new calculation on rotating protostar collapse. *The Astrophysical Journal*, 239:968–981, 1980.

[13] J. M. Stone and M. L. Norman. Zeus-2d: A radiation magnetohydrodynamics code for astrophysical flows in two space dimensions. i-the hydrodynamic algorithms and tests. *The Astrophysical Journal Supplement Series*, 80:753–790, 1992.

[14] J. M. Stone, T. A. Gardiner, P. Teuben, J. F. Hawley, and J. B. Simon. Athena: a new code for astrophysical mhd. *The Astrophysical Journal Supplement Series*, 178:137–177, 2008.

[15] J. H. Jeans. The stability of a spherical nebula. *Philosophical Transactions of the Royal Society of London. Series A, Containing Papers of a Mathematical or Physical Character*, pages 1–53, 1902.

[16] W. B. Bonnar. Boyle's law and gravitational instability. *Monthly Notices of the Royal Astronomical Society*, 116:351–359, 1956.

[17] R. Ebert. Über die verdichtung von h i-gebieten. mit 5 textabbildungen. *Zeitschrift fur Astrophysik*, 37:217–232, 1955.

[18] M. V. Penston. Dynamics of self-gravitating gaseous spheres-ii. collapses of gas spheres with cooling and the behaviour of polytropic gas spheres. *Monthly Notices of the Royal Astronomical Society*, 145:457–485, 1969.

[19] P. N. Foster and R. A. Chevalier. Gravitational collapse of an isothermal sphere. *The Astrophysical Journal*, 416:303–311, 1993.

[20] S. Ogino, K. Tomisaka, and F. Nakamura. Gravitational collapse of spherical interstellar clouds. *Publications of the Astronomical Society of Japan*, 51:637–651, 1999.

[21] F. H. Shu. Self-similar collapse of isothermal spheres and star formation. *The Astrophysical Journal*, 214:488–497, 1977.

[22] C. Hunter. On similarity solutions for the condensation of isothermal spherical gas clouds. *Monthly Notices of the Royal Astronomical Society*, 223:391–398, 1986.

[23] P. Bodenheimer and A. Sweigart. Dynamic collapse of the isothermal sphere. *The Astrophysical Journal*, 152:515–522, 1968.

[24] C. Hayashi. Evolution of protostars. *Annual Review of Astronomy and Astrophysics*, 4:171, 1966.

[25] A. P. Boss and J. G. Haber. Axisymmetric collapse of rotating, isothermal clouds. *The Astrophysical Journal*, 255:240–244, 1982.

[26] A. Whitworth and D. Summers. Self-similar condensation of spherically symmetric self-gravitating isothermal gas clouds. *Monthly Notices of the Royal Astronomical Society*, 214:1–25, 1985.

[27] Y. Lou and Y. Shen. Envelope expansion with core collapse—i. spherical isothermal similarity solutions. *Monthly Notices of the Royal Astronomical Society*, 348:717–734, 2004.

[28] F. Bian and Y. Lou. Spherical isothermal self-similar shock flows. *Monthly Notices of the Royal Astronomical Society*, 363:1315–1328, 2005.

[29] J. C. Tsai and J. L. Hsu. Protostellar collapse with a shock. *The Astrophysical Journal*, 448:774–787, 1995.

[30] F. H. Shu, S. Lizano, D. Galli, J. Cantó, and G. Laughlin. Self-similar champagne flows in h ii regions. *The Astrophysical Journal*, 580:969–998, 2002.

[31] A. P. Whitworth, A. S. Bhattal, N. Francis, and S. J. Watkins. Star formation and the singular isothermal sphere. *Monthly Notices of the Royal Astronomical Society*, 283:1061–1070, 1996.

[32] Y. Aikawa, E. Herbst, H. Roberts, and P. Caselli. Molecular evolution in collapsing prestellar cores. iii. contraction of a bonnor-ebert sphere. *The Astrophysical Journal*, 620:330–346, 2005.

[33] A. P. Boss. Protostellar formation in rotating interstellar clouds. i-numerical methods and tests. *The Astrophysical Journal*, 236:619–627, 1980.

[34] A. P. Boss. Protostellar formation in rotating interstellar clouds. iii-nonaxisymmetric collapse. *The Astrophysical Journal*, 237:866–876, 1980.

[35] A. Burkert and P. Bodenheimer. Multiple fragmentation in collapsing protostars. *Monthly Notices of the Royal Astronomical Society*, 264:798–806, 1993.

[36] P. Cassen and D. Pettibone. Steady accretion of a rotating fluid. *The Astrophysical Journal*, 208:500–511, 1976.

[37] P. Bodenheimer, G. P. Laughlin, M. Rozyczka, T. Plewa, and H. W. Yorke. *Numerical Methods in Astrophysics: An Introduction.* Taylor & Francis, 2006.

[38] R. A. Gentry, R. E. Martin, and B. J. Daly. An eulerian differencing method for unsteady compressible flow problems. *Journal of Computational Physics*, 1:87–118, 1966.

[39] P. Colella and P. R. Woodward. The piecewise parabolic method (ppm) for gas-dynamical simulations. *Journal of computational physics*, 54:174–201, 1984.

[40] M. Rozyczka, W. M. Tscharnuter, K. H. Winkler, and H. W. Yorke. Fragmentation of interstellar clouds-three-dimensional hydrodynamical calculations. *Astronomy and Astrophysics*, 83:118–128, 1980.

[41] C. Shu and S. Osher. Efficient implementation of essentially non-oscillatory shock-capturing schemes. *Journal of Computational Physics*, 77:439–471, 1988.

[42] S. K. Godunov. A difference method for numerical calculation of discontinuous solutions of the equations of hydrodynamics. *Matematicheskii Sbornik*, 89:271–306, 1959.

[43] B. van Leer. Towards the ultimate conservative difference scheme. v. a second-order sequel to godunov's method. *Journal of computational Physics*, 32:101–136, 1979.

[44] A. Marquina. Local piecewise hyperbolic reconstruction of numerical fluxes for nonlinear scalar conservation laws. *SIAM Journal on Scientific Computing*, 15: 892–915, 1994.

[45] R. J. LeVeque. *Finite volume methods for hyperbolic problems*, volume 31. Cambridge university press, 2002.

[46] R. Courant, K. Friedrichs, and H. Lewy. On the partial difference equations of mathematical physics. *IBM journal of Research and Development*, 11:215–234, 1967.

[47] A. P. Boss and D. C. Black. Collapse of accreting, rotating, isothermal, interstellar clouds. *The Astrophysical Journal*, 258:270–279, 1982.

[48] P. Bodenheimer. The evolution of protostars of 1 and 12 solar masses. *The Astrophysical Journal*, 153:483–494, 1968.

[49] H. Gong and E. C. Ostriker. Protostar formation in supersonic flows: growth and collapse of spherical cores. *The Astrophysical Journal*, 699:230–244, 2009.

[50] M. L. Norman and J. R. Wilson. The fragmentation of isothermal rings and star formation. *The Astrophysical Journal*, 224:497–511, 1978.

[51] J. Jeans. The physics of the universe. *Nature*, 122:689–700, 1928.

[52] P. Bastien. Gravitational collapse and fragmentation of isothermal, non-rotating, cylindrical clouds. *Astronomy and Astrophysics*, 119:109–116, 1983.

[53] S. M. Miyama, S. Narita, and C. Hayashi. Fragmentation of isothermal sheet-like clouds. i solutions of linear and second-order perturbation equations. *Progress of theoretical physics*, 78:1051–1064, 1987.

[54] S. Narita, C. Hayashi, and S. M. Miyama. Characteristics of collapse of rotating isothermal clouds. *Progress of theoretical physics*, 72:1118–1136, 1984.

[55] L. Spitzer Jr. The dynamics of the interstellar medium. iii. galactic distribution. *The Astrophysical Journal*, 95:329, 1942.

[56] J. Ostriker. The equilibrium of polytropic and isothermal cylinders. *The Astrophysical Journal*, 140:1056, 1964.

[57] S. M. Miyama, S. Narita, and C. Hayashi. Fragmentation of isothermal sheet-like clouds. ii—full nonlinear numerical simulations—. *Progress of theoretical physics*, 78:1273–1287, 1987.

[58] S. Chandrasekhar. *An introduction to the study of stellar structure*, volume 2. Courier Corporation, 1957.

[59] Fabian Heitsch. Gravitational infall onto molecular filaments. *The Astrophysical Journal*, 769:129, 2013.

[60] M. V. Penston. Dynamics of self-gravitating gaseous spheres-iii. analytical results in the free-fall of isothermal cases. *Monthly Notices of the Royal Astronomical Society*, 144:425–448, 1969.

[61] C. Hunter. The collapse of unstable isothermal spheres. *The Astrophysical Journal*, 218:834–845, 1977.

[62] P. L. Roe. Approximate riemann solvers, parameter vectors, and difference schemes. *Journal of computational physics*, 43:357–372, 1981.

[63] G. D. van Albada, B. van Leer, and W. W. Roberts Jr. A comparative study of computational methods in cosmic gas dynamics. *Astronomy and Astrophysics*, 108: 76–84, 1982.

[64] S. Gottlieb and C. Shu. Total variation diminishing runge-kutta schemes. *Mathematics of computation of the American Mathematical Society*, 67:73–85, 1998.

[65] R. Donat and A. Marquina. Capturing shock reflections: an improved flux formula. *Journal of Computational Physics*, 125:42–58, 1996.

[66] R. Donat, J. A. Font, J. M. Ibánez, and A. Marquina. A flux-split algorithm applied to relativistic flows. *Journal of Computational Physics*, 146:58–81, 1998.

[67] J. M. Martí, E. Müller, J. A. Font, J. M. Ibáñez, and A. Marquina. Morphology and dynamics of relativistic jets. *The Astrophysical Journal*, 479:151–163, 1997.